

**RIVERBED MORPHOLOGY, HYDRODYNAMICS
AND HYPORHEIC EXCHANGE PROCESSES**

by
Anzy Lee

A Dissertation

Submitted to the Faculty of Purdue University

In Partial Fulfillment of the Requirements for the degree of

Doctor of Philosophy



Lyles School of Civil Engineering

West Lafayette, Indiana

May 2020

THE PURDUE UNIVERSITY GRADUATE SCHOOL
STATEMENT OF COMMITTEE APPROVAL

Dr. Antoine F. Aubeneau, Chair

Lyles School of Civil Engineering

Dr. Meinhard B. Cardenas

Department of Geological Sciences, The University of Texas at Austin

Dr. John H. Cushman

Department of Earth, Atmospheric, and Planetary Sciences

Dr. Cary D. Troy

Lyles School of Civil Engineering

Approved by:

Dr. Dulcy M. Abraham

Dedicated to my husband, Sehyun

ACKNOWLEDGMENTS

Thanks to my advisor, Prof. Antoine Aubeneau, for his guidance and support over the course of my research. I acknowledge Purdue Research Foundation for financial support for this study.

Thanks to Prof. Bayani Cardenas and Prof. Xiaofeng Liu for accommodating me as a visiting student and helping me with developing research ideas and numerical models. Thanks to Prof. John Cushman and Prof. Cary Troy for giving me constructive feedbacks and suggestions on my research and serving on my examination committee.

I must say my office mates, Abhinav, Abhishek and Bruce made my stay here at Purdue more enjoyable. It is hard to imagine how the Ph.D. course would go without my soul sisters, Soojin, Kyungmin and Hye-ran.

Thanks to my family for providing unconditional support and encouragement throughout the course. I would like to especially thank my husband, Sehyun, for his love and support during the journey.

TABLE OF CONTENTS

LIST OF TABLES.....	8
LIST OF FIGURES	9
ABSTRACT	13
1. INTRODUCTION.....	15
1.1 Multiscale Riverbed Morphology and Hyporheic Exchange	21
1.2 Hydrodynamics and Hyporheic Exchange	22
1.3 Boulder-driven Hyporheic Exchange.....	23
1.4 Neural networks for predicting the bed pressure	24
1.5 References.....	26
2. RESEARCH QUESTIONS, STATEMENTS AND OBJECTIVES	34
2.1 How does the fractal dimension of riverbed morphology affect HE processes?	34
2.2 How are the hydrodynamic and hydrostatic drivers of HE related?	34
2.3 How do the spacing and embeddedness of boulders control HE?	34
2.4 Can we predict the pressure across the bed using point velocities?.....	35
3. THEORETICAL BACKGROUND	36
3.1 Navier-Stokes equations for incompressible, Newtonian fluid	36
3.1.1 Conservation of mass	36
Volume of Fluid (VoF) Method.....	36
3.1.2 Conservation of momentum.....	37
3.2 Reynolds-averaged Navier-stokes (RANS) equations.....	38
3.2.1 Eddy viscosity approximation.....	38
3.3 Porous flow modeling	39
3.4 Solute transport modeling.....	40
3.4.1 Fokker-Planck-Kolmogorov Equation (FPKE)	40
3.4.2 Residence time	40
3.5 References.....	41
4. THE SENSITIVITY OF HYPORHEIC EXCHANGE TO FRACTAL PROPERTIES OF RIVERBEDS	42
4.1 Fractal riverbed profiles.....	43

4.1.1	Previous Observations of Riverbeds and their Fractal Characterization.....	44
4.1.2	Generation of Synthetic Riverbeds based on Observations	45
4.2	Simulation conditions	47
4.3	Results and Discussion	48
4.3.1	Modeled pressure and flow fields.....	48
4.3.2	Effects of Topography on Hyporheic Flux	50
4.3.3	Effects of Topography on Residence Time Distributions	51
4.4	Discussion.....	54
4.5	Summary and Conclusions	56
4.6	References.....	56
5.	HYPORHEIC EXCHANGE THROUGH DUNES IN HIGH FROUDE NUMBER CHANNEL FLOWS WITH A FREE WATER SURFACE.....	61
5.1	Generation of synthetic riverbed morphology.....	62
5.2	Simulation conditions	63
5.3	Model validation	64
5.4	Results.....	65
5.4.1	Water surface profiles and surface flow fields	65
5.4.2	Hyporheic flux	69
5.5	Discussion.....	70
5.6	Summary and conclusions	72
5.7	References.....	73
6.	BOULDER-DRIVEN HYPORHEIC EXCHANGE	75
6.1	Boulder array configuration and Hydraulic conditions	75
6.2	Experimental setup and boundary conditions.....	76
6.3	Result	78
6.3.1	Effect of boulder array configuration on the flow field	78
6.3.2	Pressure variation across the sediment bed and interfacial flux	80
6.3.3	Solute transport and residence time distribution.....	82
6.4	Discussion.....	84
6.5	Summary and conclusions	85
6.6	References.....	86

7. PREDICTING CHANNEL BED PRESSURE USING POINT VELOCITY DATA WITH DATA-DRIVEN MODELS	89
7.1 Methods	89
7.1.1 Multivariate Linear Regression (MLR).....	90
7.1.2 Local Multivariate Linear Regression (LMLR).....	90
7.1.3 Artificial Neural Networks (ANNs)	91
7.2 Result and discussion	92
7.3 Summary and conclusions	96
8. SUMMARY AND CONCLUSIONS	97
PUBLICATION.....	100

LIST OF TABLES

Table 6.1. Embeddedness and corresponding Reynolds number (Re_h). Re_h decreases as the boulder more embedded.	78
Table 7.1. Performance of multivariate linear regression (MLR), local multivariate linear regression (LMLR), and artificial neural network (ANN) for test data. The cases where the MLR and LMLR show the best performance are colored in light orange. ANN produces consistent and accurate prediction performance under various conditions (light blue).	93

LIST OF FIGURES

Figure 1.1. Toth's flow: Toth showed how the variation in topographic elevation of water table in a small basin drives groundwater flows at multiple scales.	16
Figure 1.2. (a) Thibodeaux and Boyle (1987) observed that flow over bedforms induces pressure imbalances across the sediment bed generating significant and nested convection flow inside the porous bed sediment region (b) A similarity in flows passing over bedforms and cylinders: the pressure at the wall becomes maximum when the flow direction is perpendicular to the surface of the wall, and the pressure would drop down as the flow is accelerated while climbing up the roughness object (adapted from Thibodeaux and Boyle, 1987)	17
Figure 1.3. The broad regime of hyporheic flow with spatial scales of hyporheic flow paths ranging from millimeters or centimeters to meters or kilometers. The temporal scales also variously range from seconds to tens of years (adapted from Boano et al., 2014)	20
Figure 4.1. Illustration of the sequentially coupled surface-subsurface model framework. The channel flow field was calculated using OpenFOAM. The interfacial pressure fields from OpenFOAM simulations were used as the upper boundary to solve the groundwater flow field using FEniCS.	42
Figure 4.2. Types of low Froude number bedforms that are typically present as channel flow velocity increases: (a) typical ripple pattern ($0.1 < Fr < 0.3$), (b) compound dunes ($0.3 < Fr < 0.6$), and (c) dunes ($0.6 < Fr < 0.84$) The sketch of bedforms were adapted from Simons & Richardson (1966). The upper and lower limit of Froude number for each configuration is roughly estimated by the depth/velocity diagrams suggested by Southard and Boguchwal (1990) illustrating the fields of bedforms stability for grain size = 0.4 – 0.6 mm.	43
Figure 4.3. Measured bedforms and their characteristics: (a) Cross section of two sand beds generated in a flume and (b) Schematic power spectra of the elevation profiles, showing the location of the scaling regime between the wavelengths q_r and q_c , which corresponds to the spectral density C_{qr} and C_{qc} (original figure in Aubeneau et al., 2015). Note the steeper slope for the smoother dunes and the higher spectral density for the larger dunes compared to the smaller compound dunes. (c) Behavior of the phase for increasing wavelengths. Note the linear increase that we use to generate realistic artificial profiles.	44
Figure 4.4. Bed profile of (a) Case C_q (b) Case D and power spectral density of (c) Case C_q (d) Case D (e) Phases for both C_q and D cases. The C_q cases show the effect of maximum power spectral density or the amplitude of bedform whereas the D cases show the impact of fractal dimension of riverbeds. The phase of the signal is artificially generated to have a large variance up to the roll-off frequency and then increase linearly afterwards.	46
Figure 4.5 Channel flow velocity and subsurface hydraulic head for all cases: (a) ~ (f) for C_{q1} ~ C_{q6} , (g) ~ (l) for $D1$ ~ $D6$. The surface flow is consistent throughout simulations (0.3 m/s, 1 m water depth). The flow separation starts revealing in (d) C_{q4} , and becoming prominent in (e) C_{q5} and (f) C_{q6} . The occurrence of flow separation depends on the size of bedform. In the C_q cases, the hydraulic head equipotential lines under a local bedform are combined (smaller and smoother	

gradients) as bedform size grows ($C_q1 \rightarrow C_q6$) whereas they tend to split apart (spatially complex and steeper gradients) as fractal dimension increases ($D1 \rightarrow D6$)49

Figure 4.6 Pressure at the sediment-water interface and riverbed elevation for (a) C_q1 (b) C_q6 (c) $D1$ (d) $D6$. The pressure field is closely related to the morphology of riverbeds when the bedform size is small (e.g. (a), (c)). In the cases with large bedforms, they are not directly related due to the flow separation (e.g. (b), (d)).50

Figure 4.7 Hyporheic exchange with respect to (a) Maximum power spectrum density, C_q (logarithmic function) (b) Fractal dimension, D (exponential function) (c) Surface roughness, $\delta 2$ (logarithmic function). Hyporheic flux increases with increasing $\delta 2$, and this increase happens more rapidly for the D cases than the C_q cases.51

Figure 4.8 Fraction remaining in the bed (R) for (a) C_q cases and (b) D cases; Residence time distribution for (c) C_q cases and (d) D cases; The shortest and average residence time for (e) C_q cases and (f) D cases. A couple of inflection points are shown in (a) ~ (d) due to the stagnation point trapping particles for a while and then later releasing them. Both the shortest and average residence times decrease as C_q or D increases for the large bedforms because these increase flow velocity.53

Figure 5.1 A sequentially coupled surface-subsurface model: Both the channel (surface) flow and groundwater (subsurface) flow were solved using OpenFOAM. The pressure values from the channel flow simulations were imposed at the upper boundary of groundwater which is the sediment-water interface. We compare two different simulations, one with fixed water surface and the other with free water surface, in terms of the channel flow field, total head at the sediment-water interface and hyporheic flux under various flow conditions. We hypothesize (1) the hydrostatic pressure would increase at the dune trough and decrease at the dune peak generating larger head gradient when the water is free to move and (2) the frictional force between air-water would change the velocity field for the flow with free-surface flow.61

Figure 5.2 Riverbed morphology generated from Jerolmack and Mohrig (2005) with the following parameters: $\Delta x = 0.1, \Delta t = 0.002, A = 4.3, B = 4.3, D = 0.025, \zeta = 0.1, n = 1.5, p = 0.4$. The length and height of dune are rescaled to 1.4 m and 0.1 m, respectively. (a) The plan view (x - y) of the riverbed profile (b) The cross-sectional view (x - z) of the riverbed profile.62

Figure 5.3 The riverbed elevation (Yellow line with asterisks) along with the measured (magenta circle) and simulated water surface profile (Blue solid line): the simulated profile shows a good agreement with the measured profile.64

Figure 5.4 The measured (Blue circle) and simulated flow velocity (orange solid line) profiles where z^* is the elevation normalized by the water depth at location 1 and U^* is the velocity normalized by the depth-averaged flow velocity. The blue line represents the water surface elevation. The simulated flow velocity shows a good agreement with the experiment data.65

Figure 5.5 The channel velocity field with free-surface (surface flow, upper domain) and dynamic pressure field (subsurface flow, lower domain) are depicted for various flow conditions: $Fr_{avg} =$ (a) 0.06 (b) 0.17 (c) 0.29 (d) 0.41 (e) 0.52 (f) 0.64 (g) 0.76 (h) 0.87. White lines represent the flowpath in both surface and subsurface domain. In the surface domain, the total head for the fixed-surface case (Red) and for the free-surface case (Purple) are drawn along with bedform elevation (solid black line). The dotted black line indicates the critical depth and the asterisks (*) local flow regime

changes (e.g. sub→sup, sup→sub) wherever this line intercepts the water level. We observe an increase in flow velocity near the bed inducing a large head drop at the peak when the water surface is free to move.....67

Figure 5.6 The vertical velocity profile of channel flow at the peak of the dune for fixed-surface (blue dotted line) and free-surface case (orange solid line) for various flow conditions: Fr_{avg} = (a) 0.52 (b) 0.64 (c) 0.76 (d) 0.87. The upper x-axis represents the magnitude of horizontal velocity (green) and the lower x-axis is x-dir distance (purple). When the water surface elevation is fixed, the velocity profile at the dune peak is distributed in a way that the velocity is zero at the sediment bed and has maximum value at the water-air interface. In the free-surface case, the location where the velocity is maximum moves closer to the bed (away from the surface) at high Froude number.68

Figure 5.7 Relationship between the average Froude number (Fr_{avg}) and the normalized hyporheic flux (q_{int}/U). The hyporheic flux increases linearly with Fr_{avg} in fixed surface case (blue circular dots, a linear regression line (skyblue dotted line) $= 2.69 \times 10^{-5}x$, $R^2 = 0.9993$). In free-surface case, the power-law fitting curve is $y = 3.77 \times 10^{-5}x^{1.17}$ (R-squared: 0.9482, RMSE: 1.67×10^{-6}) for the former 5 cases70

Figure 6.1 A conceptual diagram of a coupled surface-subsurface system with a boulder array with $S = 5$, $E = 35\%$. h (surface flow water depth) = 0.3 m, h_g (Groundwater depth) = 1 m. (a) A geometry of a roughness element modelled by an ellipsoid having a ratio of axial diameters, $D_x : D_y : D_z = 10 \text{ cm} : 8 \text{ cm} : 6 \text{ cm}$. (b) An example of computational domain for As S increases, the distance between two adjacent boulders increases. As E increases, the boulder is more embedded into the sediment bed.76

Figure 6.2 Channel flow fields depicted with three-dimensional streamlines colored with the magnitude of the velocity with various spacing (S) and embeddedness (E) conditions: (a) $S = 2$, $E = 5\%$ (b) $S = 3$, $E = 5\%$ (c) $S = 7$, $E = 5\%$ (d) $S = 2$, $E = 50\%$ (e) $S = 3$, $E = 50\%$ (f) $S = 7$, $E = 50\%$ (g) $S = 2$, $E = 80\%$ (h) $S = 3$, $E = 80\%$ (i) $S = 7$, $E = 80\%$. For the cases with large embeddedness, the recirculation zone would disappear as the flow is hardly detached at the boulder's crest regardless of the distance between boulders. For the cases with small embeddedness, the recirculation vortex is observed in both closely- and loosely-packed cases, but the size of vortex was smaller and less coherent in the closely-packed case.79

Figure 6.3 The pressure distribution over the sediment bed for various boulder embeddedness (E) with constant spacing (S), $S = 7$, (a) $E = 5\%$ (b) $E = 20\%$ (c) $E = 35\%$ (d) $E = 50\%$ (e) $E = 65\%$ (f) $E = 80\%$ (g) $E = 95\%$. The size of both high- and low-pressure zone is larger and spread out across the sediment bed when the boulder embeddedness is small. The small embeddedness also produces more complicated low-pressure variation since an additional factor, a funnel vortex, contributes to the flow acceleration near the bed.80

Figure 6.4 The dependence of hyporheic flux on (a) Embeddedness (E) and (b) Spacing (S). The interfacial flux increases as the embeddedness decreases and as the spacing increases except for the case with the smallest spacing. This implies there is nonlinear dynamics between the spacing and embeddedness contributing to the exchange rate between surface and subsurface domain...82

Figure 6.5 The normalized solute mass inside the bed (a) with different spacings (S) while the embeddedness is the smallest, $E = 1$ and (b) with different embeddednesses (E) while the spacing

is the smallest, $S = 2$. The average residence time decreases as the embeddedness increases. As the boulder is embedded, the lateral movement of tracer becomes dominant making the path shorter, reducing the residence time of solute in the bed.83

Figure 6.6 Tracer paths of solute released at the centerline of the sediment bottom: for various boulder embeddedness (E) settings with constant spacing ($S = 1$): (a) $E = 5\%$ (b) $E = 20\%$ (c) $E = 35\%$ (d) $E = 50\%$ (e) $E = 65\%$ (f) $E = 80\%$ (g) $E = 95\%$. As the boulder embeddedness increases (b, c), the path starts to move in lateral direction as the streamwise route is hindered by the submerged boulder. As the boulder is more embedded (e, f, g), the lateral movement of tracer becomes dominant making the path even shorter, reducing the residence time of solute in the bed.84

Figure 7.1. (a) The normalized pressure obtained from CFD simulation (b1) ~ (d3) The normalized difference between the model output and target data for Case 1 which uses 70% of data for training and 30% of data for test. The boulder is depicted as a black ellipse. The highest error is observed upstream and near the boulder. While LMLR and ANN are able to model the general shape of pressure distribution, MLR barely captures the variation of pressure where the error plot shows almost the same pattern as the actual pressure. Still, LMLR is not able to predict the extreme change in pressure near the boulder unlike ANN. This is because of underfitting meaning that LMLR cannot represent the data having nonlinear structures.95

ABSTRACT

Hyporheic exchange is key to buffer water quality and temperatures in streams and rivers, while also providing localized downwelling and upwelling microhabitats. In this research, the effect of geomorphological parameters on hyporheic exchange has been assessed from a physical standpoint: surface and subsurface flow fields, pressure distribution across the sediment/water interface and the residence time in the bed.

First, we conduct a series of numerical simulations to systematically explore how the fractal properties of bedforms are related to hyporheic exchange. We compared the average interfacial flux and residence time distribution in the hyporheic zone with respect to the magnitude of the power spectrum and the fractal dimension of riverbeds. The results show that the average interfacial flux increases logarithmically with respect to the maximum spectral density whereas it increases exponentially with respect to fractal dimension.

Second, we demonstrate how the Froude number affects the free-surface profile, total head over sediment bed and hyporheic flux. When the water surface is fixed, the vertical velocity profile from the bottom to the air-water interface follows the law of the wall so that the velocity at the air-water interface has the maximum value. On the contrary, in the free-surface case, the velocity at the interface no longer has the maximum value: the location having the maximum velocity moves closer to the sediment bed. This results in increasing velocity near the bed and larger head gradients, accordingly.

Third, we investigate how boulder spacing and embeddedness affect the near-bed hydrodynamics and the surface-subsurface water exchange. When the embeddedness is small, the recirculation vortex is observed in both closely-packed and loosely-packed cases, but the size of vortex was smaller and less coherent in the closely-packed case. For these dense clusters, the inverse relationship between embeddedness and flux no longer holds. As embeddedness increases, the subsurface flowpaths move in the lateral direction, as the streamwise route is hindered by the submerged boulder. The average residence time therefore decreases as the embeddedness increases.

Lastly, we propose a general artificial neural network for predicting the pressure field at the channel bottom using point velocities at different level. We constructed three different data-driven models with multivariate linear regression, local linear regression and artificial neural network. The input variable is velocity in x , y , and z directions and the target variable is pressure at the

sediment bed. Our artificial neural network model produces consistent and accurate prediction performance under various conditions whereas other linear surrogate models such as linear multivariate regression and local linear multivariate regression significantly depend on input variable.

As restoring streams and rivers has moved from aesthetics and form to a more holistic approach that includes processes, we hope our study can inform designs that benefit both structural and functional outcomes. Our results could inform a number of critical processes, such as biological filtering for example. It is possible to use our approach to predict hyporheic exchange and thus constrain the associated biogeochemical processing under different topographies. As river restoration projects become more holistic, geomorphological, biogeochemical and hydro-ecological aspects should also be considered.

1. INTRODUCTION

Freshwater only accounts for 3% of global waters, but is essential for life. Rivers carry less than 1% of that freshwater, but are vital corridors transferring water, nutrients and sediment across landscapes, from mountains to oceans. Flowing waters interact with the surrounding alluvium: they are sustained by the adjacent aquifers that they sometimes also recharge. This bilateral exchange between surface and groundwater spans many scales, from entire regions to local processes at the grain scale (Stanford and Ward, 1988, 1993; Buffington and Tonina, 2009). The hyporheic zone (HZ) is a region near riverbeds where porous-media-flows are driven by the forces at the sediment / surface-water interface. Hyporheic zones are hotspots for ecohydrology and biogeochemistry, harboring the biofilms that regulate the cycling of major elements such as carbon, nitrogen and phosphorus (Triska et al., 1989; Mulholland et al., 1997; Battin et al., 2008).

Orghidan first coined the term Hyporheic zone, from the Greek prefix “hypo” meaning under and the root “rheos” meaning flow. Hyporheic flow is the flow that enters the sediment from the surface water and returns to the surface (Harvey et al., 1996; Winter et al., 1998; Storey et al., 2003; Gooseff, 2010). Hyporheic exchange includes the dissolved load and its organic and inorganic compounds. Upwelling water returning to the surface is enriched in reduced species while downwelling surface-water is usually rich in dissolved oxygen. The oxygen is used by the hyporheic microbiome to combust (i.e., respire) organic matter. After the available oxygen is used, other species such as nitrates provide the oxidative power that fuels the redox processes.

Since Toth’s pioneering research (Toth, 1963), many others have studied the physics of groundwater-surface water interaction. Toth showed how the variation in topographic elevation of water table in a small basin drives groundwater flows at multiple scales (Figure 1.1). He approximated the water table as a combination of three components which are constant, linear and sinusoidal functions under the assumption the water table is in-phase with the land surface (Meneley, 1963; King 1892; Meinzer 1923; Wisler and Brater, 1959). The ‘three well pronounced vertical zones of groundwater flow’, namely local, intermediate, and regional systems, are observed in his model. Their characteristics are explained in Norvatov and Popov (1961) as follows: (1) ‘Upper zone of active flow, whose geographical zonality coincides with climatic belts. The lower boundary of this zone coincides with the local base levels of rivers; (2) ‘medium zone of delayed flow, subject to lesser climatic effect but also geographically zonal. The lower boundary

of this zone is the base level of large rivers; (3) ‘lower zone (of relatively stagnant water), geographically azonal and lying below the base level of large stream systems.’.

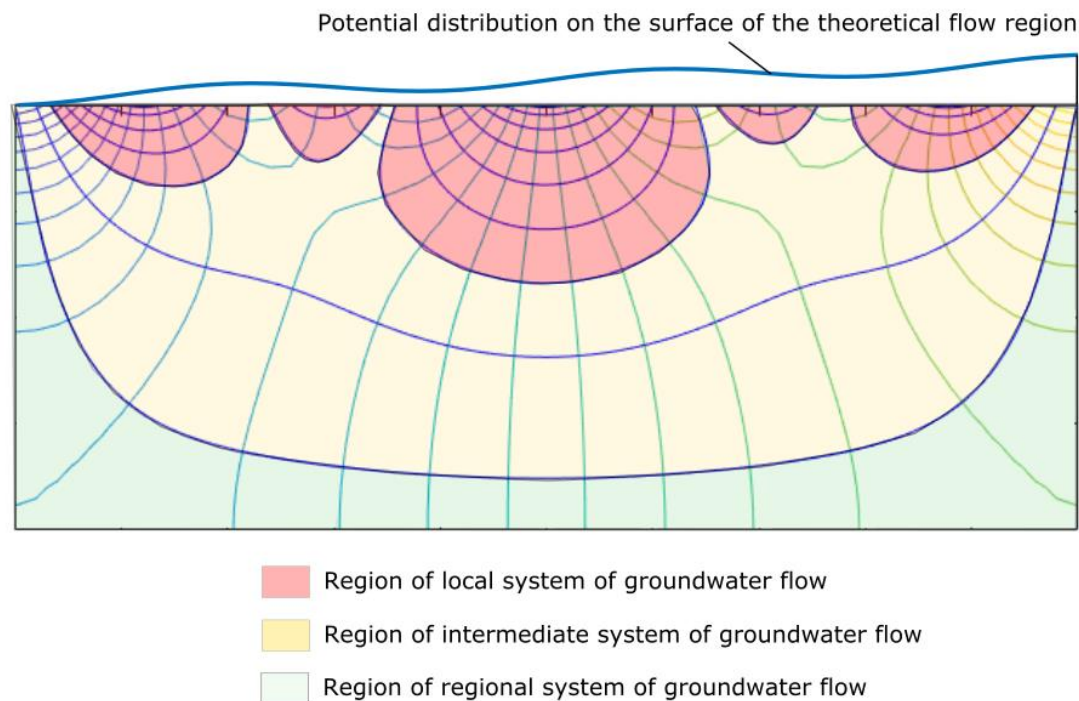


Figure 1.1. Toth's flow: Toth showed how the variation in topographic elevation of water table in a small basin drives groundwater flows at multiple scales.

As new model interpretations were developed, the hydrologic exchange with stream waters and slowly moving waters confined in “dead zones”, was quantified by dye tracer experiments (Hays, 1966; Hays et al., 1966). It is assumed that (1) dead zones are stagnant compared to the streamwise channel flow and (2) the exchange between surface and dead zones water is proportional to the concentration gradient between the channel and storage zone. Many effective transport models, lumping all actual slow zones into a single conceptual dead zones were proposed in the 60ies and 70ies (Coates, 1966; Valentine and Wood, 1977; Thackston and Schnelle, 1970). Bencala and Walters (1983) applied such a model to solute transport in Uvas creek and coined the term transient storage model, replacing dead zones in the vocabulary.

A more mechanistic model of hyporheic exchange, conceptually reminiscent of Toth flows, was put forth by Thibodeaux and Boyle (1987). They observed that flows over bedforms induce pressure imbalances across the sediment bed generating significant and nested convection flows inside the porous bed (Figure 1.2a). Such flows over bedforms are similar to the classic flows

around cylinders studied in fluid mechanics classes: pressure increases as flow accelerates while climbing up the roughness (Figure 1.2b). From this analogy, they proposed an early model of convective hyporheic exchange: ‘the total pressure gradient is the sum of the wave contribution and the hydraulic gradient (slope of the water surface) contribution:’. The ‘wave contribution’ driven by the pressure drop across the bedform is approximated by $c_p \rho V^2 / \lambda$ where c_p is a pressure coefficient, ρ is the density of water, V is the average convective velocity, and λ is the wavelength of a bedform. The pressure gradient due to the hydraulic gradient is $\rho g s$ where g is gravitational acceleration and s is the slope of the water surface. They further apply Darcy’s law to estimate the porous flow velocity: $V_0 = K / \nu (c_p V^2 / \lambda + g s)$ where K is the permeability of the bed sediment and ν is the kinematic viscosity of water. It follows from the analysis that hyporheic exchange caused by topography is proportional to the Froude number (V^2), the hydraulic conductivity of the alluvium (K) and inversely proportional to the size (wavelength) of the bedforms.

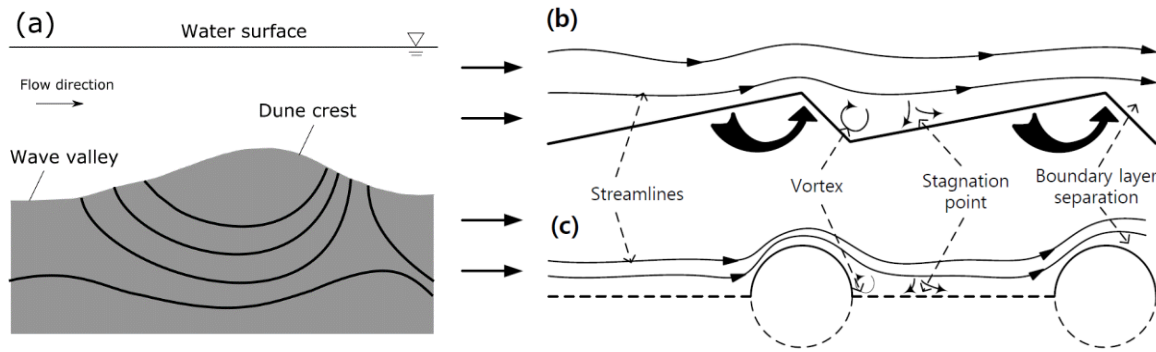


Figure 1.2. (a) Thibodeaux and Boyle (1987) observed that flow over bedforms induces pressure imbalances across the sediment bed generating significant and nested convection flow inside the porous bed sediment region (b) A similarity in flows passing over bedforms and cylinders: the pressure at the wall becomes maximum when the flow direction is perpendicular to the surface of the wall, and the pressure would drop down as the flow is accelerated while climbing up the roughness object (adapted from Thibodeaux and Boyle, 1987)

Elliott and Brooks (1997) investigated the mechanisms and surface/subsurface exchange for sediment beds by conducting laboratory experiments under steady and uniform hydraulic conditions and his theoretical and experimental work remains a cornerstone of our fundamental understanding of bedform-driven hyporheic exchange. He used a formula to calculate dynamic head deviation based on experimental measurements of head over triangular solid shapes, $h_m = 0.28(V^2/2g)(H/0.34d)^n$ where H is the bedform height, d the water depth, and n is a constant

determined by H/d (e.g. $n = 3/8$ for $H/d \leq 0.34$ and $n = 3/2$ otherwise), and this formula has been widely used since to estimate the head drop across the bed. The head in this formula (and by extension the amount of exchange) is still proportional to the Froude number, but also to the flow restriction caused by the bedform.

As computational fluid dynamics (CFD) simulations became less expensive and more feasible, CFD has been utilized in estimating the channel flow field and pressure distribution across the sediment bed (or riverbed). CFD is capable of simulating turbulent flow and reduces laboratory/field experiment costs. Cardenas and Wilson (2007) first applied CFD simulation for channel flow and used the pressure distribution at the sediment bed to simulate hyporheic flow. Reynolds-Averaged Navier-Stokes equations were used to solve the surface flow field and the resulting pressure values across the sediment bed are fed to the upper boundary of a groundwater domain, where flow is modelled by Darcy's law. Eddies generated by the bedform affects the near-bed hydrodynamics altering the locations where the maximum/minimum pressure occurs. As the slope of dune (ratio of height to wavelength) gets steeper, the detachment length becomes longer and the interfacial exchange zone is thus shallower.

CFD is also useful to simulate complex morphologies such as pool-riffle systems or various natural objects that cannot be included in analytical models. Sawyer et al. (2011) investigated the hyporheic exchange driven by a channel-spanning log. She used Reynolds-averaged Navier-stokes (RANS) turbulence model to simulate stream flow structures such as eddies and flow circulation behind the log. The water surface elevation was estimated with a Volume of Fluid (VoF) method, which is an air-water mixture model. The simulated head along the bed shows good agreement with the flume experiments. Results demonstrate the pressure difference between upstream and downstream of a log drives the hyporheic exchange. Trauth et al. (2013) studied the interaction between turbulent channel flow and hyporheic flow over pool-riffle sequences under various groundwater conditions using RANS model along with VoF method as well and these tools are now becoming the norm to study hyporheic exchange.

Large-eddy simulation (LES) has been adopted for research which requires detailed flow structures or when the channel flow is in transitional state. Scalo et al. (2013) developed a dissolved oxygen (DO) surface/subsurface transport model under a transitional oscillatory channel flow based on LES. They used LES in order to represent the flow transition from a quasi-laminar to a fully turbulent accurately, which is difficult to achieve with RANS model. LES produces a reliable

estimation of the sediment-oxygen uptake (SOU) as it resolves the full range of solute transport processes. Han et al. (2018) used LES to deal with rough and permeable beds composed of arranged particles when simulating the solute transfer from stream water to sediment beds. Recently, Lian et al. (2019) simulated turbulent stream flows with LES model over a matrix of spheres submerged in the water in order to represent the porous water flow near the interface. LES model has shown the ability to capture the turbulent flow characteristics over rough and permeable bed.

Recently, direct numerical simulations (DNS) has been used to fully resolve turbulent flow in an open channel and simulate associated hyporheic exchange processes. Shen et al. (in-press) used DNS to demonstrate the detailed effects of bed roughness in terms of scalar and momentum transfer including turbulent structures and averaged flow statistics. Consequently, the random interface produces significantly higher hyporheic flux than the regular one. Sherman et al. (2019) proposed a dual domain coupled model that estimates transport processes in open channels with hyporheic exchange. They compared breakthrough curve (BTC) predictions from the model with results obtained from DNS. They also utilized the spatio-temporally averaged DNS velocity and diffusivity profiles to parameterize the open channel flow to create joint probability density distributions of particle travel times and distances.

Figure 1.3 illustrates the broad regime of hyporheic flow with spatial scales of hyporheic flow paths ranging from millimeters or centimeters (Elliott and Brooks, 1997; Marion et al., 2002; Tonina and Buffington, 2007) to meters or kilometers. The temporal scales also variously range from seconds to tens of years (Stanford and Ward, 1988; Wondzell and Swanson, 1996; Harvey and Wagner, 2000; Cardenas et al., 2004; Boano et al., 2006; Wörman et al., 2007; Revelli et al., 2008; Hester and Doyle, 2008). This research focuses on the range where the dynamics of bio-fluvial-geomorphic influences govern ranging from ripples to pool-riffle system. We especially look at the “transitional” state in terms of geomorphology and hydrodynamic conditions. This research aims to understand how the hyporheic exchange processes alter as geomorphic or hydrodynamic conditions change. By achieving this, we want to build a bridge between small scale and large scale under natural system which always changes.

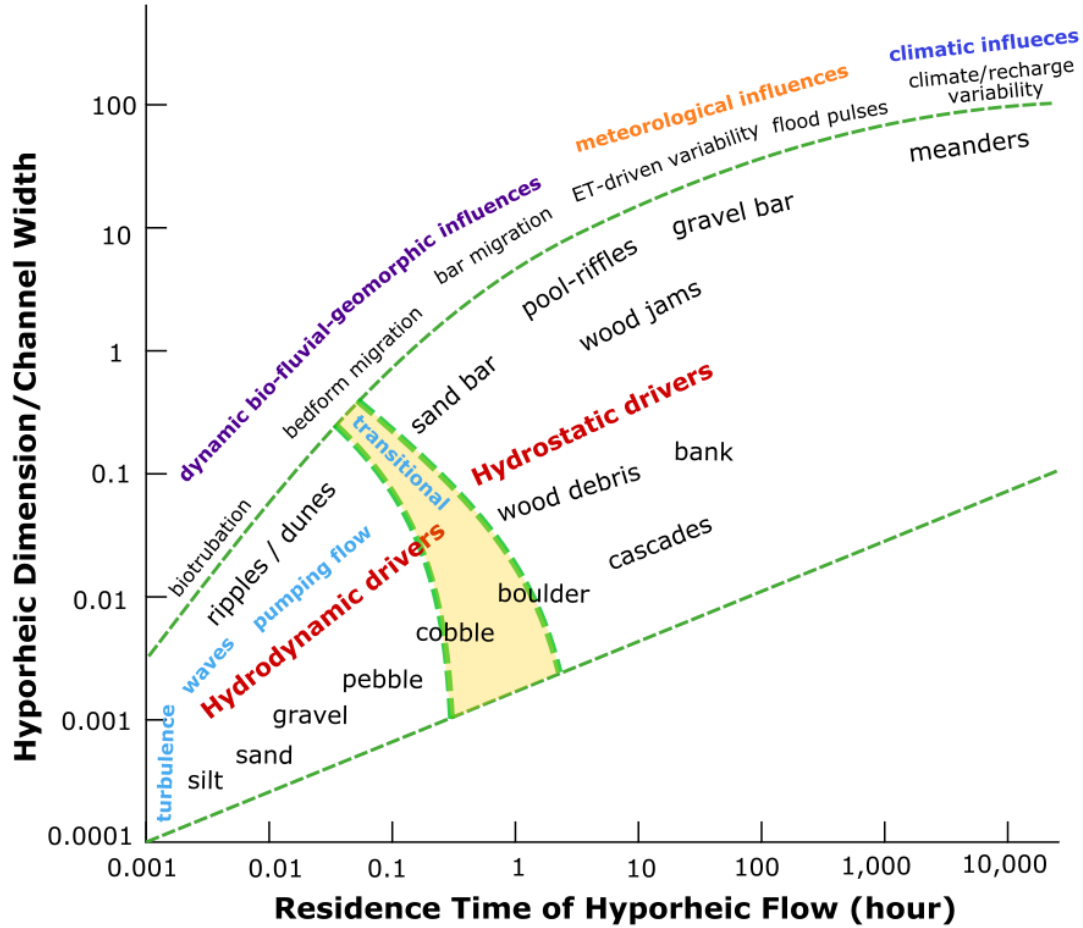


Figure 1.3. The broad regime of hyporheic flow with spatial scales of hyporheic flow paths ranging from millimeters or centimeters to meters or kilometers. The temporal scales also variously range from seconds to tens of years (adapted from Boano et al., 2014)

This thesis is composed of four different topics which are under the transitional states in terms of either geomorphology or hydrodynamics. The next sections in this chapter introduce each topic in more detail. Briefly, in chapter 4, we investigate the effect of surface roughness (the scaling of bedform topography) on hyporheic exchange. In chapter 5, we study how the Froude number affects the exchange of water between surface and subsurface when the water surface is fixed and when it is allowed to adjust. In chapter 6, we discuss how boulder spacing and embeddedness affect the near-bed hydrodynamics and hyporheic exchange. Finally, in chapter 7, a surrogate model relating point velocities to pressure at the sediment bed is developed using neural networks. A general procedure of chapter 4, 5, and 6 is (1) generate a channel topography, (2) simulate channel flow with CFD modeling, (3) solve for groundwater flow using the pressure

values obtained from CFD simulate, and (4) simulate the solute transport inside the hyporheic zone. We assess the hyporheic exchange process in terms of interfacial flux and residence time distribution of solute in the hyporheic zone.

1.1 Multiscale Riverbed Morphology and Hyporheic Exchange

Morphology driven hyporheic flows are inherently multiscale, with local head gradients influenced by features ranging from the grain scale to the regional topography (Wörman et al., 2007; Cardenas et al., 2008; Buffington and Tonina, 2009; Boano et al., 2014). Hyporheic exchange due to multiscale riverbed morphology has been studied previously (Stonedahl et al., 2012, 2013; Gomez-Velez and Harvey, 2014; Wörman et al., 2006, 2007; Aubeneau et al., 2015). Stonedahl et al. (2010) developed a multiscale model that included ripples, dunes and meanders and compared the residence time distributions in hyporheic zones associated with each feature. Wörman et al. (2006) showed that a hyporheic flow field could be calculated from the Fourier series representing riverbed elevation, and similarly showed the scaling of groundwater flow fields from the local to continental scale. Aubeneau et al. (2015) showed that the scaling of topography produced the scaling in residence time distributions in flume experiments, hinting at the importance of a relationship between the fractal dimension of riverbeds and their corresponding transit time distributions.

Fractals are pervasive in nature, from coastlines, to snowflakes, to river networks (Mandelbrot, 1983). Fractal scaling is also observed in riverbed topography both in models (Turcotte, 1997; Jerolmack and Morhig, 2005) and in observed elevation profiles (Hino, 1968; Burrough, 1981; Robert, 1988; Coleman and Nikora, 2011; Martin and Jerolmack, 2013). The observed scaling of natural bedforms corresponds to Hurst exponents between 0.5 under transient conditions and 1 at equilibrium (Nikora and Hicks, 1997; Jerolmack and Mohrig, 2005). Nikora et al. (2019) used artificial bed models with varied topographic scaling and showed how surface roughness is associated with friction factor and hydraulic resistance. In hyporheic exchange studies, random bedform fields have used white noise, where the spectral density is constant (Elliott, 1991), or equilibrium scaling, where the spectral slope is -3 (Stonedhal et al., 2013).

This study demonstrates the effect of fractal scaling of riverbed topography on hyporheic exchange. A set of synthetic fractal riverbeds with different scaling statistics was generated and used as inputs to sequentially-coupled numerical simulations of turbulent channel flow, hyporheic

flow. In the analysis, the maximum power spectrum (dune size) and the fractal dimension (topographic complexity) were considered as independent variables and we then investigated how interfacial fluxes and hyporheic travel times are functionally related to these variables. As the maximum power spectrum increases (i.e., dune height to flow depth ratio), the average interfacial flux increases logarithmically whereas it increases exponentially with an increase in fractal dimension. Hyporheic exchange is more sensitive to additional roughness (larger fractal dimensions) than to bedform size (larger maximum power). Our results imply that fractal properties of riverbeds are crucial to predicting hyporheic exchange.

1.2 Hydrodynamics and Hyporheic Exchange

The interaction of flow and sediment in rivers and streams shapes bedforms that in turn affect flow (Best, 2005; Venditti, 2013). Water accelerates on the stoss side upstream and slows down over the lee side downstream. Around the peak, flow separation can create recirculating zones in the lee side that affect head gradients over the sediment-water interface (SWI). Head gradients over the SWI force water in and out of the porous alluvium, defining a region known as the hyporheic zone. These interfacial zones are hotspots for ecohydrology and biogeochemistry, harboring the biofilms that regulate the cycling of major elements such as carbon, nitrogen and phosphorus (Triska et al., 1989; Mulholland et al., 1997; Battin et al., 2008).

Potential and kinetic energy gradients at the stream bottom boundary drive hyporheic exchange. The total head at the streambed includes the hydrostatic (pressure and elevation head) and the hydrodynamic head (mean velocity head and unsteady motions related to bed roughness generating Reynolds stresses and momentum transfers) (Boano et al., 2014). Although both hydrostatic and hydrodynamic heads contribute to hyporheic flow, the hydrostatic forces tend to be more influential when it is associated with the streambed's larger topographic features, such as bars, steps, cascades, riffles, and meandering banks, which can change water surface profile spatially (Harvey and Bencala, 1993; Woessner, 2000; Tonina and Buffington, 2009; Gooseff, 2010; Trauth et al., 2013). In contrast, the hydrodynamic head gradient is dominant in driving hyporheic flow when it is associated with relatively small-scale channel features, such as ripples and dunes, since the hydrostatic head changes little when the water surface is not perturbed. The hydrodynamic driving forces primarily depend on the flow conditions (e.g. the mean stream

velocity, Froude number, Reynolds number) whereas hydrostatic drivers are mainly influenced by the change in surface water elevation (SWE).

The classification of hyporheic exchange drivers by the size of topographic features has been used since the variation of water surface profile, which can be considered as an indicator of hydrostatic head gradient, depends on the riverbed elevation by basic principles of open channel flows: small features such as bedforms induce small water surface profile change and large features such as meandering banks cause large water surface profile variation. The modeling of hyporheic exchange driven by small features often ignores the variation in water surface profile (Cardenas and Wilson, 2007; Hardy et al., 2009; Chen et al., 2018). However, for flows having large Froude number (~ 0.5), macroturbulence caused by a flow separation in lee side can create boils on the water surface, affecting flow patterns and head distributions (Best, 2005). We hypothesize that shallower, faster flows near critical conditions may promote more hyporheic exchange than expected if the SWE is not allowed to adjust.

1.3 Boulder-driven Hyporheic Exchange

Debris and obstacles in streams and rivers are ubiquitous. Trees and wood clog waterways, blocks eroded from canyon walls tumble down to the valley floor, high flows leave behind cobble jams and bars, braided channels are but an obstacle... Examples are endless. Natural debris provide beneficial structural and functional diversity: more habitats harbor more species (Gorman and Karr, 1978; McGuinness and Underwood, 1986; Stoll et al., 2016), natural dams and large scale roughness dissipate energy (Pagliara and Chiavachini, 2006), head gradients around obstacles drive surface/subsurface exchange (Sawyer et al., 2011), buffering temperatures and improving water quality (Hutchinson and Webster, 1998; Sawyer and Cardenas, 2012; Briggs et al. 2013).

After decades of degrading lotic environments, river restoration has become a major endeavor, generating billions in business and occupying many water resources engineers and scientists (Wohl et al., 2015). Stream restoration often targets fish habitat and populations, but improving water quality has now become preponderant (Bernhardt et al., 2005). As the importance of the hyporheic zone in improving water quality has been recognized over the past twenty years (Fischer et al., 2005), incorporating near bed water mixing in the design of restoration projects could lead to healthier hydro-ecosystems (Hester and Gooseff, 2010; Palmer et al., 2014). Salmonid redds have been linked to strong interstitial flows that supply oxygen and prevent

clogging, and the connection between hyporheic flows and the breeding and survival of sensitive fish species is well documented (Cooper, 1965; Baxter and Hauer, 2000). We suggest that large stable features such as boulders intended to improve fish habitat could also increase hyporheic flows, hence further benefiting ecosystems by improving water quality.

If boulders influence the near-bed hydrodynamics, boulder clusters can also affect the surrounding flow fields (Yager et al. 2007). As boulders are closer, the wake they generate can extend to their neighbors and interfere with the wakes of the adjacent elements. Fang et al. (2017) investigated the effects of boulder concentration on hydrodynamics and turbulent flow properties. They showed that boulders influence the mean flow and the near bed turbulence, but also that the streamwise spacing played an important role on the surface flow field. In particular, when boulders were near each other, wake interference and skimming flow were observed, greatly reducing bed shear. Since spacing changes the near bed hydrodynamics, we expect it will also affect hyporheic exchange. More specifically, we hypothesize that hyporheic exchange will increase with boulder spacing as wake interference disappears.

Boulder embeddedness, the extent boulders are sunken into the stream bed (Barbour et al., 1999) is also expected to influence surface-subsurface water exchange. We hypothesize that boulder embeddedness will influence hyporheic exchange processes because (1) flow patterns will change with embeddedness (e.g. a whole sphere placed on the bed vs. a half-buried sphere) and (2) the embedded part of the boulder is impermeable and thus changes the makeup of the hyporheic zone. More specifically, we predict that embeddedness will shorten flowpaths and thus decrease residence times if the flux is the same. However, the flux is expected to decrease with embeddedness, as the more the boulders protrude in the surface flow, the more head gradients can drive hyporheic flows. It is possible that the increase in flux compensates the decrease in flowpath length, resulting in similar residence times.

1.4 Neural networks for predicting the bed pressure

Artificial neural networks (ANNs) have been widely utilized as a prediction and forecast model in various areas including aerospace, finance, manufacturing, medicine, water resources and environmental sciences. Although the basic principles of artificial neurons were introduced in 1940s, employments of ANNs have blossomed after the application of the back-propagation (BP) training algorithm for feedforward ANNs during 1980s, and advances in computer capability

accelerated the use of ANNs. More recently, data-driven and machine learning techniques have been applied for turbulence modeling in fluid dynamics. Numerical modeling of fluid flows primarily depends on solving the partial differential equation systems in a discretized form. approach, which is often computationally expensive.

As an early data-driven model, Willcox and Peraire (2002) suggested a use of model reduction method via the Proper Orthogonal Decomposition (POD) to represent the high-fidelity system (e.g. turbulent flow) with relatively small amount of basis vectors. The projection model reduction methods became popular tools in parameterizing dynamical systems and high fidelity models. On the other hand, ANN has been used as a surrogate model to represent the nonlinear relationship between flow variables (e.g. pressure, velocity, dynamic reattachment) (Faller et al., 1995; Bonakdari et al., 2011; Jin et al., 2018; Bhatnagar et al., 2019).

Over the decades, cost-effective surrogate models have been suggested as alternatives to resolve those challenges in water resources engineering (Cheng et al., 2002; Lin et al., 2006; Muttill and Chau, 2006; Muzzammil, 2008; Wu et al., 2008; Harter and Velho, 2010; Ghosh et al., 2010; Safikhani et al., 2011). Bhattacharya et al. (2007) applied neural networks in sedimentation modeling for the channel of the port area of Rotterdam. They used wave energy, flow discharge and sedimentation potential to predict the sedimentation. Bilgil and Altun (2008) estimated the friction coefficient of smooth open channels via ANN. The proposed ANN model outperformed the conventional method, Manning's equation, in predicting friction coefficient. Kocabas et al. (2008) suggested an ANN approach to predict the critical submergence of intake pipe for permeable and impermeable bottom. They compared ANN model with Multiple Linear Regression (MLR) approaches and the proposed ANN model showed more accurate prediction ability. Emiroglu et al. (2011) applied ANN to estimate the discharge capacity of triangular labyrinth side-weirs. Similar to Kocabas et al. (2008), they compared the performance of the ANN model with MLR models and ANN outperformed MLR.

In this study, we propose a general artificial neural network (ANN) based data-driven model for predicting the pressure field at the channel bottom using point velocities at different level. We constructed three different data-driven models with multivariate linear regression, local linear regression and ANN. The input variable is velocity in x, y, and z directions and the target variable is pressure at the sediment bed. We show that ANN based surrogate models can estimate the pressure field compared to other linear regression model. Comparing ANN with LMLR, ANN

predicted the pressure field across the bed more accurately than LMLR based on the point velocity data. Both ANN and LMLR are able to model the general trend of pressure variation, but only ANN captures the nonlinear relationship between the velocity and pressure near the boulder.

1.5 References

- Aubeneau, A. F., Martin, R. L., Bolster, D., Schumer, R., Jerolmack, D., and Packman, A. I. (2015). Fractal patterns in river morphology produce fractal scaling of water storage times. *Geophys. Res. Lett.*, 42, 5309–5315. <https://doi.org/10.1002/2015GL064155>
- Battin, T. J., Kaplan, L. A., Findlay, S., Hopkinson, C. S., Marti, E., Packman, A. I., et al. (2008). Biophysical controls on organic carbon fluxes in fluvial networks Metabolism. *Nature Geoscience*, 1.
- Barbour, M. T., Gerritsen, J., Snyder, B. D., and Stribling, J. B. (1999) Rapid Bioassessment Protocols for Use in Streams and Wadeable Rivers: Periphyton, Benthic Macroinvertebrates and Fish, Second Edition. EPA 841-B-99-002. U.S. Environmental Protection Agency; Office of Water; Washington, D.C.
- Baxter, C. V., and Hauer, F. R. (2000). Geomorphology, hyporheic exchange, and selection of spawning habitat by bull trout (*Salvelinus confluentus*). *Canadian Journal of Fisheries and Aquatic Sciences*, 57(7), 1470-1481.
- Bencala, K. E., and Walters, R. (1983), Simulation of solute transport in a mountain pool-and-riffle stream: A transient storage model, *Water Resour. Res.*, 19, 718–724, doi:10.1029/WR019i003p00718.
- Best, J. (2005). Kinematics, Topology and Significance of Dune-Related Macroturbulence: Some Observations from the Laboratory and Field. *Fluvial Sedimentology VII* , 41–60. doi: 10.1002/9781444304350.ch3
- Bhatnagar, S., Afshar, Y., Pan, S., Duraisamy, K. and Kaushik, S. (2019) Prediction of aerodynamic flow fields using convolutional neural networks. *Comput. Mech.* 64(2), 525–545
- Bhattacharya, B., Deibel, I. K., Karstens, S. and Solomatine, D. P. (2007). Neural networks in sedimentation modeling approach channel of the port area of Rotterdam. *Proceedings in Marine Science* 8:477-492
- Bilgil, A. and Altun, H. (2008). Investigation of flow resistance in smooth open channels using artificial neural networks. *Flow Measurement and Instrumentation* 19:404-408.
- Bonakdari, H., Baghalian, S., Nazari, F. and Fazli, M. (2011) Numerical Analysis and Prediction of the Velocity Field in Curved Open Channel Using Artificial Neural Network and Genetic Algorithm, *Engineering Applications of Computational Fluid Mechanics*, 5:3, 384-396, doi: 10.1080/19942060.2011.11015380

- Boano, F., Camporeale, C., Revelli, R. and Ridolfi, L. (2006), Sinuosity-driven hyporheic exchange in meandering rivers, *Geophys. Res. Lett.*, 33, L18406, doi:10.1029/2006GL027630.
- Boano, F., Harvey, J. W., Marion, A., Packman, A. I., Revelli, R., Ridolfi, L. and Wörman, A. (2014), Hyporheic flow and transport processes: Mechanisms, models, and biogeochemical implications, *Rev. Geophys.*, 52, 603–679, doi:10.1002/2012RG000417.
- Briggs, Martin A., Lautz, L. K., Hare, D. K., and González-Pinzón, R. (2013) Relating hyporheic fluxes, residence times, and redox-sensitive biogeochemical processes upstream of beaver dams. *Freshwater Science* 32.2, 622-641.
- Buffington, J. M. and Tonina, D. (2009) Hyporheic exchange in mountain rivers I: Mechanics and environmental effects. *Geography Compass*, 3(3):1063–1086, 2009. ISSN 17498198. doi: 10.1111/j.1749-8198.2009.00226.x.
- Bernhardt, E. S., Palmer, M. A., Allan, J. D., Alexander, G., Barnas, K., Brooks, S. et al. (2005) Synthesizing U.S. River Restoration Efforts. *Science*, 308(5722), 636-637.
- Burrough, P. A. (1981). Fractal dimensions of landscapes and other environmental data. *Nature*, 294, 240-242. <https://doi.org/10.1038/294240a0>
- Cardenas, M. B. (2008), Surface water-groundwater interface geomorphology leads to scaling of residence times, *Geophys. Res. Lett.*, 35, L08402, doi:10.1029/2008GL033753.
- Cardenas, M. B., and Wilson, J. L. (2007), Dunes, turbulent eddies, and interfacial exchange with permeable sediments, *Water Resour. Res.*, 43, W08412, doi:10.1029/2006WR005787
- Cardenas, M. B., Wilson, J. L., and Zlotnik, V. A. (2004), Impact of heterogeneity, bed forms, and stream curvature on subchannel hyporheic exchange, *Water Resour. Res.*, 40, W08307, doi:10.1029/2004WR003008.
- Chen, X., Cardenas, M. B., and Chen, L. (2018). Hyporheic Exchange Driven by Three-Dimensional Sandy Bed Forms: Sensitivity to and Prediction from Bed Form Geometry. *Water Resources Research*, 54 (6), 4131–4149. doi: 10.1029/2018WR022663
- Cheng, C. T., Ou, C. P. and Chau, K. W. (2002) Combining a fuzzy optimal model with a genetic algorithm to solve multi-objective rainfall–runoff model calibration. *Journal of Hydrology* 268:72–86.
- Coates, D. R. (1966) Glaciated appalachian plateau: till shadows on hills. *Science*, 152(3729), 1617-1618.
- Coleman, S. E. and Nikora, V. I. (2011). Fluvial dunes: initiation, characterization, flow structure. *Earth Surf. Process. Landforms*, 36: 39-57. <https://doi.org/10.1002/esp.2096>
- Cooper, A.C. (1965) The effect of transported stream sediments on survival of sockeye and pink salmon eggs and alevin. *Int. Pac. Salmon Fish. Comm. Bull.* 18, 1–71.

- Elliott, A. H. (1991) Transfer of solutes into and out of streambeds, (Doctoral dissertation). Retrieved from CaltechTHESIS. (<http://resolver.caltech.edu/CaltechETD:etd-07092007-074127>). Pasadena, CA: California Institute of Technology.
- Elliott, A. H., and Brooks, N. H. (1997), Transfer of nonsorbing solutes to a streambed with bed forms: Theory, *Water Resour. Res.*, 33, 123–136, doi:10.1029/96WR02784.
- Emiroglu, M. E. and Bilhan, O. and Kisi, O. (2011). Neural networks for estimation of discharge capacity of triangular labyrinth side-weir located on a straight channel. *International Journal of Expert Systems* 38:867-874.
- Faller, W., Schreck, S. and Luttges, M. (1994) Real-time prediction and control of three-dimensional unsteady separated flow fields using neural networks. AIAA, Aerospace Sciences Meeting and Exhibit, 32nd, Reno, NV; UNITED STATES; 10-13 Jan. 1994
- Fang, H. W., Liu, Y., and Stoesser, T. (2017) Influence of boulder concentration on turbulence and sediment transport in open-channel flow over submerged boulders. *Journal of Geophysical Research: Earth Surface*, 122, 2392–2410. <https://doi.org/10.1002/2017JF004221>
- Fischer, H., Kloep, F., Wilzcek, S., and Pusch, M. T. (2005). A river's liver—microbial processes within the hyporheic zone of a large lowland river. *Biogeochemistry*, 76(2), 349-371.
- Ghosh, S., Pratihar, D. K., Maiti, B. and Das, P. K. (2010). Optimum design of a two step planar diffuser: A hybrid approach. *Engineering Applications of Computational Fluid Mechanics* 4(3):415-424
- Gomez-Velez, J. D., and Harvey, J. W. (2014), A hydrogeomorphic river network model predicts where and why hyporheic exchange is important in large basins, *Geophys. Res. Lett.*, 41, doi:10.1002/2014GL061099.
- Gorman, O. T., and Karr, J. R. (1978). Habitat structure and stream fish communities. *Ecology*, 59(3), 507-515.
- Gooseff, M. N. (2010) Defining hyporheic zones - advancing our conceptual and operational definitions of where stream water and groundwater meet. *Geography Compass*, 4(8):945–955. ISSN 17498198. doi: 10.1111/j.1749-8198.2010.00364.x.
- Han, X., Fang, H., He, G. and Reible, D. (2018) Effects of roughness and permeability on solute transfer at the sediment water interface. *Water Research*, 129, 39-50. doi: 10.1016/j.watres.2017.10.049
- Hardy, R. J., Best, J. L., Lane, S. N., and Carbonneau, P. E. (2009). Coherent flow structures in a depth-limited flow over a gravel surface: The role of near-bed turbulence and influence of Reynolds number. *Journal of Geophysical Research: Earth Surface*, 114 (1), 1–18. doi: 10.1029/2007JF000970

- Harter, F. B. and Velho, H. F. C. (2010). Multilayer perceptron neural network in a data assimilation scenario. *Engineering Applications of Computational Fluid Mechanics* 4(2):237-245.
- Harvey, J. W. and Bencala, K. E. (1993). The Effect of streambed topography on surface-subsurface water exchange in mountain catchments. *Water Resources Research*, 29 (1), 89–98. doi: 10.1029/92WR01960
- Harvey, J. W., and Wagner, B. J. (2000), Quantifying hydrologic interactions between streams and their subsurface hyporheic zones, in *Streams and Ground Waters*, edited by J. A. Jones and P. J. Mulholland, pp. 3–44, Academic Press, San Diego, Calif.
- Harvey, J. W., Wagner, B. J., and Bencala, K. E. (1996) Evaluating the reliability of the stream tracer approach to characterize stream-subsurface water exchange. *Water Resources Research*, 2(8): 2441–2451.
- Hays, J. R. (1966), Mass transport phenomena in open channel flow, PhD dissertation, Dep. of Chemical Engineering, Vanderbilt Univ., Nashville, Tenn.
- Hays, J. R., Krenkel, P. A., and Schnelle, K. B. J. (1966), Mass-transport mechanisms in open-channel flow, Tech. Rep. 8, Sanit. and Water Resour. Eng., Dep. of Civ. Eng., Vanderbilt Univ., Nashville, Tenn.
- Hester, E. T., and Doyle, M. W. (2008), In-stream geomorphic structures as drivers of hyporheic exchange, *Water Resour. Res.*, 44, W03417, doi:10.1029/2006WR005810.
- Hester, E. T., and Gooseff, M. N. (2010). Moving beyond the banks: Hyporheic restoration is fundamental to restoring ecological services and functions of streams. *Environ. Sci. Technol.* 44, 5, 1521-1525
- Hino, M. (1968). Equilibrium-range spectra of sand waves formed by flowing water. *Journal of Fluid Mechanics*, 34(3), 565-573. doi:10.1017/S0022112068002089
- Hutchinson, P. A. and Webster I. T. (1998) Solute Uptake in Aquatic Sediments due to Current-Obstacle Interactions. *J. Environ. Eng.*, 124(5), 419-426, [https://doi.org/10.1061/\(ASCE\)0733-9372\(1998\)124:5\(419\)](https://doi.org/10.1061/(ASCE)0733-9372(1998)124:5(419))
- Jerolmack, D. J., and Mohrig, D. (2005). A unified model for subaqueous bed form dynamics. *Water Resour. Res.*, 41, W12421, <https://doi.org/10.1029/2005WR004329>.
- Jin, X., Cheng, P., Chen, W. and Li, H. (2018) Prediction model of velocity field around circular cylinder over various Reynolds numbers by fusion convolutional neural networks based on pressure on the cylinder. *Phys. Fluids* 30, 047105, doi:10.1063/1.5024595
- King, F. H. (1892) Observations and experiments on the fluctuations in the level and rate of movement of ground-water on the Wisconsin Agricultural Experiment Station Farm, *U. S. Dept. Agr. Weather Bureau, Bull. no. 5*, 75.

- Kocabas, F., Unal, S. and Unal, B. (2008). A neural network approach for prediction of critical submergence of an intake in still water and open channel flow for permeable and impermeable bottom. *International Journal of Computational Fluid Dynamics* 37:1040-1046.
- Lian, Y. P., Dallmann, J., Sonin, B., Roche, K. R., Liu, W. K., Packman, A. I. and Wagner, G. J. (2019) Large eddy simulation of turbulent flow over and through a rough permeable bed. *Computers and Fluids*, 180, 128-138. doi: 10.1016/j.compfluid.2018.12.015
- Lin, J. Y., Cheng, C. T. and Chau, K. W. (2006). Using support vector machines for long-term discharge prediction. *Hydrological Sciences Journal* 51(4): 599-612.
- McGuinness, K. A. and Underwood, A. J. (1986) Habitat structure and the nature of communities on intertidal boulders. *J. Exp. Mar. Biol. Ecol.*, 104, 97-123
- Marion, A., M. Bellinello, I. Guymer, and A. I. Packman (2002), Effect of bedform geometry on the penetration of nonreactive solutes into a streambed, *Water Resour. Res.*, 38(10), 1209, doi:10.1029/2001WR000264.
- Mandelbrot, B. B. (1983). *The fractal geometry of nature*. W. H. Freeman and company, New York
- Martin, R. L., and Jerolmack, D. J. (2013). Origin of hysteresis in bed form response to unsteady flows. *Water Resour. Res.*, 49, 1314–1333. <https://doi.org/10.1002/wrcr.20093>.
- Meinzer, O. E. (1923) Outline of ground-water hydrology with definitions, *U. S. Geol. Surv. Water Supply Paper* 494, 71.
- Meneley, W. A. (1963) The occurrence and movement of groundwater in Alberta, in *Early Contributions to the Groundwater Hydrology of Alberta*, Res. Council Alberta, Can., Bull. 12, 123., Edmonton.
- Mulholland, P. J., Marzolf, E. R., Webster, J. R., Hart, D. R., and Hendricks, S. P. (1997) Evidence that hyporheic zones increase heterotrophic metabolism and phosphorus uptake in forest streams. *Limnology and Oceanography*, 42(3):443–451, ISSN 00243590. doi: 10.4319/lo.1997.42.3.0443.
- Muttil, N. and Chau, K. W. (2006). Neural network and genetic programming for modelling coastal algal blooms. *International Journal of Environment and Pollution* 28(3-4):223-238.
- Muzzammil, M. (2008). Application of neural networks to scour depth prediction at the bridge abutments. *Engineering Applications of Computational Fluid Mechanics* 2(1):30-40.
- Pagliara, S., and Chiavaccini, P. (2006) Flow resistance of rock chutes with protruding boulders. *Journal of Hydraulic Engineering*, 132.6 545-552.
- Palmer, M. A., Hondula, K. L., and Koch, B. J. (2014). Ecological restoration of streams and rivers: shifting strategies and shifting goals. *Annual Review of Ecology, Evolution, and Systematics*, 45, 247-269.

- Nikora, V. and Hicks, D. M. (1997). Scaling relationships for sand wave development in Unidirectional Flow. *J. of Hydraulic Eng.*, 123(12), 1152-1156. doi:/10.1061/(ASCE)0733-9429(1997)123:12(1152)
- Nikora, V. I., Stoesser, T., Cameron, S. M., Stewart, M., Papadopoulos, K., Ouro, P., et al. (2019). Friction factor decomposition for rough-wall flows: theoretical background and application to open-channel flows. *J. Fluid Mech.* 872, 626-664. <https://doi.org/10.1017/jfm.2019.334>
- Norvatov, A. M., and Popov, O. V. (1961) Laws of the formation of minimum stream flow, *Bull. Intern. Assoc. Sci. hydrol.*, vol. 6, no. 1, 20-27, Louvain
- Revelli, R., F. Boano, C. Camporeale, and Ridolfi, L. (2008), Intra-meander hyporheic flow in alluvial rivers, *Water Resour. Res.*, 44, W12428, doi:10.1029/2008WR007081.
- Robert, A. (1988). Statistical properties of sediment bed profiles in alluvial channels. *Mathematical Geology*, 20.3, 205-225.
- Safikhani, H., Khalkhali, A. and Farajpoor, M. (2011). Pareto Based Multi-Objective Optimization of Centrifugal Pumps Using CFD, Neural Networks and Genetic Algorithms. *Engineering Applications of Computational Fluid Mechanics* 5(1):37-48.
- Sawyer, A. H., Cardenas, M. B., and Buttles, J. (2011), Hyporheic exchange due to channel-spanning logs, *Water Resour. Res.*, 47, W08502, doi:10.1029/2010WR010484.
- Sawyer, A. H., and Cardenas, M. B. (2012). Effect of experimental wood addition on hyporheic exchange and thermal dynamics in a losing meadow stream. *Water Resources Research*, 48(10).
- Scalo, C., L. Boegman, and Piomelli, U. (2013) Large-eddy simulation and low-order modeling of sediment-oxygen uptake in a transitional oscillatory flow, *J. Geophys. Res. Oceans*, 118, 1926–1939, doi:10.1002/jgrc.20113.
- Shen, G., Yuan, J. and Phanikumar, M. S. (in-press) Direct numerical simulations of turbulence and hyporheic mixing near sediment-water interfaces. *Journal of Fluid Mechanics*.
- Sherman, T., Roche, K. R., Richter, D. H., Packman, A. I. and Bolster, D. (2019) A Dual Domain stochastic lagrangian model for predicting transport in open channels with hyporheic exchange. *Advances in Water Resources*, 125, 57-67
- Stanford, J. A. and Ward, J. V. (1988) The hyporheic habitat of river ecosystems. *Nature*, 335:8–10.
- Stanford, J. A. and Ward, J. V. (1993) An Ecosystem Perspective of Alluvial Rivers: Connectivity and the Hyporheic Corridor. *Journal of the North American Benthological Society*, 12(1):48–60.

- Stoll, S., Breyer, P., Tonkin, J. D., Früh, D., and Haase, P. (2016). Scale-dependent effects of river habitat quality on benthic invertebrate communities—implications for stream restoration practice. *Science of the Total Environment*, 553, 495-503.
- Stonedahl, S. H., J. W. Harvey, A. Wörman, M. Salehin, and A. I. Packman (2010), A multiscale model for integrating hyporheic exchange from ripples to meanders, *Water Resour. Res.*, 46, W12539, doi:10.1029/2009WR008865.
- Stonedahl, S. H., J. W. Harvey, J. Detty, A. Aubeneau, and A. I. Packman (2012), Physical controls and predictability of stream hyporheic flow evaluated with a multi-scale model, *Water Resour. Res.*, 48, W10513, doi:10.1029/2011WR011582.
- Stonedahl, S. H., J. W. Harvey, and A. I. Packman (2013), Interactions between hyporheic flow produced by streammeanders, bars, and dunes, *Water Resour. Res.*, 9, 5450–5461, doi:10.1002/wrcr.20400.
- Storey, R. G., Howard, K. W., and Williams, D. D. (2003) Factors controlling riffle-scale hyporheic exchange flows and their seasonal changes in a gaining stream: A three-dimensional groundwater flow model. *Water Resources Research*, 39(2):1–17. ISSN 00431397. doi: 10.1029/2002WR001367.
- Thackston, E. L and Schnelle, K. B. (1970) Predicting effects of dead zones on stream mixing. *Journal of Sanitary Engineering Division*, 96(2), 319-331.
- Thibodeaux, L. J., and Boyle, J. D. (1987), Bedform-generated convective transport in bottom sediment, *Nature*, 325, 341–343.
- Tonina, D., and Buffington, J. M. (2007), Hyporheic exchange in gravel bed rivers with pool-riffle morphology: Laboratory experiments and three-dimensional modeling, *Water Resour. Res.*, 43, W01421, doi:10.1029/2005WR004328.
- Tonina, D., and Buffington, J. M. (2009). A three-dimensional model for analyzing the effects of salmon redds on hyporheic exchange and egg pocket habitat. *Canadian Journal of Fisheries and Aquatic Sciences*, 66 (12), 2157–2173. doi: 10.1139/F09-146
- Tóth, J. (1963), A theoretical analysis of groundwater flow in small drainage basins, *J. Geophys. Res.*, 68, 4795–4812, doi:10.1029/JZ068i016p04795
- Trauth, N., Schmidt, C., Maier, U., Vieweg, M., and Fleckenstein, J. H. (2013). Coupled 3-D stream flow and hyporheic flow model under varying stream and ambient groundwater flow conditions in a pool-riffle system. *Water Resources Research*, 49, 5834-5850, doi: 10.1002/wrcr.20442
- Triska, F. J., Kennedy, V. C., Avanzino, R. J., Zellweger, G. W., and Bencala, K. E. (1989). Retention and Transport of Nutrients in a Third-Order Stream in Northwestern California: Hyporheic Processes. *Ecology*, 70 (6), 1893–1905.

- Turcotte, D. (1997). *Fractals and Chaos in Geology and Geophysics*, Cambridge University Press, The Edinburgh Building, Cambridge CB2 8RU, UK
- Valentine, E. M., and Wood, I. R. (1977), Longitudinal dispersion within dead zones, *J. Hydraul. Div. Am. Soc. Civ. Eng.*, 103, 975–1006.
- Venditti, J. G. (2013) Bedforms in sand-bedded rivers, In: *Treatise on Geomorphology* (Ed. J. Shroder, Jr., and E. Wohl), Academic Press, San Diego, California, 137-162.
- Willcox, K. and Peraire, J. (2002) Balanced Model Reduction via the Proper Orthogonal Decomposition. *AIAA Journal* 40(11), 2323-2330, doi: 10.2514/2.1570
- Winter, T. C., Harvey, J. W., Franke, O. L., and Alley, W. M. (1998) *Ground Water and Surface Water: A Single Resource*. U.S. Geological Survey circular. ISBN 0607893397.
- Wisler, Ch. O., and Brater, E. F. *Hydrology*, 2nd ed., 408 pp., John Wiley and Sons, New York, 1959.
- Woessner, W. W. (2000). Stream and fluvial plain ground water interactions: Rescaling hydrogeologic thought. *Ground Water* , 38 (3), 423–429.
- Wohl, E., S. N. Lane, and A. C. Wilcox (2015), The science and practice of river restoration, *Water Resour. Res.*, 51, 5974–5997, doi:10.1002/ 2014WR016874.
- Wondzell, S. M., and Swanson, F. J. (1996), Seasonal and storm dynamics of the hyporheic zone of a 4th-order mountain stream. II. Nitrogen cycling, *J. N. Am. Benthol. Soc.*, 15(1), 20–34.
- Wörman , A., Packman, A. I., Marklund, L., Harvey, J. W., and Stonedahl, S. H. (2006). Exact three-dimensional spectral solution to surface-groundwater interactions with arbitrary surface topography. *Geophys. Res. Lett.*, 33, L07402, <https://doi.org/10.1029/2006GL025747>.
- Wörman, A., A. I. Packman, L. Marklund, J. Harvey, and Stonedahl, S. H. (2007), Fractal topography and subsurface water flows from fluvial bed forms to the continental shield, *Geophys. Res. Lett.*, 34, L07402, doi:10.1029/2007GL029426.
- Wu, K. H., Lin, B. J. and Hung, C. I. (2008). Novel design of centrifugal pump impellers using generated machining method and CFD. *Engineering Applications of Computational Fluid Mechanics* 2(2):195-207
- Yager, E. M., Kirchner, J. W., and Dietrich, W. E. (2007) Calculating bed load transport in steep boulder bed channels. *Water Resour. Res.* 43, W07418, DOI: 10.1029/2006WR005432.

2. RESEARCH QUESTIONS, STATEMENTS AND OBJECTIVES

2.1 How does the fractal dimension of riverbed morphology affect HE processes?

Given that riverbeds are fractals, the relationship between topographic scaling and hyporheic exchange deserves further attention. In this chapter, we considered a broad range of fractal topographies described by their spectral properties to ascertain the relationship between scaling and hyporheic exchange. We addressed the question: How do the fractal properties of riverbeds influence hyporheic exchange? We hypothesize that bed roughness is a primary control of hyporheic exchange in terms of both interfacial flux and bed residence time, and that the influence of the fractal dimension is stronger than the influence of bedform size. We designed numerical experiments on a set of fractal riverbeds having different sizes for the same scaling or different fractal dimensions for the same size. We then quantified the differences in the average interfacial flux (q_{int}) and residence time distribution (RTD) associated with each condition.

2.2 How are the hydrodynamic and hydrostatic drivers of HE related?

The main objective of this chapter is to investigate how coherent flow structures interact with a free surface under different flow conditions and how this affects hyporheic exchange. We this address the following question: How does the SWE change as the Froude number increases to near critical conditions and how much does it affect hyporheic exchange? We use computational fluid dynamics to simulate the two-phase (air-water) turbulent flow under various Froude number. The volume of fluid method is used to model the surface water wave and hydraulic jumps. A groundwater flow model is then sequentially coupled with the free-surface water flow model. We then compared the results of the free surface simulations to cases with a fixed SWE.

2.3 How do the spacing and embeddedness of boulders control HE?

In this chapter, we investigate how boulder spacing and embeddedness affect the near bed hydrodynamics and in turn the hyporheic flux and residence time. We use Computational Fluid Dynamics (CFD) to simulate the stream flow and a groundwater model is then sequentially coupled with the surface flow model. Hyporheic flux is computed as the sum of the inward Darcy fluxes at the sediment water interface, and hyporheic residence time distributions are calculated

from the hyporheic flow-field. Our results show that as boulders are more embedded, flowpaths are shorter and so are the associated travel times. Spacing increases hyporheic flux without affecting the subsurface domain, thus systematically decreasing residence times. Fluxes decreased with increasing embeddedness, but less so as clusters were tighter. Together, our results suggest that there is an optimal configuration that enhances hyporheic flux when boulders are not embedded and sufficiently far away. Our findings could help better manage and conserve riverine ecosystems by optimizing hyporheic processes during restoration projects.

2.4 Can we predict the pressure across the bed using point velocities?

ANNs have shown great potential to tackle high-dimensional nonlinear problems in fluid dynamics. This chapter focuses on developing a prediction model using ANNs based on the numerical simulation results from the previous chapter on boulder-driven hyporheic exchange. We firstly extract flow velocities at various locations and corresponding pressure values at the sediment bed. Then we train neural networks with velocities as an input and bed pressure as an output variable with 70% of the extracted data. Lastly we test the neural network model with the test dataset whether it accurately models the nonlinear relationship between velocity and pressure.

3. THEORETICAL BACKGROUND

3.1 Navier-Stokes equations for incompressible, Newtonian fluid

The governing principles of the fluid flow are the conservation of mass, momentum, and energy (Kundu et al., 2012). In this chapter, the Navier-Stokes (NS) equations are presented which associates mass and momentum conservation laws. We model river flow with NS equations assuming the water is incompressible and Newtonian.

3.1.1 Conservation of mass

The derivation of conservation of mass in a fluid flow are based on the assumption that the mass collected from neighboring fluid particles is constant. Consider the mass flow through a small control volume. Conservation of mass for the control volume in a flowing fluid is:

$$\frac{\partial}{\partial t} \int_{V(t)} \rho(\mathbf{x}, t) dV = 0 \quad (3.1)$$

where ρ is the fluid density, \mathbf{x} is the location vector, t is time and $V(t)$ is the total volume at time t . By Reynolds transport theorem,

$$\int_{V(t)} \frac{\partial \rho(\mathbf{x}, t)}{\partial t} dV + \int_{A(t)} \rho(\mathbf{x}, t) \mathbf{u}(\mathbf{x}, t) \cdot \mathbf{n} dA = 0 \quad (3.2)$$

By applying Gauss' divergence theorem to Eq. (3.2) for the surface integration,

$$\int_{V(t)} \left\{ \frac{\partial \rho(\mathbf{x}, t)}{\partial t} + \nabla \cdot (\rho(\mathbf{x}, t) \mathbf{u}(\mathbf{x}, t)) \right\} dV = 0 \quad (3.3)$$

Since Eq. (3.3) requires the integrand to be zero:

$$\frac{\partial \rho(\mathbf{x}, t)}{\partial t} + \nabla \cdot (\rho(\mathbf{x}, t) \mathbf{u}(\mathbf{x}, t)) = 0 \quad (3.4)$$

This equation is called the continuity equation. For the incompressible case, the density for the fluid is constant and thus we can simplify the continuity equation to

$$\nabla \cdot \mathbf{u} = 0 \quad (3.5)$$

Volume of Fluid (VoF) Method

The volume of fluid (VoF) method is to simulate free boundary configuration (Hirt and Nichols, 1981). We use VoF in the cases where the water surface profile changes in response to

the channel geometry when the Froude number is sufficiently large. The density ρ and viscosity μ in the domain are given by

$$\rho = F\rho_1 + (1 - F)\rho_2 \quad (3.6)$$

$$\mu = F\mu_1 + (1 - F)\mu_2 \quad (3.7)$$

where F is the volume fraction function for the two fluids (air and water) defined by

$$F = \begin{cases} 0 & \text{if volume occupied by air} \\ 1 & \text{if volume occupied by water} \end{cases} \quad (3.8)$$

Volume fraction F is transported by the fluid velocity field. The equation for the volume fraction scalar F is a conservation law:

$$\frac{\partial F}{\partial t} + \nabla \cdot (\mathbf{u}F) + \nabla \cdot (\mathbf{u}_R F(1 - F)) = 0 \quad (3.9)$$

where \mathbf{u} is the velocity of air-water mixture and \mathbf{u}_R is the relative velocity between air and water phases to compress the interface.

3.1.2 Conservation of momentum

For the derivation of the conserved momentum equation, we use Newton's second law which is the fundamental law governing fluid momentum:

$$\frac{\partial}{\partial t} \int_{V(t)} \rho(\mathbf{x}, t) \mathbf{u}(\mathbf{x}, t) dV = \int_{V(t)} \rho(\mathbf{x}, t) \mathbf{g} dV + \int_{A(t)} \mathbf{f}(\mathbf{n}, \mathbf{x}, t) dA \quad (3.10)$$

where $\rho\mathbf{u}$ is the momentum per unit volume, \mathbf{g} is the body force per unit mass, \mathbf{f} is the surface force per unit area acting on $A(t)$, and \mathbf{n} is the normal vector of $A(t)$. By applying Reynolds transport theorem,

$$\begin{aligned} \int_{V(t)} \frac{\partial}{\partial t} (\rho(\mathbf{x}, t) \mathbf{u}(\mathbf{x}, t)) dV + \int_{A(t)} \rho(\mathbf{x}, t) \mathbf{u}(\mathbf{x}, t) (\mathbf{u}(\mathbf{x}, t) \cdot \mathbf{n}) dA \\ = \int_{V(t)} \rho(\mathbf{x}, t) \mathbf{g} dV + \int_{A(t)} \mathbf{f}(\mathbf{n}, \mathbf{x}, t) dA \end{aligned} \quad (3.11)$$

Using Gauss' theorem, we convert the surface integrals to volume integrals:

$$\begin{aligned} \int_{A(t)} \rho(\mathbf{x}, t) \mathbf{u}(\mathbf{x}, t) (\mathbf{u}(\mathbf{x}, t) \cdot \mathbf{n}) dA \\ = \int_{V(t)} \nabla \cdot (\rho(\mathbf{x}, t) \mathbf{u}(\mathbf{x}, t) \mathbf{u}(\mathbf{x}, t)) dV \end{aligned} \quad (3.12a)$$

$$\int_{A(t)} \mathbf{f}(\mathbf{n}, \mathbf{x}, t) dA = \int_{V(t)} \nabla \cdot \boldsymbol{\tau} dV \quad (3.12b)$$

where $\boldsymbol{\tau}$ is stress tensor. Thus, Eq. (3.11) becomes

$$\frac{\partial \rho \mathbf{u}}{\partial t} + \nabla \cdot (\rho \mathbf{u} \mathbf{u}) - \nabla \cdot \boldsymbol{\tau} = -\nabla p + \rho \mathbf{g} \quad (3.13)$$

Assuming Newtonian fluid,

$$\boldsymbol{\tau} = 2\mu \mathbf{S} - \frac{2}{3}\mu(\nabla \cdot \mathbf{u})\mathbf{I} \quad (3.14)$$

where \mathbf{S} is the strain rate tensor which is defined by $\mathbf{S} = [\nabla \mathbf{u} + (\nabla \mathbf{u})^T]/2$.

For incompressible flow, Equation (3.13) is further simplified as

$$\frac{\partial \rho \mathbf{u}}{\partial t} + \nabla \cdot (\rho \mathbf{u} \mathbf{u}) - \nabla \cdot (2\mu \mathbf{S}) = -\nabla p + \rho \mathbf{g} \quad (3.15)$$

since $\nabla \cdot \mathbf{u} = 0$.

3.2 Reynolds-averaged Navier-stokes (RANS) equations

Turbulent flows are associated with unpredictable fluctuations, and they have not been fully understood by deterministic or statistical analysis. In this chapter, we focus on the Reynolds-Averaging approach which was introduced by Osborne Reynolds. The dependent-field quantities can be separated into two components representing the mean $\bar{\phi}$ and its fluctuation ϕ' that is oscillating around the mean value:

$$\phi(\mathbf{x}, t) = \bar{\phi}(\mathbf{x}, t) + \phi'(\mathbf{x}, t) \quad (3.16)$$

where

$$\bar{\phi}(\mathbf{x}, t) = \lim_{T \rightarrow \infty} \frac{1}{T} \int_t^{t+T} \phi(\mathbf{x}, t) dt \quad (3.17)$$

$$\overline{\phi'}(\mathbf{x}, t) = 0 \quad (3.18)$$

The time-averaged incompressible mass conservation equation can be obtained by substituting $\mathbf{u} = \bar{\mathbf{u}} + \mathbf{u}'$ in Eq. (3.4),

$$\nabla \cdot \bar{\mathbf{u}} = 0 \quad (3.19)$$

The time-averaged incompressible momentum conservation equation is then

$$\frac{\partial \rho \bar{\mathbf{u}}}{\partial t} + \nabla \cdot (\rho \bar{\mathbf{u}} \bar{\mathbf{u}}) - \nabla \cdot (2\mu \mathbf{S}) = -\nabla p + \rho \mathbf{g} - \rho \nabla \cdot (\overline{\mathbf{u}' \mathbf{u}'}) \quad (3.20)$$

These equations are known as Reynolds-Averaged-Navier-Stokes equations (RANS).

3.2.1 Eddy viscosity approximation

Joseph Boussinesq related the Reynold-Stresses ($\overline{\sigma_t}$), which is $-\rho \overline{\mathbf{u}' \mathbf{u}'}$, to the mean values of the velocities and the kinetic energy of the turbulence k as:

$$\bar{\sigma}_t = 2\mu_t \bar{\mathbf{S}} - \frac{2}{3}\mu_t(\nabla \cdot \bar{\mathbf{u}})\mathbf{I} - \frac{2}{3}\rho \mathbf{I} k \quad (3.21)$$

where k is defined as

$$k = \frac{1}{2} \overline{\mathbf{u}' \cdot \mathbf{u}'} \quad (3.22)$$

The turbulence kinetic energy and turbulence energy dissipation rate are then computed by solving the following differential equations:

$$\mu_t = C_\mu \frac{k}{\epsilon} \quad (3.23)$$

$$\frac{\partial(\rho k)}{\partial x_j} + \nabla \cdot (\rho \mathbf{u} k) = \nabla \cdot \left[\frac{\mu_t}{\sigma_k} \nabla k \right] + 2\mu_t |\nabla \mathbf{u}|^2 - \rho \epsilon \quad (3.24)$$

$$\frac{\partial(\rho \epsilon)}{\partial x_j} + \nabla \cdot (\rho \mathbf{u} \epsilon) = \nabla \cdot \left[\frac{\mu_t}{\sigma_\epsilon} \nabla \epsilon \right] + 2C_1 \mu_t |\nabla \mathbf{u}|^2 \frac{\epsilon}{k} - C_2 \rho \frac{\epsilon^2}{k} \quad (3.25)$$

where μ_t is the eddy viscosity, k is turbulence kinetic energy, ϵ is turbulence energy dissipation rate. The constants $C_\mu, C_1, C_2, \sigma_k, \sigma_\epsilon$ take the values of 0.09, 1.44, 1.92, 1.9, 1.3 respectively.

3.3 Porous flow modeling

The potential and flow field for groundwater flow are modeled by Darcy's law:

$$-\nabla \cdot \left[\frac{K}{\mu} \nabla h - \rho \mathbf{g} \right] = 0 \quad (3.26)$$

where K is intrinsic permeability and h is potential head. We set $\tilde{h} = h - \rho \mathbf{g} \mathbf{z}$ to render boundary condition simple, e.g. $\nabla \tilde{h} \cdot \vec{n} = 0$ at the wall where \vec{n} is the normal vector at the boundary. Then Eq. (3.26) becomes:

$$-\nabla \cdot \left[\frac{K}{\mu} \nabla \tilde{h} \right] = 0 \quad (3.27)$$

The Darcy flux, given constant intrinsic permeability, can be sequentially computed by

$$\mathbf{q}_s = -\frac{K}{\mu} [\nabla \tilde{h}] \quad (3.28)$$

The interfacial flux is then calculated by

$$q_{int}(x) = \begin{cases} \mathbf{q}_s \cdot \mathbf{n} & \text{if } \mathbf{q}_s \cdot \mathbf{n} > 0 \\ 0 & \text{if } \mathbf{q}_s \cdot \mathbf{n} \leq 0 \end{cases} \quad (3.29)$$

where \mathbf{n} is the unit vector normal to the bed surface into the bed.

3.4 Solute transport modeling

The advection-diffusion-dispersion equation is

$$\frac{\partial c}{\partial t} = -\nabla(\mathbf{U}c) + \nabla(\mathbf{D}\nabla c) \quad (3.30)$$

where $c = c(\mathbf{x}, t)$ is concentration, $\mathbf{U} = \mathbf{U}(\mathbf{x}, t)$ is a velocity field, $\mathbf{D}(\mathbf{x}, t)$ is dispersion coefficient at location \mathbf{x} and time t . For the dispersion coefficient, we assume

$$\mathbf{D} = (D_m + \alpha_v |\mathbf{U}(\mathbf{x}(t))|) \mathbf{I} + \frac{\alpha_L - \alpha_v}{|\mathbf{U}(\mathbf{x}(t))|} \mathbf{U} \otimes \mathbf{U} \quad (3.31)$$

where D_m is the molecular diffusion coefficient, α_L and α_v are longitudinal and vertical dispersivities, \mathbf{U} is the pore velocity vector and \mathbf{I} is the identity matrix (Bear, 1961). The longitudinal dispersivity is assumed to be equal to $\alpha_L = 0.5$ m and the transverse dispersivity is approximated by $\alpha_T = 0.1\alpha_L$ (Cardenas et al., 2008; Moltyaner and Killey, 1988).

3.4.1 Fokker-Planck-Kolmogorov Equation (FPKE)

We can rewrite the advection-diffusion-dispersion equation as

$$\frac{\partial c}{\partial t} = -\nabla[(\mathbf{U} + \nabla\mathbf{D}) \cdot c] + \nabla^2(\mathbf{D}c) \quad (3.32)$$

for $\nabla^2(\mathbf{D}c) = \nabla(\mathbf{D}\nabla c + c\nabla\mathbf{D})$ Particle tracking methods solve the Fokker-Planck-Kolmogorov Equation (FPKE):

$$\frac{\partial P}{\partial t} = -\nabla(\mathbf{A}P) + \frac{1}{2} \nabla^2(\mathbf{B}P) \quad (3.33)$$

where $P = P(\mathbf{x}, t)$ is the probability density for a particle to be at location \mathbf{x} at time t . $\mathbf{A}(\mathbf{x})$ and $\mathbf{B}(\mathbf{x})$ can be interpreted as the mean velocity and the statistical dispersion respectively. By equating (18) and (19), we get $\mathbf{A}(\mathbf{x}) \equiv \mathbf{U} + \partial\mathbf{D}/\partial\mathbf{x}$ and $\mathbf{B}(\mathbf{x}) \equiv \mathbf{D}$. This yields an algorithm for the new location of a particle after time Δt :

$$\mathbf{x}(t + \Delta t) = \mathbf{x}(t) + [\mathbf{U}(\mathbf{x}(t)) + \nabla\mathbf{D}(\mathbf{x}(t))] \cdot \Delta t + (2\mathbf{D}(\mathbf{x}(t)) \cdot \Delta t)^{1/2} \cdot \boldsymbol{\xi} \quad (3.34)$$

where \mathbf{x} is the location of particle, $\boldsymbol{\xi}$ is a vector of random numbers drawn from a standard normal distribution (Delay et al., 2005).

3.4.2 Residence time

Assume the initial concentration value, c_0 , is uniformly distributed over the upper boundary of groundwater domain, which is the sediment-water interface, and the solute is transported by

advection-dispersion equation as given in Eq. (3.30). The solute mass in the bed is computed by integrating concentration inside the bed,

$$R(t) = \int_{Vol_{bed}} c(\mathbf{x}, t) dV \quad (3.35)$$

The average residence time function, $\bar{R}(\tau)$, which denotes the fraction of solute which entered the bed in a short time near $t = 0$ and remains in the bed at time τ is

$$\bar{R}(\tau) = \frac{\int_L q_{int} R(x_0, \tau) ds}{\int_L q_{int} ds} \quad (3.36)$$

where $R(x_0, \tau)$ denotes the fraction of solute particles which entered the bed at an arbitrary point at SWI, x_0 , and remains in the bed after an elapsed time τ , L is the length of sediment-water interface. The residence time distribution is the time derivative of $\bar{R}(\tau)$.

3.5 References

- Bear, J. (1961). On the tensor form of dispersion in porous media, J. Geophys. Res., 66(4), 1185–1197. <https://doi.org/10.1029/JZ066i004p01185>.
- Cardenas, M. B., Wilson, J. L., and Haggerty, R. (2008). Residence time of bedform-driven hyporheic exchange. Advances in Water Resources, 31(10), 1382-1386. <https://doi.org/10.1016/j.advwatres>
- Delay, F., Ackerer, P. and Danquigny, C. (2005) Simulating solute transport in porous or fractured formations using random walk particle tracking: A Review. Vadose Zone Journal, 4, 360-379
- Hirt, C. W., & Nichols, B. D. (1981). Volume of Fluid (VOF) Method for the Dynamics of Free Boundaries. Journal of computational physics, 39, 201–225.
- Kundu, P. K., Cohen, I. M. and Dowling, D. R. (5th ed.) (2012) *Fluid mechanics*. Waltham, MA 02451, USA. Elsevier Inc.
- Moltyaner, G. L., and Killey, R. W. D. (1988). Twin Lake Tracer Tests: Transverse dispersion. Water Resour. Res., 24(10), 1628–1637. <https://doi.org/10.1029/WR024i010p01628>.

4. THE SENSITIVITY OF HYPORHEIC EXCHANGE TO FRACTAL PROPERTIES OF RIVERBEDS

Hyporheic exchange in riverbeds is driven by current-bed topography interactions. Because riverbeds exhibit roughness across scales, from individual grains to bedforms and bars, they can exhibit fractal patterns. This study analyzed the influence of fractal properties of riverbeds on hyporheic exchange. A set of synthetic fractal riverbeds with different scaling statistics was used as inputs to sequentially-coupled numerical simulations of turbulent channel flow and hyporheic flow (Figure 4.1). In the analysis, the maximum power spectrum (dune size) and the fractal dimension (topographic complexity) were considered as independent variables and we then investigated how interfacial fluxes and hyporheic travel times are functionally related to these variables. As the maximum power spectrum increases (i.e., dune height to flow depth ratio), the average interfacial flux increases logarithmically whereas it increases exponentially with an increase in fractal dimension. Hyporheic exchange is more sensitive to additional roughness (larger fractal dimensions) than to bedform size (larger maximum power). Our results imply that fractal properties of riverbeds are crucial to predicting hyporheic exchange. The predictive relationships we propose could be integrated with reduced complexity, large scale models. They can also be used to design artificial topographies that target hyporheic ecosystem services.

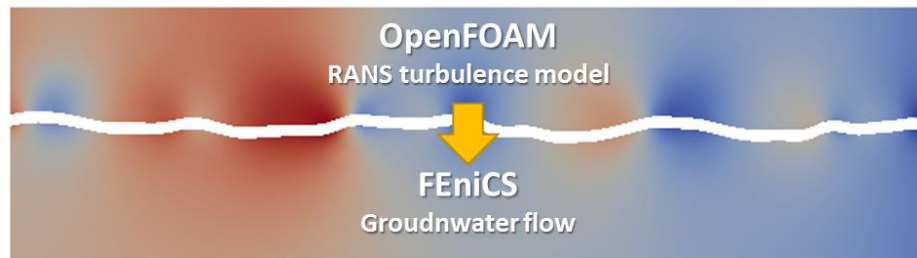


Figure 4.1. Illustration of the sequentially coupled surface-subsurface model framework. The channel flow field was calculated using OpenFOAM. The interfacial pressure fields from OpenFOAM simulations were used as the upper boundary to solve the groundwater flow field using FEniCS.

4.1 Fractal riverbed profiles

The self-similarity of fractals is indicated by the power-law relationship between their power spectral density (PSD) and wave number (or spatial frequency), i.e., $|X(q)|^2 = Cq^{-\beta}$ where $X(q)$ is the Fourier transform of surface elevation at wave number q and C and β are positive constants (Malinverno and Gilbert, 1989). The power-law dependence of the PSD on wave number is indicated by β and is often expressed as a Hurst exponent (H): $\beta = 2H + 1$. The fractal dimension (D) of the topography is also related to the spectral slope by: $\beta = 5 - 2D$ so that the smaller D is, the higher β is and the signal with small wavelength (high frequency) has less amplitude (Turcotte, 1997). These small D cases correspond to smooth bedforms with high spatial correlation in their elevation profile. Conversely, high fractal dimensions (and lower β) correspond to rougher (noisier) surfaces, with less short-range correlation in elevation. $\beta = 0$ corresponds to random white noise profiles.



Figure 4.2. Types of low Froude number bedforms that are typically present as channel flow velocity increases: (a) typical ripple pattern ($0.1 < Fr < 0.3$), (b) compound dunes ($0.3 < Fr < 0.6$), and (c) dunes ($0.6 < Fr < 0.84$). The sketch of bedforms were adapted from Simons & Richardson (1966). The upper and lower limit of Froude number for each configuration is roughly estimated by the depth/velocity diagrams suggested by Southard and Boguchwal (1990) illustrating the fields of bedforms stability for grain size = 0.4 – 0.6 mm.

Surface flow velocity controls the shape of natural bedforms and thus also their fractal dimension in nature. Plane beds are followed by a sequence across increasing Froude number: plane bed \rightarrow ripples \rightarrow ripples on dunes (compound dunes) \rightarrow dunes \rightarrow transition or washed-out dunes \rightarrow plane bed \rightarrow antidune standing waves \rightarrow antidune breaking waves \rightarrow chutes and pools (Simons and Richardson, 1966; Tonina and Buffington, 2009). If we consider the elevation profile as a signal, compound dunes (Figure 4.2b) have more energy in the small wavelength (high frequency) than dunes (Figure 4.2c); the amplitude of the signal with small wavelength is thus smaller in the dunes, resulting in larger spectral slopes β (smaller D) and smoother, more spatially

correlated profiles. In the next two subsections, we first describe the statistical properties of two observed riverbeds (4.1.1) to inform the parameter sets we selected for the computer-generated riverbeds (4.1.2).

4.1.1 Previous Observations of Riverbeds and their Fractal Characterization

The experimental design in this study is based on and inspired by observations of two contrasting sand riverbeds measured by Aubeneau et al. (2015) in a large flume (Figure 4.3a); one had small and irregular dunes while the other had larger and smoother bedforms. These experiments are referred to as M1 and M2 hereafter. Bedforms were generated by a steady water discharge, 40 L/s (velocity ~ 0.2 m/s) and 80 L/s (velocity ~ 0.4 m/s) for M1 and M2, respectively. In M1, the average height and length of bedforms were 6 cm and 66 cm whereas they were 20 cm and 90 cm, respectively, in M2. To describe these riverbeds, metrics that characterize fractals are used, and these are defined below.

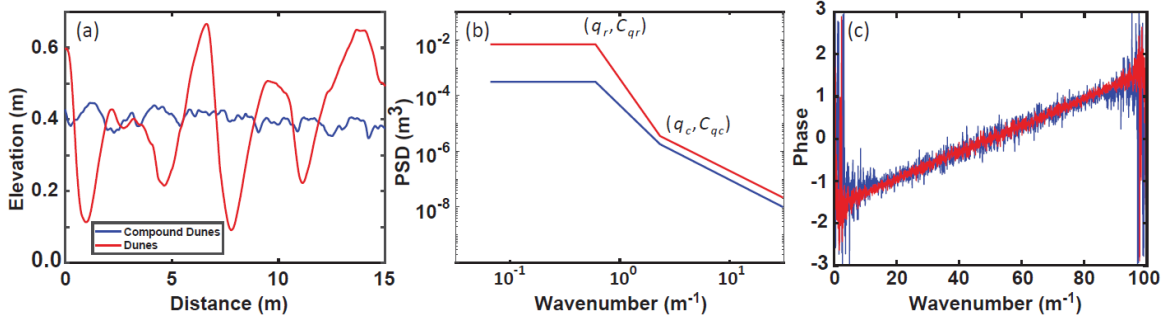


Figure 4.3. Measured bedforms and their characteristics: (a) Cross section of two sand beds generated in a flume and (b) Schematic power spectra of the elevation profiles, showing the location of the scaling regime between the wavelengths q_r and q_c , which corresponds to the spectral density C_{qr} and C_{qc} (original figure in Aubeneau et al., 2015). Note the steeper slope for the smoother dunes and the higher spectral density for the larger dunes compared to the smaller compound dunes. (c) Behavior of the phase for increasing wavelengths. Note the linear increase that we use to generate realistic artificial profiles.

A Discrete Fourier Transform (DFT) yields the Power Spectral Density (PSD) (Figure 4.3b)

$$X(q) = \frac{1}{N} \sum_{n=0}^{N-1} e^{-j2\pi qn} x(n), \quad (4.1)$$

where $x(n)$ is the surface profile measurement (m) which consists of N values. We identify the scaling regime between q_r and q_c (m⁻¹) with corresponding spectral density C_{qr} and C_{qc} (m³). The

slope of the PSD between q_r and q_c is β . In addition, we also introduce the mean-square roughness, δ^2 (m²), which is defined by the mean square of the elevation:

$$\delta^2 = \frac{1}{N} \sum_{n=0}^{N-1} x^2(n), \quad (4.2)$$

This value is also known as a power signal, which is an averaged energy signal. δ^2 is equivalent to the area under the PSD (Eq. (4.3)) by Parseval's theorem (Eq. (4.4)):

$$\delta^2 = \frac{1}{N^2} \sum_{q=0}^{N-1} |X(q)|^2 = \frac{1}{L_x} \sum_{q=0}^{N-1} P(q) \quad (4.3)$$

$$N \sum_{n=0}^{N-1} x^2(n) = \sum_{k=0}^{N-1} |X(q)|^2 \quad (4.4)$$

where PSD is defined as $P(q) = |X(q)|^2 (L_x/N^2)$, $X(q)$ is the Fourier transform of $x(n)$, L_x is the length of the surface profile (m).

The wavenumber and power density (m³) varied from 0.5 to 5 and from 1×10^{-7} to 6.5×10^{-3} for the M1 and M2 riverbeds. $\beta=2$, $D=1.5$, $H=0.5$, and $\delta^2=2.3 \times 10^{-2}$ m² for M1, and $\beta=3$, $D=1$, $H=1$ and $\delta^2=4.5 \times 10^{-4}$ m² for M2. C_q is larger for M2 (large features) than for M1 (small features), reflecting the difference in dune elevation. D is also smaller for M2, indicating the change from compound dunes (M1) to dunes-dominated riverbed (M2).

As D is larger (which also means there is a shallower slope in the PSD), the amplitude of fluctuations with small wavelengths has a higher influence on the spectra and vice versa. Smaller D corresponds to the disappearance of small wavelengths resulting in a smoother, more correlated topography associated with steeper power spectral slopes. In summary, C_q reflects the magnitude of the bedforms whereas D captures their roughness, or complexity

4.1.2 Generation of Synthetic Riverbeds based on Observations

Because C_q and D are the main characteristics of the bed topography PSD, we generated two sets of PSD: one with different maximum PSDs (referred to as the C_q cases hereafter) but constant D ; the second with different D (referred to as the D cases hereafter) but constant C_q . We built both sets of cases using q_r and q_c values from M1. The tailing in PSD after q_c is ignored so that hyporheic exchange only depends on C_q or D . C_q is varied from the minimum to the maximum observed in M1 and M2, while D values range from 0 to 2. The middle parameter value is used for C_q and D when they are held constant ($C_q = 10^{-3}$ m³ when D is varied and $D=1$ when C_q changes;

see Figure 4.4). The PSD method is useful in that it can create multiscale bedforms and the fractal dimension of the dune fields can be easily controlled. A total of twelve cases were considered, six in each suite. In increasing order, the six C_q cases had values of 10^{-4} (for case C_q1), $10^{-3.6}$ (C_q2), $10^{-3.2}$ (C_q3), $10^{-2.8}$ (C_q4), $10^{-2.4}$ (C_q5), and 10^{-2} (C_q6); the D cases had D values of 0 (for case $D1$), 0.4 ($D2$), 0.8 ($D3$), 1.2 ($D4$), 1.6 ($D5$), and 2.0 ($D6$). A relative trend and relationship between phase and frequency found in the observed bed topography was also implemented when creating artificial riverbeds. In order to replicate the phase behavior, we assigned random values varying from $-\pi$ to π before q_r and $-\pi/4$ to $\pi/4$ after q_r with an increasing linear trend (see Figures 4.3c and 4.4e). In addition, the same phase values were used for all riverbeds within the range of wavenumber = $0 \sim q_r \text{ m}^{-1}$.

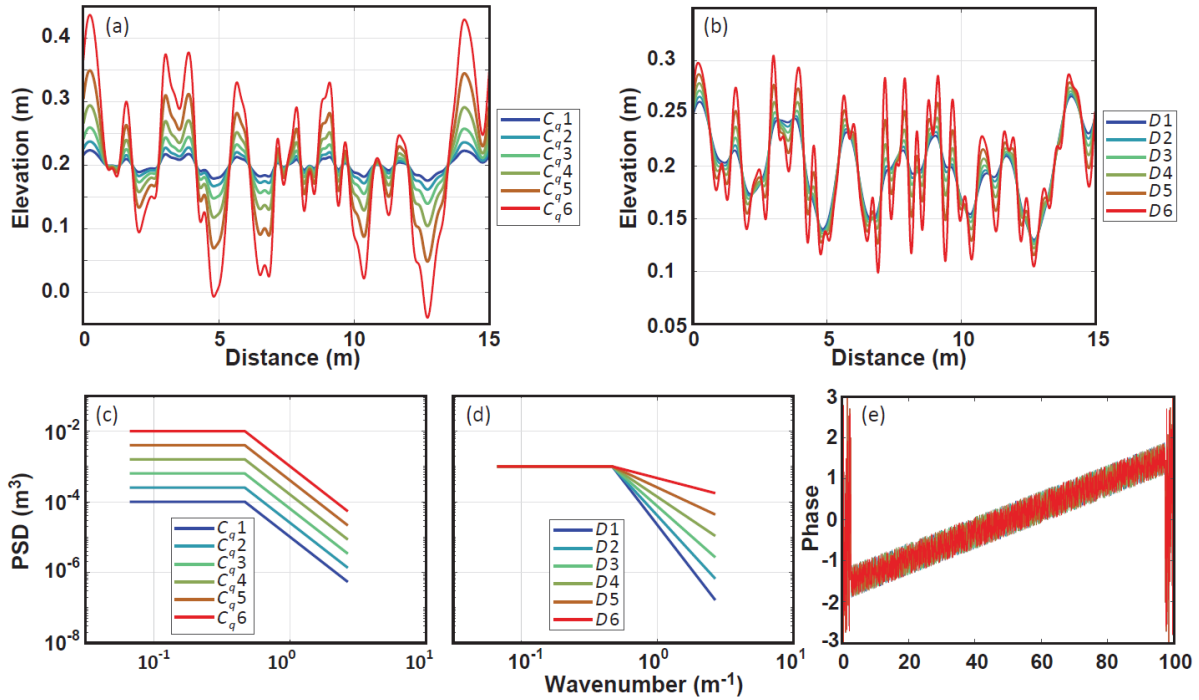


Figure 4.4. Bed profile of (a) Case C_q (b) Case D and power spectral density of (c) Case C_q (d) Case D (e) Phases for both C_q and D cases. The C_q cases show the effect of maximum power spectral density or the amplitude of bedform whereas the D cases show the impact of fractal dimension of riverbeds. The phase of the signal is artificially generated to have a large variance up to the roll-off frequency and then increase linearly afterwards.

The two sets of six different power spectra described above were inverse Fourier transformed to a 2-dimensional spatial morphology (longitudinal direction and vertical direction). The discrete inverse Fourier transform $x(n)$ is

$$x(n) = \frac{1}{N} \sum_{q=0}^{N-1} e^{j\frac{2\pi}{N}qn} X(q), \quad n = 0, \dots, N-1 \quad (4.5)$$

The total length of the simulated domain is 15 m, with $N=1500$ discrete points. Figure 4.4 illustrates the morphology of the two sets of computer-generated riverbeds. As mentioned in Section 4.1.1, C_q reflects the size or the elevation of dunes while D indicates their roughness. These characteristics are clearly apparent in Figure 4.4.

4.2 Simulation conditions

The two-dimensional steady-state Reynolds-average Navier-Stokes (RANS) model is used to simulate the surface flow to obtain the pressure distribution imposed upon the sediment-water interface (SWI). We used OpenFOAM 5.0 to solve the CFD model introduced in this section. In the natural fluvial system, surface water controls the size and shape of bedforms. However, in order to demonstrate the effects of roughness on hyporheic exchange, we used fixed beds for our simulations, and assumed constant water depth and velocity of 1 m and 0.3 m/s respectively. We note that the influence of water depth is not considered. In addition, the flow velocity is under the threshold shear for bedload for a coarse sand. A uniform velocity profile was used at the inlet and the simulation was run until reaching steady-state to isolate the effects of dune morphology (statistical properties). To minimize boundary effects, the upstream-most 3 meters were discarded from the results. A no-slip condition was applied at the sediment-water interface. We adopted a Low-Reynolds number treatment for the viscous boundary layer instead of using wall functions at the sediment bed. The near-wall grid points are positioned such that the dimensionless wall distance is less than 1 ($y^+ < 1$) everywhere which will give a finer mesh than the wall function approach (Versteeg and Malalasekera, 2007). The mesh is composed of hexahedral cells and the total number of cells is approximately 50,000.

The two-dimensional groundwater potential and flow field are modeled by the finite element method. The boundary value problem and the finite element discretization is constructed and solved by FEniCS (Logg et al., 2012). The unstructured triangular mesh is generated automatically by the built-in mesh generation function and the number of elements is about 10,000 for the 15 m

(streamwise) \times 4 m (vertical) domain. The second order Lagrange element is adopted for both trial and test function. The hydraulic conductivity is assumed isotropic and set at 1.5×10^{-3} m/s, typical of coarse to very coarse sand

We used particle tracking to approximate the transported solute mass in the subsurface flow field (Kitanidis, 1994), which in turn yields the time spent by the particles in the bed. The molecular diffusion coefficient is set to 5×10^{-11} m²/s, the longitudinal dispersivity is assumed to be equal to $\alpha_L = 0.5$ m and the transverse dispersivity is approximated by $\alpha_T = 0.1\alpha_L$ (Cardenas et al., 2008; Moltyaner and Killey, 1988). The maximum spatial step is set to 0.001 m (Stonedahl et al., 2010) and the time step (Δt) is calculated for a Courant number of 0.5: $\Delta t = Co \cdot D_{\text{step}}/|\mathbf{q}_p|_{\text{max}}$ where $|\mathbf{q}_p|_{\text{max}}$ is the magnitude of maximum velocity of particles, D_{step} is the distance for one particle to move in one step, 0.001 m.

4.3 Results and Discussion

4.3.1 Modeled pressure and flow fields

Figure 4.5 shows the channel flow field and the subsurface hydraulic head. In the C_q suite of cases, the surface flow is essentially uniform for small amplitudes (Figure 4.5a and 4.5b). As bedforms become more prominent (as in C_q5 and C_q6), eddies appear and develop behind the larger features where the flow separates (Figure 4.5e and 4.5f). Flow separation seemed to initiate when the lee side slope was 0.2 or greater, and eddies were more prominent where the distance between two neighboring peaks was large. We observed similar patterns in the D suite of cases, but because the bedforms were smaller, we did not see large, well developed eddies. In the subsurface, local head gradients between the stoss and lee sides drive hyporheic flow. In the C_q cases, as bedform size grew, flow cells represented by the white equipotential lines also grew and assimilated some of the smaller features. Conversely, for the D cases, more and more local cells appear as the fractal dimension increases, reflecting the additional transport scales introduced by the added scaling.

The pressure at the sediment-water interface is closely related to the morphology of the riverbeds. Since the surface flow is consistent across simulations (0.3 m/s, 1 m water depth), the head at the bed is controlled by the changes in bed elevation. The side view of riverbed elevation and pressure distribution for different C_q and D are shown in Figure 4.6. The magnitude of the pressure gradient resulting from the elevation difference between peak and trough is largest for the

C_q6 case, as shown in Figure 4.6b. Figure 4.6a illustrates that the local bedform peak corresponds to a local minimum pressure and that the local bedform trough to a local maximum pressure.

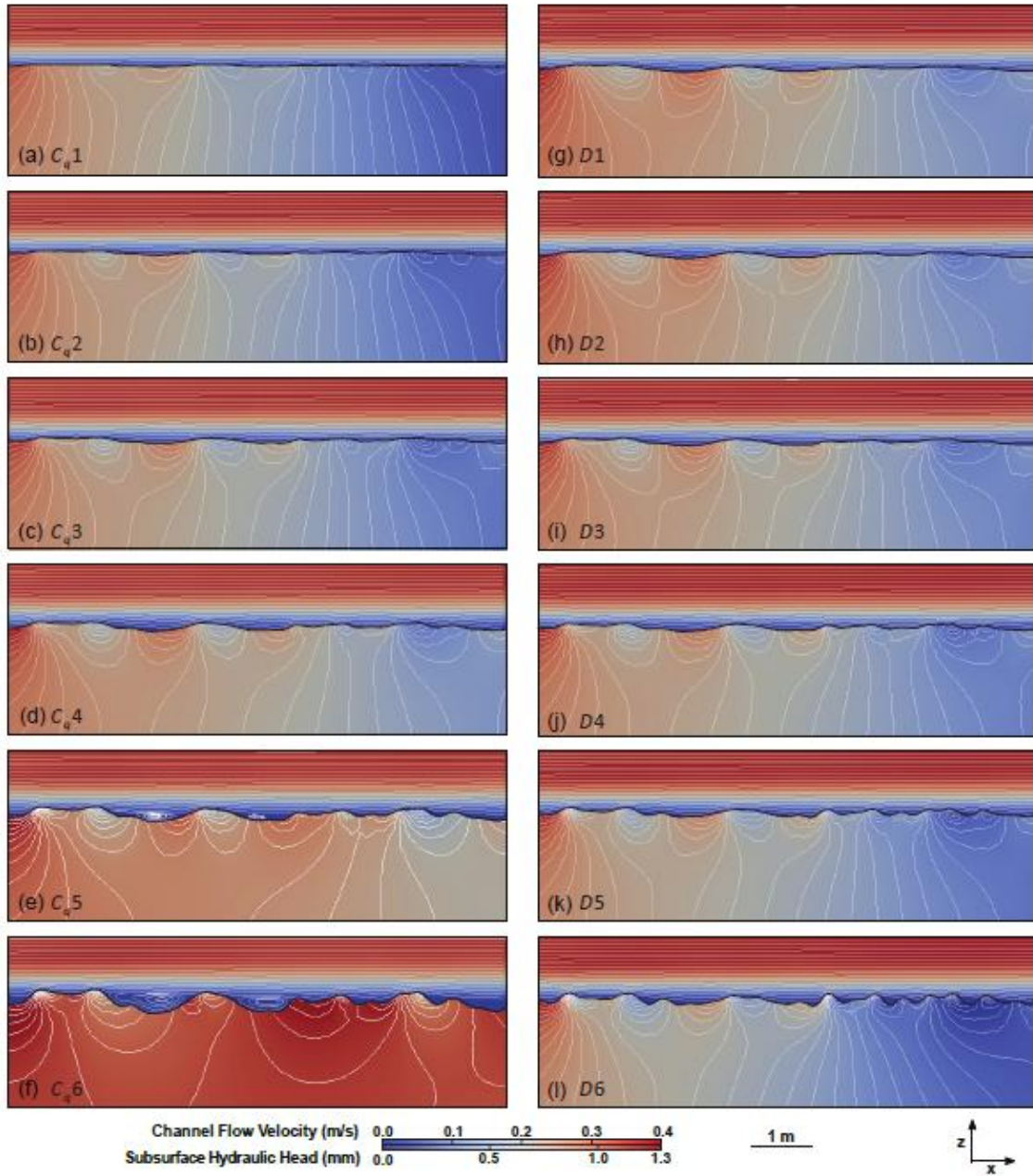


Figure 4.5 Channel flow velocity and subsurface hydraulic head for all cases: (a) ~ (f) for $C_q1 \sim C_q6$, (g) ~ (l) for $D1 \sim D6$. The surface flow is consistent throughout simulations (0.3 m/s, 1 m water depth). The flow separation starts revealing in (d) C_q4 , and becoming prominent in (e) C_q5 and (f) C_q6 . The occurrence of flow separation depends on the size of bedform. In the C_q cases, the hydraulic head equipotential lines under a local bedform are combined (smaller and smoother gradients) as bedform size grows ($C_q1 \rightarrow C_q6$) whereas they tend to split apart (spatially complex and steeper gradients) as fractal dimension increases ($D1 \rightarrow D6$)

However, local peaks do not always match with the local pressure drop, as seen at $x = 1.64$ m in C_q6 for example. There, the flow velocity has decreased due to the large upstream dune blocking the flow. In this case, we cannot directly relate the head to mean flow characteristics used in simple empirical formulae (Elliot, 1991). CFD simulations are able to model the flow separation and recirculation zones behind bedforms and provide more accurate estimates of the head at the bed. The riverbed elevation profile and pressure distributions of $D1$ and $D6$ are depicted in Figure 4.6c and 4.6d. The maximum or minimum elevations are not significantly different between cases, but there are more bedforms in case $D6$, and thus more local pressure gradients associated with the rougher surface.

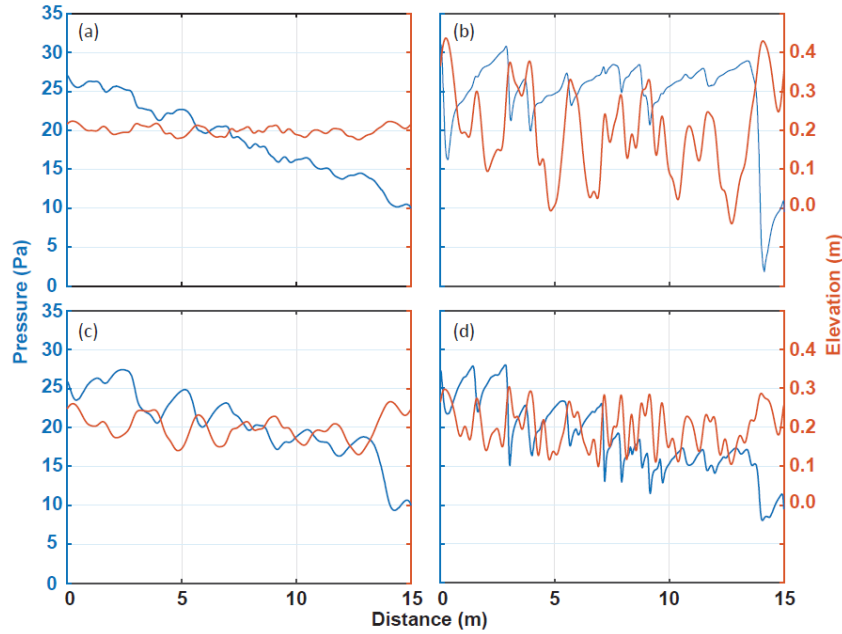


Figure 4.6 Pressure at the sediment-water interface and riverbed elevation for (a) C_q1 (b) C_q6 (c) $D1$ (d) $D6$. The pressure field is closely related to the morphology of riverbeds when the bedform size is small (e.g. (a), (c)). In the cases with large bedforms, they are not directly related due to the flow separation (e.g. (b), (d)).

4.3.2 Effects of Topography on Hyporheic Flux

The average interfacial flux into the hyporheic zone (q_{int}) computed by Eq. 4.22 for each case is shown in Figure 4.7. In both cases, the average interfacial flux increases as C_q or D increases, but with different functional relationships: in Case C_q , the average interfacial flux increases logarithmically with C_q whereas it increases exponentially with D . The logarithm and exponential

function curves are fitted to the data with a coefficient of determination (r^2) greater than 0.99. A linear increase in fractal dimension (D) results in an exponential increase in hyporheic flux, whereas an increase in bedform size (C_q) does not induce much additional flux (e.g., a saturation effect).

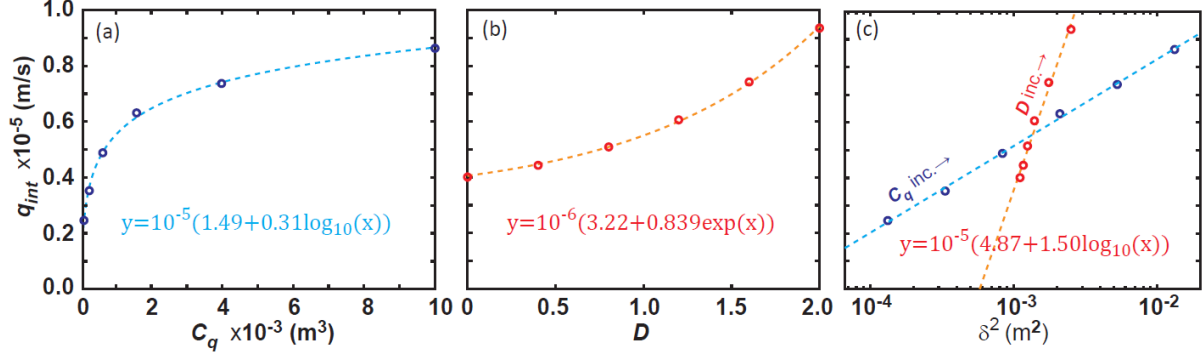


Figure 4.7 Hyporheic exchange with respect to (a) Maximum power spectrum density, C_q (logarithmic function) (b) Fractal dimension, D (exponential function) (c) Surface roughness, δ^2 (logarithmic function). Hyporheic flux increases with increasing δ^2 , and this increase happens more rapidly for the D cases than the C_q cases.

Figure 4.7c illustrates the influence of the mean-square roughness δ^2 on q_{int} . The blue and pink dotted lines indicate the fitting curve for the C_q and D cases, respectively. Both graphs show an increase in flux with increasing δ^2 , but with a much faster increase for the D cases than C_q cases. The additional roughness at larger D is more effective at promoting hyporheic exchange than the mere size of the bedforms (C_q). Moreover, the difference between the two graphs can be interpreted as an additional flux introduced by additional surface roughness (e.g. D6 has rougher bed profile compared to D1). This is similar to the difference between plane beds vs. beds with bedforms (Elliott, 1991; Marion et al., 2002). We also note that the same amount of hyporheic exchange is achieved for the high D case and the high C_q case, but the bedforms in the high D case are only half as big as those in the high C_q case. We conclude from these results that bed roughness, or complexity, is a very strong driver of hyporheic exchange.

4.3.3 Effects of Topography on Residence Time Distributions

The fraction of particles remaining in the bed (\bar{R}) and residence time distributions (RTD) for each case are shown in Figure 4.8a to 4.8d. In addition, the shortest and average residence time

are shown in Figure 4.8e and 4.8f. The observed RTDs conform with the usual power law distributions for hyporheic exchange in bedforms (Cardenas et al., 2008). We observed that the shortest and average residence time decreases as C_q or D increase. Taller bedforms (higher C_q) produce larger head gradients and faster pore water velocity. The multitude of small scales added by increasing D introduces shorter flowpaths and thus shorter travel times. For the C_q cases, especially for C_{q6} , the slope in \bar{R} starts to change at $t = 0.0346 \text{ hr}$ ($\approx 125 \text{ s}$) whereas the change in slope is at $t = 0.033 \text{ hr}$ ($\approx 118 \text{ s}$) for $D6$. It took 95.8 sec and 80.3 sec for particles to circulate through the smallest bedforms for C_{q6} and $D6$ respectively. Since the bedforms in $D6$ are relatively small and since the local head gradients are larger than those of C_{q6} , particles expectedly travel faster.

The slope of the RTD curve changes, and these are indicated by dotted lines on Figures 4.8c and 4.8d. These inflections are due to stagnation points where the flow velocities are small so that they trap particles (Uffink, 1990). This can happen when $\partial \mathbf{D} / \partial \mathbf{x}$ is small compared to \mathbf{U} in zones located between the peak and trough where the direction of flow changes (i.e., at a stagnation zone). Theoretically, this transition in flow direction would not be observed in a flat-bed, but only in beds with topographic features. Since riverbeds are multiscale, multiple stagnation zones are formed and this results in multiple inflection points. The time between two inflection points indicates the travel time from the current to the next stagnation zone. For both D and C_q cases, the riverbed with higher amplitude (e.g., $D6$, C_{q6}) have the earliest inflection because of the higher Darcy flux.

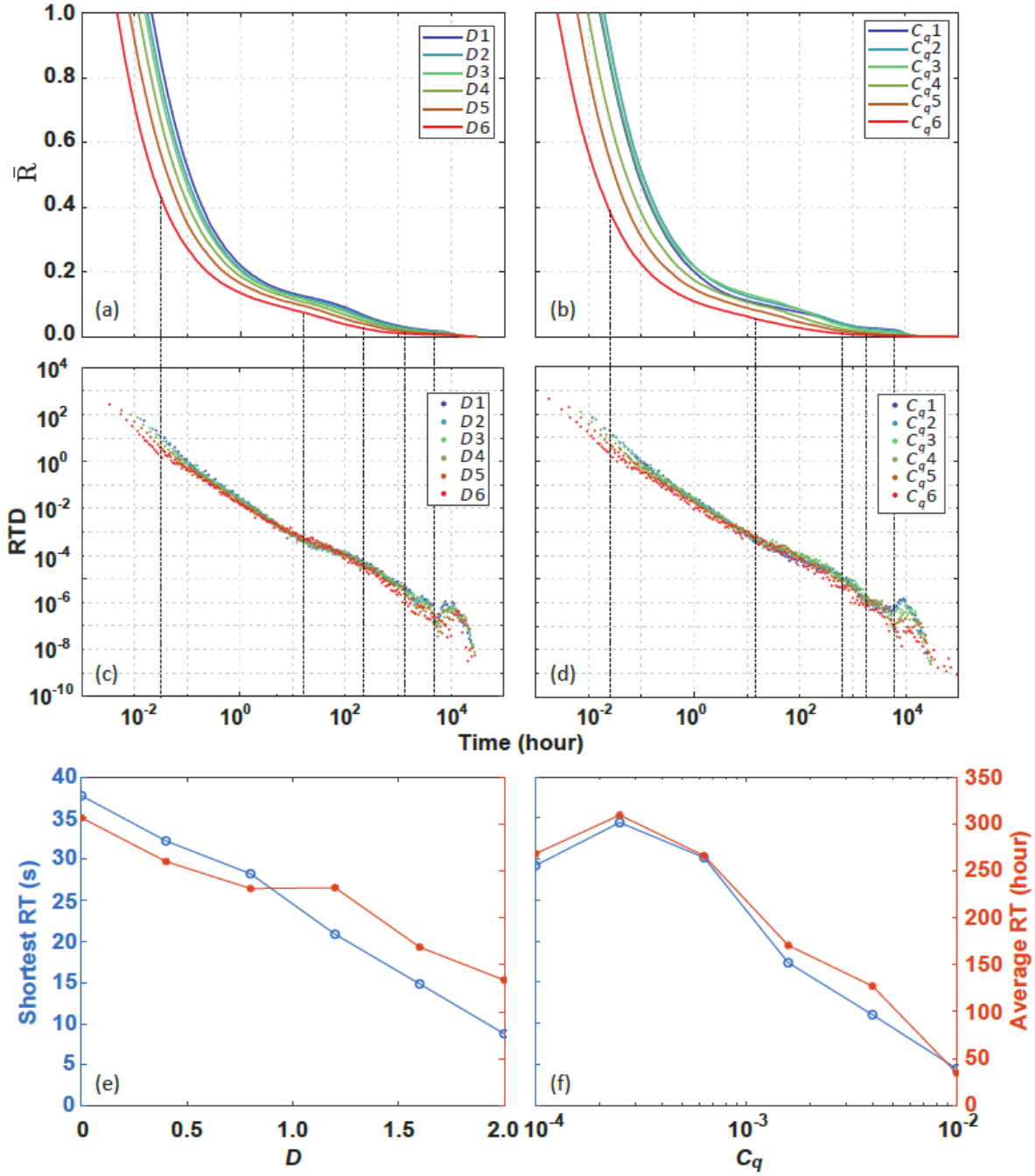


Figure 4.8 Fraction remaining in the bed (\bar{R}) for (a) C_q cases and (b) D cases; Residence time distribution for (c) C_q cases and (d) D cases; The shortest and average residence time for (e) C_q cases and (f) D cases. A couple of inflection points are shown in (a) ~ (d) due to the stagnation point trapping particles for a while and then later releasing them. Both the shortest and average residence times decrease as C_q or D increases for the large bedforms because these increase flow velocity.

4.4 Discussion

Our results demonstrate that the fractal scaling of bedforms exerts a primary control on hyporheic exchange. Hyporheic flux increased exponentially with fractal dimension, whereas it only increased logarithmically with bedform size (C_q cases). This is the first reported systematic investigation quantifying the linkages between the scaling of topography and the exchange behavior. Our findings are consistent with previous studies on the effect of multiscale bedforms on hyporheic exchange. Stonedahl et al. (2013) investigated the contribution of meanders, bars and dunes and showed that small morphologic features (e.g., ripples and dunes) increase hyporheic flux significantly. Similarly, Wörman et al. (2007) showed that smaller-scale features tend to control the surface/subsurface water exchange in fractal landscapes.

Our results could inform a number of critical processes, such as biological filtering for example. The hyporheic zone is a biocatalytic filter that can buffer water quality and influence global nutrient cycles (Fischer et al., 2005; Battin et al., 2008; Huettel et al., 2014; Azizian et al. 2015). Application of our approach requires detailed bed topography in order to extract the fractal scaling and maximum amplitude. These data are becoming easier to collect using green Lidar, multi-beam sonar, and photogrammetry, to name a few relevant methods (Okino and Higashi, 1986; Bufton et al., 1991; Costa et al., 2009; Dietrich, 2017). Given the riverbed topography, it is possible to use our approach to predict hyporheic exchange and thus constrain the associated biogeochemical processing under different topographies. As such, our results could be used to design more efficient biological filters.

The flow separation on the lee side of larger bedforms decreased hyporheic exchange by reducing the pressure variations behind these features. The Bernoulli equation can describe the total head over bedforms with small to mild slopes, but turbulent eddies become important behind larger and steeper bedforms. The Bernoulli equation can be applied to streamlines even near the riverbed where the shearing stresses are not strong enough to disrupt the flow when the slope is mild. The wake observed behind the crest of steeper bedforms indicates the prevalence of frictional forces and this can only be simulated by solving rotational flow equations using CFD. This could help explain the tapering off (logarithmic saturation) of exchange with increasing bedform sizes we observed.

In this study, we used a separate solver for the surface and the subsurface flow, effectively assuming an impermeable interface. Blois et al. (2014) showed that flow separation is very

different above a coarse material than above an impermeable boundary. This suggests that our results may not be valid for coarser and more permeable bed material. We note however that natural bedforms and pumping mechanisms are most important in sand beds (Thibodeaux and Boyle, 1987) while for coarser materials, reach scale channel morphology dominate exchange (Tonina and Buffington, 2009). As the influence of turbulence on hyporheic exchange is critical (Grant et al., 2018), we suggest that using the appropriate surface flow processes (but not systematically the complete Navier-Stokes equations) will become essential to better understand and predict hyporheic exchange. Extending the turbulent domain into the porous space remains an additional important challenge in coarser materials (Roche et al., 2019).

Natural bedforms are complex with superimposed scales and multiple brink points (Catano-Lopera et al., 2009; Lefebvre et al., 2016; Reesink et al., 2018). The roughness is often lacking in the idealized shapes often used in simulations (Cardenas and Wilson, 2007; Trauth et al., 2013; Chen et al., 2018). This simplification can result in underestimating the hyporheic flux by ignoring the head variation driven by the ever-smaller scales such as small ripples on compound dunes for example. The power spectral methods we used can generate artificial riverbeds with multiscale topography and thus better account for the different scales impacting the exchange processes.

In order to isolate the effects of geomorphology on hyporheic exchange, we used the same surface flow conditions in all our simulations. Natural flows are unsteady and often non-uniform, altering hyporheic exchange in space and time (Cardenas and Wilson, 2007; Sawyer et al., 2011; Janssen et al., 2012; Trauth et al., 2013). Assuming constant surface flow conditions also ignores the feedback between hydraulic conditions and bed morphology (Exner, 1925). Incorporating these dynamic feedbacks between flow and morphology may be important in sand riverbeds where bedload and turnover can dominate exchange (Elliott, 1991; Martin and Jerolmack, 2013) and when the hysteresis in the morphological response to unsteady flow controls exchange during crucial flow transitions (Harvey et al., 2012). Finally, because of these nonlinear responses, relict morphology such as bars and other features shaped during high flows but persisting at base flow are also important and can control hyporheic processes and their associated biogeochemical processes (Zarnetske et al., 2011).

Natural bedforms are asymmetrical with a small stoss slope and a large lee-side slope (repose angle), but since we used statistical methods to create our artificial riverbeds, our bedforms are composed of superimposed sinusoids (Fourier series), resembling bedforms created under tidal

currents rather than river flow (Komarova and Newell, 2000; Morelissen et al., 2003; Lefebvre et al., 2011). In symmetrical bedforms, the flow separates at the dune peak but soon reattaches at the lee side (Cardenas and Wilson, 2007). One possible way to resolve this issue is to manipulate the phase spectra in a way that can generate asymmetrical dunes, since phases carries information on the shape of a signal. The phase shift of topography has been poorly studied since it has been often considered to be random (Fox and Hayes, 1985). However, the phase spectra have strong correlations (Figure 4.3c), which should not be regarded as a stationary random process. The relationship between phase spectra and dune shape should be better understood to generate more realistic bedforms.

4.5 Summary and Conclusions

We conducted a series of numerical simulations to systematically explore how the fractal properties of bedforms are related to hyporheic exchange. We compared the average interfacial flux (q_{int}) and RTD in the hyporheic zone with respect to the magnitude of the power spectrum (C_q) and the fractal dimension (D) of riverbeds. First, we created two sets of fractal riverbed topologies: one with different maximum power spectrum density C_q and the other with different fractal dimension D . We then numerically simulated the turbulent flow field over the synthetic riverbeds and used the resultant head distribution as a boundary condition in simulations of hyporheic zone (groundwater) flow fields. Finally, random walk particle tracking simulations were used to quantify residence time distributions in the hyporheic zone.

The results show that the average interfacial flux increases logarithmically with respect to C_q whereas it increases exponentially with respect to D . In addition, q_{int} generally increased with mean-square roughness (δ^2), yet the increases in flux remained more sensitive to increases in D than C_q . The additional roughness at larger D is more important than C_q at increasing q_{int} . These findings confirm that small features tend to dominate hyporheic exchange and imply that roughness is a significant driver of hyporheic exchange.

4.6 References

Aubeneau, A. F., Martin, R. L., Bolster, D., Schumer, R., Jerolmack, D., and Packman, A. I. (2015). Fractal patterns in river morphology produce fractal scaling of water storage times. *Geophys. Res. Lett.*, 42, 5309–5315. <https://doi.org/10.1002/2015GL064155>

- Azizian, M., Grant, S. B., Kessler, A. J., Cook, P. L., Rippy, M. A., and Stewardson, M. J. (2015). Bedforms as biocatalytic filters: A pumping and streamline segregation model for nitrate removal in permeable sediments. *Environmental science and technology*, 49(18), 10993-11002.
- Battin, T. J., Kaplan, L. A., Findlay, S., Hopkinson, C. S., Marti, E., Packman, A. I., et al. (2008). Biophysical controls on organic carbon fluxes in fluvial networks. *Nature Geoscience*, 1, 95-100. <https://doi.org/10.1038/ngeo101>
- Blois, G., Best, J. L., Smith, G. H. S., and Hardy, R. J. (2014). Effect of bed permeability and hyporheic flow on turbulent flow over bed forms. *Geophys. Res. Lett.*, 41, 6435-6442. <https://doi.org/10.1002/2014GL060906>
- Bufton, J. L., Garvin, J. B., Cavanaugh, J. F., Ramos-Izquierdo, L. A., Clem, T. D., and Krabill, W. B. Airborne lidar for profiling of surface topography. *Optical Engineering*, 30(1), <https://doi.org/10.1117/12.55770>
- Cardenas, M. B., and Wilson, J. L. (2007). Dunes, turbulent eddies, and interfacial exchange with permeable sediments. *Water Resour. Res.*, 43, W08412, <https://doi.org/10.1029/2006WR005787>.
- Cardenas, M. B., Wilson, J. L., and Haggerty, R. (2008). Residence time of bedform-driven hyporheic exchange. *Advances in Water Resources*, 31(10), 1382-1386. <https://doi.org/10.1016/j.advwatres>
- Catano-Lopera, Y. A., Abad, J. D. and Garcia, M. H. (2009). Characterization of bedform morphology generated under combined flows and currents using wavelet analysis. *Ocean Eng.*, 36(9-10), 617-632. <https://doi.org/10.1016/j.oceaneng.2009.01.014>
- Chen, X., Cardenas, M. B., and Chen, L. (2018). Hyporheic exchange driven by three-dimensional sandy bedforms: sensitivity to and prediction from bedform geometry. *Water Resources Research*, 54(6), 4131-4149. <https://doi.org/10.1029/2018WR022663>.
- Costa, B. M., Battista, T. A. and Pittman, S. J. (2009) Comparative evaluation of airborne LiDAR and ship-based multibeam SoNAR bathymetry and intensity for mapping coral reef ecosystems. *Remote Sensing of Environment*, 133(5), 1082-1100. doi:10.1016/j.rse.2009.01.015
- Dietrich, J. T. (2017) Bathymetric Structure-from-Motion: extracting shallow stream bathymetry from multi-view stereo photogrammetry. *Earth Surf. Process. Landforms*, 42, 355-364. doi:10.1002/esp.4060
- Elliott, A. H. (1991) Transfer of solutes into and out of streambeds, (Doctoral dissertation). Retrieved from CaltechTHESIS. (<http://resolver.caltech.edu/CaltechETD:etd-07092007-074127>). Pasadena, CA: California Institute of Technology.
- Exner, F. M. (1925). U'ber die Wechselwirkung zwischen Wasser und Geschiebe in Flu'ssen (in German), Sitz. Acad. Wiss. Wien Math. Natur-wiss. Abt. 2a, 134, 165-203

- Fischer, H., Kloep, F., Wilzcek, S. and Pusch, M. T. (2005). A River's Liver – Microbial Processes within the Hyporheic Zone of a Large Lowland River. *Biogeochemistry*, 76: 349. <https://doi.org/10.1007/s10533-005-6896-y>
- Fox, C. G., and Hayes, D. E. (1985). Quantitative methods for analyzing the roughness of the seafloor. *Rev. Geophys.*, 23, 1-48. <https://doi.org/10.1029/RG023i001p00001>.
- Grant, S. B., Gomez-Velez, J. D., and Ghisalberti, M. (2018). Modeling the effects of turbulence on hyporheic exchange and local-to-global nutrient processing in streams. *Water Resources Research*, 54, 5883–5889. <https://doi.org/10.1029/2018WR023078>
- Harvey, J. W., Drummond, J. D., Martin, R. L., MacPhillips, L. E., Packman, A. I., Jerolmack, D. J., et al. (2012). Hydrogeomorphology of the hyporheic zone: Stream solute and fine particle interactions with a dynamic streambed. *J. Geophys. Res.*, 117, G00N11, <https://doi.org/10.1029/2012JG002043>.
- Huettel, M., Berg, P. and Kostka, J. E. (2014). Benthic Exchange and Biogeochemical Cycling in Permeable Sediments. *Annu. Rev. Mar. Sci.*, 6, 23–51.
- Janssen, F., Cardenas, M. B., Sawyer, A. H., Dammrich, T., Krietsch, J., and de Beer, D. (2012). A comparative experimental and multiphysics computational fluid dynamics study of coupled surface–subsurface flow in bed forms. *Water Resour. Res.*, 48, W08514, <https://doi.org/10.1029/2012WR011982>.
- Kitanidis, P. K. (1994). The concept of the Dilution Index. *Water Resour. Res.*, 30(7), 2011–2026. <https://doi.org/10.1029/94WR00762>.
- Komarova, N., and Newell, A. (2000). Nonlinear dynamics of sand banks and sand waves. *Journal of Fluid Mechanics* 415, 285–321.
- Lefebvre, A., Ernsten, V. B., and Winter, C. (2011). Bedform characterization through 2D spectral analysis. *J. of Coast. Res.*, SI 64 (Proceedings of the 11th International Coastal Symposium), 781-785. Szczecin, Poland, ISSN 0749-0208.
- Lefebvre, A., Paarlberge, A. J., and Winter, C. (2016). Characterising natural bedform morphology and its influence on flow. *Geo-Mar. Lett.*, 36, 379–393. <https://doi.org/10.1007/s00367-016-0455-5>
- Logg, A., Mardal, K. A., and Wells, G.N (eds.) (2012). *Automated Solution of Differential Equations by the Finite Element Method: The FEniCS Book*. Springer: Berlin
- Malinverno, A., and Gilbert, L. E. (1989). A stochastic model for the creation of abyssal hill topography at a slow spreading center. *J. Geophys. Res.*, 94(B2), 1665–1675. <https://doi.org/10.1029/JB094iB02p01665>.
- Marion, A., Bellinello, M., Guymer, I., Packman, A. I. (2002). Effect of bed form geometry on the penetration of nonreactive solutes into a streambed. *Water Resour. Res.*, 38(10), 1209, <https://doi.org/doi:10.1029/2001WR000264>.

- Martin, R. L., and Jerolmack, D. J. (2013). Origin of hysteresis in bed form response to unsteady flows. *Water Resour. Res.*, 49, 1314–1333. <https://doi.org/10.1002/wrcr.20093>.
- Moltyaner, G. L., and Killey, R. W. D. (1988). Twin Lake Tracer Tests: Transverse dispersion. *Water Resour. Res.*, 24(10), 1628–1637. <https://doi.org/10.1029/WR024i010p01628>.
- Morelissen, R., Hulscher, S. J. M. H., Knaapen, M. A. F., Németh, A. and Bijker, R. (2003). Mathematical modeling of sand wave migration and the interaction with pipelines. *Coastal Engineering* 48, 197–209.
- Okino, M. and Higashi, Y. (1986) Measurement of seabed topography by multibeam sonar using CFFT. 11(4), 474-479. doi: 10.1109/JOE.1986.1145209
- Reesink, A. J. H., Parsons, D. R., Ashworth, P. J., Best, J. L., Hardy, R. J., Murphy, B. J., et al. (2018). The adaptation of dunes to changes in river flow, *Earth-Science Reviews*, 185, 1065–1087. ISSN 0012-8252, <https://doi.org/10.1016/j.earscirev.2018.09.002>
- Roche, K. R., Li, A., Bolster, D., Wagner, G. J., and Packman, A. I. (2019). Effects of turbulent hyporheic mixing on reach-scale transport. *Water Resources Research*, 55, 3780–3795. <https://doi.org/10.1029/2018WR023421>
- Sawyer, A. H., Cardenas, M. Bayani, and Buttles, J. (2011). Hyporheic exchange due to channel-spanning logs. *Water Resour. Res.*, 47, W08502, <https://doi.org/10.1029/2011WR010484>
- Simons, D. B., and Richardson, E. V. (1966). Resistance to flow in alluvial channels. Professional Paper 422-J, U.S. Geological Survey, Washington D.C.
- Southard, J. B. and Boguchwal, L. A. (1990). Bed configurations in steady unidirectional water flows. Part 2. Synthesis of flume data. *Journal of Sedimentary Petrology* 60, 649–657.
- Stonedahl, S. H., Harvey, J. W., and Packman, A. I. (2013). Interactions between hyporheic flow produced by stream meanders, bars, and dunes. *Water Resour. Res.*, 49, 5450–5461. <https://doi.org/10.1002/wrcr.20400>.
- Stonedahl, S. H., Harvey, J. W., Wörman, A., Salehin, M., and Packman, A. I. (2010). A multiscale model for integrating hyporheic exchange from ripples to meanders. *Water Resour. Res.*, 46, W12539, <https://doi.org/10.1029/2009WR008865>.
- Thilbodeaux, L. J. and Boyle, J. D (1987). Bedform-generated convective transport in bottom sediment, *Nature*, 325, 341–343. <https://doi.org/10.1038/325341a0>
- Trauth, N., Schmidt, C., Maier, U., Vieweg, M., and Fleckenstein, J. H. (2013). Coupled 3-D stream flow and hyporheic flow model under varying stream and ambient groundwater flow conditions in a pool-riffle system. *Water Resour. Res.*, 49, 5834–5850. <https://doi.org/10.1002/wrcr.20442>.

- Tonina, D. and Buffington, J. M. (2009) Hyporheic exchange in mountain rivers I: Mechanics and Environmental Effects. *Geography Compass*, 3(3):1063–1086.
<https://doi.org/10.1111/j.1749-8198.2009.00226.x>.
- Turcotte, D. (1997). *Fractals and Chaos in Geology and Geophysics*, Cambridge University Press, The Edinburgh Building, Cambridge CB2 8RU, UK
- Uffink, G. J. M. (1990). Analysis of dispersion by the random walk method, (Doctoral dissertation). Retrieved from Institutional Repository. (<http://resolver.tudelft.nl/uuid:cef0af43-fda7-4ce4-907a-87027ccb67be>). Delft, Netherlands: Delft University of Technology.
- Versteeg, H. K. and Malalasekera, W. (2007). *An Introduction to Computational Fluid Dynamics: The Finite Volume Method*. John Wiley and Sons Inc., New York.
- Wörman, A., Packman, A. I., Marklund, L., Harvey, J. W., and Stonedahl, S. H. (2007). Fractal topography and subsurface water flows from fluvial bedforms to the continental shield. *Geophys. Res. Lett.*, 34, L07402, <https://doi.org/10.1029/2007GL029426>.
- Zarnetske, J. P., Haggerty, R., Wondzell, S. M. and Baker, M. A. (2011). Dynamics of nitrate production and removal as a function of residence time in the hyporheic zone. *J. Geophys. Res.*, 116, G01025, <https://doi.org/10.1029/2010JG001356>

5. HYPORHEIC EXCHANGE THROUGH DUNES IN HIGH FROUDE NUMBER CHANNEL FLOWS WITH A FREE WATER SURFACE

Hyporheic exchange in streams and rivers affects water quality and biogeochemical cycles. Hyporheic exchange is driven by head gradients arising from changes in water depth or velocity. Since the Froude number expresses the ratio of inertial forces to gravitational forces, it is a concise description of the main drivers of hyporheic exchange. Through simulations, this research explores how the hyporheic exchange between the overlying flow and a dune changes with the Froude number. We hypothesize that accounting for two-phase flow at the air-water interface will result in relationships between Froude number and hyporheic exchange that have so far been missed by previous studies which ignored the free water surface. We conducted coupled numerical open channel and hyporheic flow simulations which compare cases with a free water surface (two-phase air and water flow) with corresponding rigid-lid top boundaries for the channel (Figure 5.1). Our results show that hyporheic flux increases linearly with average Froude number in the fixed-surface case but nonlinearly when the water surface is free. This means that consideration for two-phase flow might be critical under certain Froude number conditions. Otherwise, model results are inaccurate and not representative.

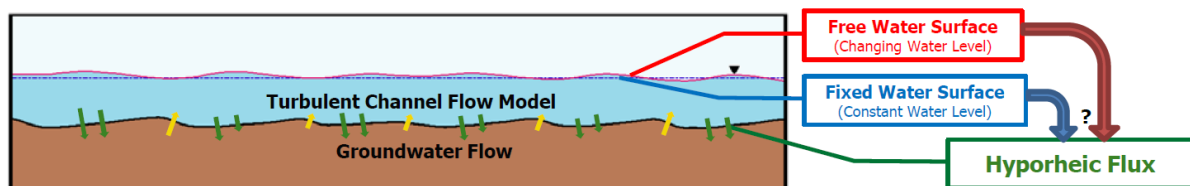


Figure 5.1 A sequentially coupled surface-subsurface model: Both the channel (surface) flow and groundwater (subsurface) flow were solved using OpenFOAM. The pressure values from the channel flow simulations were imposed at the upper boundary of groundwater which is the sediment-water interface. We compare two different simulations, one with fixed water surface and the other with free water surface, in terms of the channel flow field, total head at the sediment-water interface and hyporheic flux under various flow conditions. We hypothesize (1) the hydrostatic pressure would increase at the dune trough and decrease at the dune peak generating larger head gradient when the water is free to move and (2) the frictional force between air-water would change the velocity field for the flow with free-surface flow.

5.1 Generation of synthetic riverbed morphology

The morphodynamic model developed by Jerolmack and Mohrig (2005) was used to generate fluvial dunes. The surface-evolution equation including stochastic noise term has the form of:

$$\begin{aligned} \frac{\partial \eta}{\partial t} = & \langle q_s \rangle \frac{n}{1-\phi} \left(\frac{A}{\langle h \rangle} + B \frac{\partial^2 \eta}{\partial x^2} \right) \left(1 + A \frac{\eta}{\langle h \rangle} + B \frac{\partial \eta}{\partial x} \right)^{n-1} \\ & + D \frac{\partial^2 \eta}{\partial y^2} + \zeta(x, y, t) \end{aligned} \quad (5.1)$$

where η is bed elevation, $\langle h \rangle$ is sediment flux with dimensions L^2/T , ϕ is porosity, n is an exponent for sediment transport which generally has a value of 1.5, $\langle h \rangle$ is spatially averaged depth of flow, A and B are shape parameters, D is lateral diffusion coefficient and $\zeta(x, y, t)$ is Gaussian-distributed low-amplitude white noise. The parameters used to generate the morphology are the following: $\Delta x = 0.1$, $\Delta t = 0.002$, $A = 4.3$, $B = 4.3$, $D = 0.025$, $\zeta = 0.1$, $n = 1.5$, $\phi = 0.4$. The same model parameters values from Jerolmack and Mohrig (2005) were used. The morphology is then rescaled so that the dune spacing (length, L) is 1.4 m and the dune height (H) is 0.1 m. The dune spacing and the height were estimated by a bedform stability diagrams from Southard and Boguchwal (1990). The mean flow velocity and the mean flow depth used to determine the dune spacing are 0.6 m/s and 0.3 m, respectively.

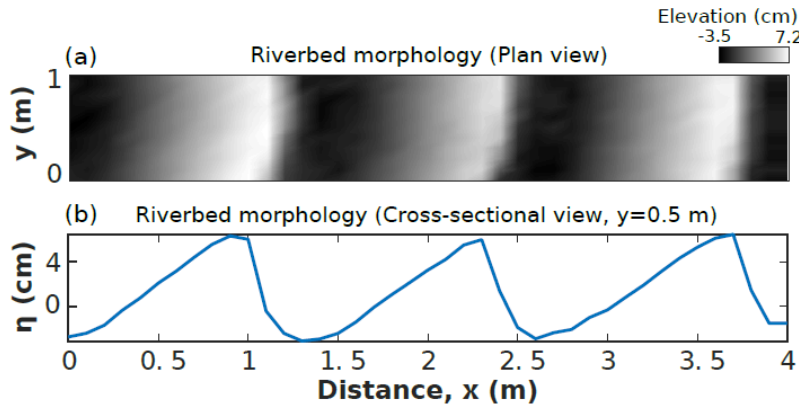


Figure 5.2 Riverbed morphology generated from Jerolmack and Mohrig (2005) with the following parameters: $\Delta x = 0.1$, $\Delta t = 0.002$, $A = 4.3$, $B = 4.3$, $D = 0.025$, $\zeta = 0.1$, $n = 1.5$, $p = 0.4$. The length and height of dune are rescaled to 1.4 m and 0.1 m, respectively. (a) The plan view (x - y) of the riverbed profile (b) The cross-sectional view (x - z) of the riverbed profile.

5.2 Simulation conditions

The surface water flow is modeled by solving the Navier-Stokes equations with a $k - \epsilon$ turbulence closure model. An air-water mixture model, the Volume of Fluid (Hirt and Nichols, 1981) method, is used to simulate open-channel flows. The simulation platform used in this research is the open source CFD package OpenFOAM (<https://openfoam.org/>). The interFoam solver within OpenFOAM was used to simulate the free surface flow in the surface domain. A new solver was written using the OpenFOAM platform to solve the porous media flow equation. The simulations were conducted in a two-dimensional domain, with cardinal directions x -dir (streamwise direction) and z -dir (gravitational force direction). For the surface flow, we compared two different cases: one with a fixed-surface and the other with a free-surface in order to see how they produce different head distributions and hyporheic flux.

Open-channel flows are naturally driven by the x -dir component of gravitational force, $\rho \mathbf{g}_x$ as in Eq. (5.2). However, since the simulation domain in this work is periodic in the x -dir, special treatment is used to make the pressure field compatible with the periodicity requirement. Indeed, in all simulations, a desired mean flow velocity, $\bar{\mathbf{U}}$, (equivalently desired discharge) is enforced through an adjustable body force in the momentum equation. At every time step, the gravity term in the streamwise direction (adjustable body force) in the momentum equations of surface and subsurface flow, Eq. (3.15) and (3.26), is calculated as follows:

$$\rho \mathbf{g}_x = \omega \frac{(|\bar{\mathbf{U}}| - |U_{avg}|)}{a_p} \quad (5.2)$$

where ω is a relaxation factor which is 0.2 in this study, $|U_{avg}|$ is the magnitude of the volume-averaged streamwise velocity, and a_p is the diagonal elements of the linear system of equation for velocity. In this study, the mean flow velocity, $\bar{\mathbf{U}}$, varies from 0.1 to 1.5 m/s with a 0.2 m/s interval.

The length (x -dir) and height (z -dir) of the bedform are 1.4 m and 0.06 m while the average channel water depth and the depth of the groundwater domain (z -dir) are set to 0.3 m and 1 m, respectively. We tested three different meshes satisfying $y^+ = 5, 10, 30$ near the bed and the one with $y^+ = 10$ is chosen for accuracy and efficiency. A cyclic (periodic) boundary condition is applied to the inlet and outlet for both surface and subsurface flow models. A no-slip boundary is used at the bottom boundary of the surface flow (e.g., sediment-water interface) and subsurface

flow domains. The simulated pressure values at the bottom of the surface water flow domain are imposed as the upper boundary condition (Dirichlet boundary) of the subsurface flow model.

The dimensionless Froude number expresses the ratio of inertial forces to gravitational forces, and is thus a concise description of the main drivers of hyporheic exchange. The Froude number is defined as:

$$Fr = \frac{\bar{U}}{\sqrt{gh_m}} \quad (5.3)$$

where \bar{U} and h_m are the averaged flow velocity and hydraulic mean depth, and g is gravitational acceleration. Since we assume two-dimensional flow and the channel is considered as a wide-rectangular shape, h_m is approximated as water depth (h). In Figure 5.3, we denote Fr_{avg} as $\bar{U}/\sqrt{gh_{avg}}$, where $h_{avg} = 0.3$ m.

5.3 Model validation

We validated our model with the measured velocity and surface water elevation data obtained by van Mierlo and de Ruiter (1988). They created an artificial dune and measured flow properties such as time-averaged water velocity eddy viscosity. We used one of the experiment results named T6 to validate how our numerical model. The discharge of this experiment is 0.257 m³/s. Figure 5.3 shows the riverbed elevation along with the measured and simulated water surface profile: the simulated profile shows a good agreement with the measured profile.

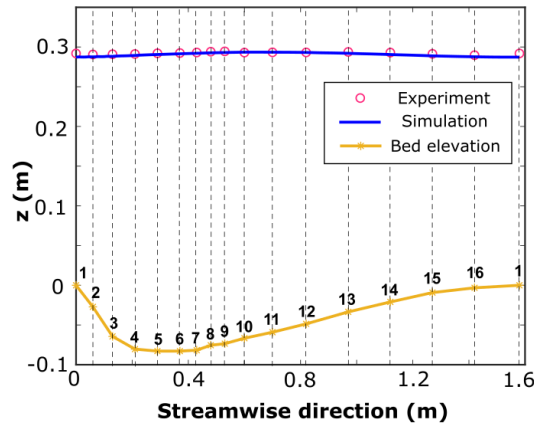


Figure 5.3 The riverbed elevation (Yellow line with asterisks) along with the measured (magenta circle) and simulated water surface profile (Blue solid line): the simulated profile shows a good agreement with the measured profile.

Figure 5.4 depicts the measured and simulated flow velocity profiles where z^* is the elevation normalized by the water depth at location 1 and U^* is the velocity normalized by the depth-averaged flow velocity. The blue line represents the water surface elevation. The number for each subfigure denotes the reference location which corresponds to the number in Figure 5.2. The simulated velocity profile also showed a great agreement with the experimental data.

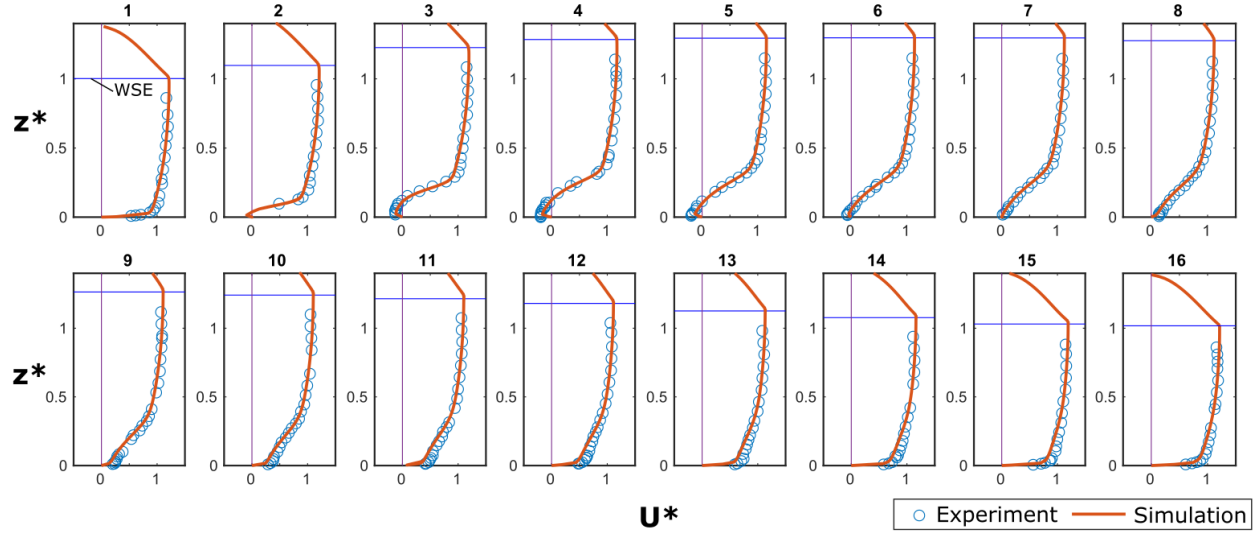


Figure 5.4 The measured (Blue circle) and simulated flow velocity (orange solid line) profiles where z^* is the elevation normalized by the water depth at location 1 and U^* is the velocity normalized by the depth-averaged flow velocity. The blue line represents the water surface elevation. The simulated flow velocity shows a good agreement with the experiment data.

5.4 Results

5.4.1 Water surface profiles and surface flow fields

Figure 5.5 shows the results for a range of Froude numbers. Depicted are the channel velocity fields with the free-surface profile for the surface flow model (upper domain) and the dynamic pressure fields and streamlines for the subsurface flow model (lower domain). By definition, the surface water elevation for the fixed case was held constant and flat. On the other hand, the free-surface elevation for the cases where the surface moved required additional analysis. The surface was mapped by extracting the iso-surface of the time-averaged $F = 0.9$ from the simulation results (see Eq. (3.8)).

At small Froude numbers (e.g., $Fr_{avg} < 0.5$, Figure 5.5a-d), the water surface profile is almost flat, except a small undulation in Figure 5.5d. Starting from Figure 5.5e with $Fr_{avg} = 0.52$, the

water surface profile starts to change with respect to the bedform shape. For larger Froude numbers (e.g., $Fr_{avg} > 0.5$, Figure 5.5e-h), we observe a boil on the water surface downstream of the crest. In addition, the water profile undulates more as Fr_{avg} increases.

Flow separation is observed except for cases with the highest Froude number, $Fr_{avg} = 0.87$. For the cases with $Fr_{avg} < 0.5$ (Figure 5.5a ~ 5.5d), the detachment length representing the scale of recirculation zone gets larger as Froude number increases. For the cases with $Fr_{avg} > 0.5$ (Figure 5.5e ~ 5.5h), the recirculation zone starts to shrink as the Froude number increases. The shallower depth at the dune crest and lee side because of the adjusting water surface results in increasing velocity near the bed. For the cases with high Froude numbers such as Figure 5.5g and 5.5h, the separation zone is further reduced in size and the surface elevation resembled a dampened and shifted dune profile.

Figure 5.6. depicts the velocity profile at the peak of the dune for cases having $Fr_{avg} > 0.5$. When the water surface elevation is fixed, the velocity profile at the dune peak is distributed in a way that the velocity is zero at the sediment bed and has a maximum value at the water-air interface. In the free-surface case, the location where the velocity is maximum moves closer to the bed (away from the surface) at high Froude number. This is because the water-mixture model considers frictional forces between water and air reducing the velocity at the water-air interface. The mean flow maps presented in Best (2005) show a similar pattern which has a maximum velocity near the bed rather than the water-surface elevation.

The total head at the sediment-water interface for the fixed and free-surface case are depicted in Figure 5.5. The total head at the riverbed for both fixed-surface and free-surface is computed by summing the dynamic and hydrostatic heads. Note the summation of hydrostatic pressure head and elevation head is constant in the fixed-surface cases. For both fixed-surface and free-surface case, the head drop at the peak becomes larger as Fr increases. This is because the magnitude of dynamic pressure driven by a bedform gets larger as the flow velocity increases. This can be partly explained by the Bernoulli equation: for two points lying on a streamline near the bed, we can write

$$\left(\frac{p}{\gamma} + z + \frac{v^2}{2g}\right)_1 = \left(\frac{p}{\gamma} + z + \frac{v^2}{2g}\right)_2 \quad (5.4)$$

where p is pressure, γ is the specific weight of water, z is elevation, and v is velocity.

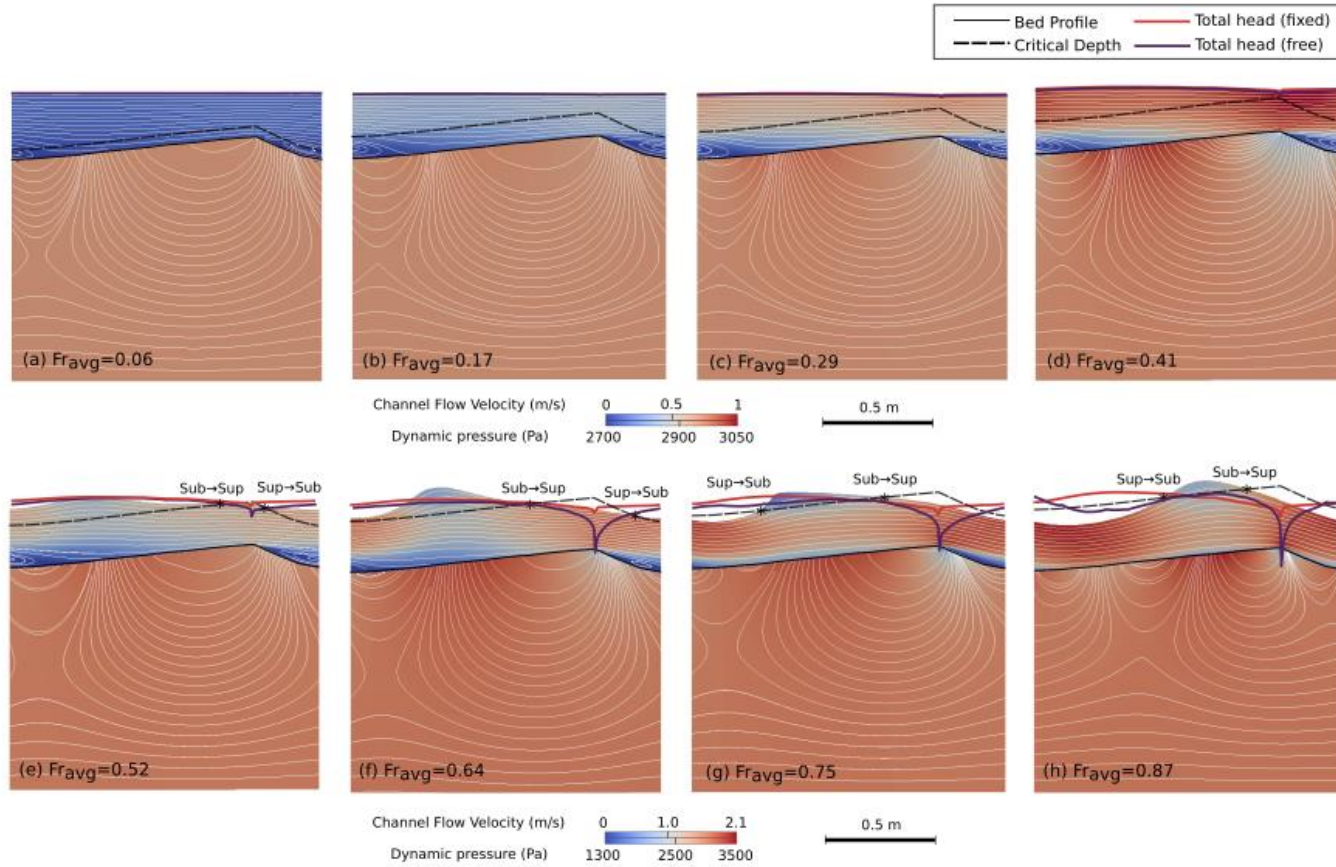


Figure 5.5 The channel velocity field with free-surface (surface flow, upper domain) and dynamic pressure field (subsurface flow, lower domain) are depicted for various flow conditions: $Fr_{avg} =$ (a) 0.06 (b) 0.17 (c) 0.29 (d) 0.41 (e) 0.52 (f) 0.64 (g) 0.76 (h) 0.87. White lines represent the flowpath in both surface and subsurface domain. In the surface domain, the total head for the fixed-surface case (Red) and for the free-surface case (Purple) are drawn along with bedform elevation (solid black line). The dotted black line indicates the critical depth and the asterisks (*) local flow regime changes (e.g. sub \rightarrow sup, sup \rightarrow sub) wherever this line intercepts the water level. We observe an increase in flow velocity near the bed inducing a large head drop at the peak when the water surface is free to move.

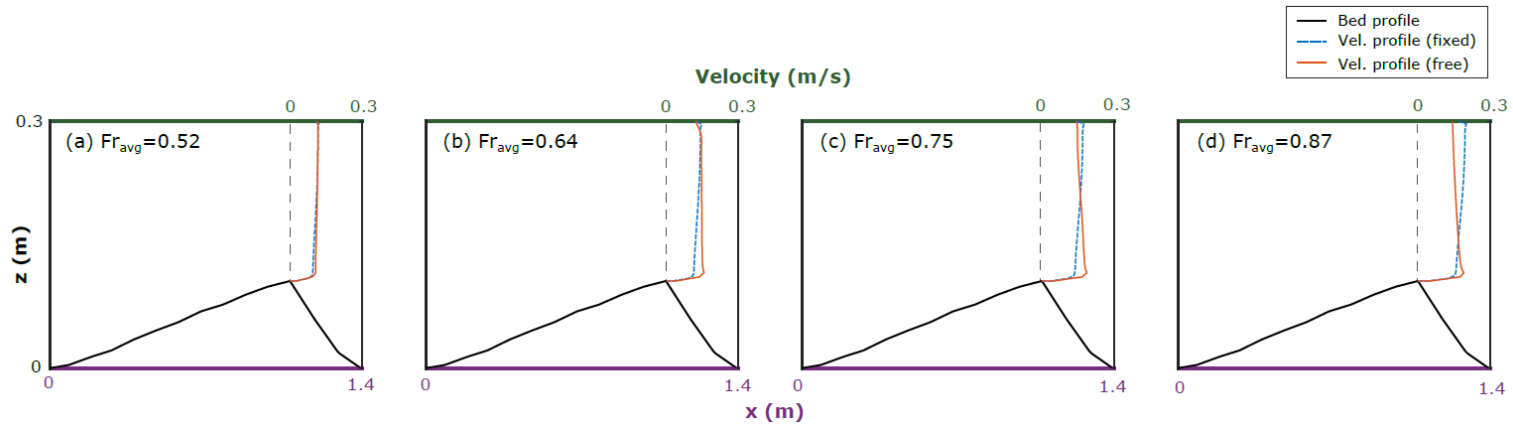


Figure 5.6 The vertical velocity profile of channel flow at the peak of the dune for fixed-surface (blue dotted line) and free-surface case (orange solide line) for various flow conditions: $Fr_{avg} =$ (a) 0.52 (b) 0.64 (c) 0.76 (d) 0.87. The upper x-axis represents the magnitude of horizontal velocity (green) and the lower x-axis is x-dir distance (purple). When the water surface elevation is fixed, the velocity profile at the dune peak is distributed in a way that the velocity is zero at the sediment bed and has maximum value at the water-air interface. In the free-surface case, the location where the velocity is maximum moves closer to the bed (away from the surface) at high Froude number.

The total head (pressure head + elevation head) difference between two points is then

$$\nabla h = \frac{p_2 - p_1}{\gamma} + z_2 - z_1 = \frac{(v_1^2 - v_2^2)}{2g} \quad (5.5)$$

The head drop at the dune crest is always larger in free-surface case. For fixed-surface case, since the log-law profile is applicable throughout the surface domain, the difference in v^2 between two points near the bed (e.g. $v_1^2 - v_2^2$ in Eq. (5.5)) is proportional to the squared mean velocity, \bar{U}^2 . However, this scaling relationship between ∇h and \bar{U}^2 is no longer valid in free-surface case as Fr_{avg} increases. This is because the velocity profile at the dune crest does not follow the conventional log-law profile when Fr_{avg} is large. As shown in Figure 5.6, the velocity near the bed in free-surface case rapidly increases compared to that in fixed-surface case. We found that friction between air and water at the interface is one of the reasons causing this nonlinear increase in near-bed velocity.

5.4.2 Hyporheic flux

The relationship between Fr_{avg} and total interfacial flux normalized by mean velocity is shown in Figure 5.7. The blue dots and dotted line represent the hyporheic flux and corresponding fitted line for the fixed-surface cases and the red symbols are for the free-surface cases. The normalized flux increases almost linearly as Fr_{avg} increases in the fixed-surface case. A regression analysis shows that $y = 2.69 \times 10^{-5}x$ (R-squared: 0.9990, RMSE: 2.32×10^{-7}) with x and y being Fr_{avg} and averaged flux, respectively. In contrast, the normalized flux in the free-surface case increases nonlinearly as Fr_{avg} increases. Since there are two different patterns in free-surface case, the former part with small Fr_{avg} and the latter part with large Fr_{avg} , we divided them into two groups. For the former 5 cases, the power-law fitting curve is $y = 3.77 \times 10^{-5}x^{1.17}$ (R-squared: 0.9482, RMSE: 1.67×10^{-6}). Dots in the latter part with large Fr_{avg} do not follow the regression line fitted for the former 5 cases, yet increased significantly.

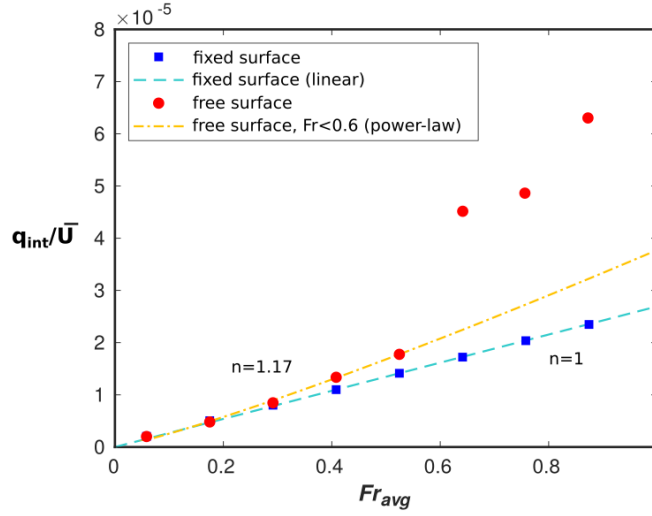


Figure 5.7 Relationship between the average Froude number (Fr_{avg}) and the normalized hyporheic flux (q_{int}/\bar{U}). The hyporheic flux increases linearly with Fr_{avg} in fixed surface case (blue circular dots, a linear regression line (skyblue dotted line) $= 2.69 \times 10^{-5}x$, $R^2 = 0.9993$).

In free-surface case, the power-law fitting curve is $y = 3.77 \times 10^{-5}x^{1.17}$ (R-squared: 0.9482, RMSE: 1.67×10^{-6}) for the former 5 cases

Sawyer et al. (2011) proposed the relationship between Froude number and mean hyporheic flux (q^*), $q^* \propto Fr^2$. In this study, we also observed the relationship between the normalized hyporheic flux and Froude number, $q_{int}/\bar{U} \propto Fr$, for the fixed-surface case. These two relationships are equivalent since $Fr_{avg} \propto \bar{U}$. As mentioned in 3.2, since the log-law profile is applicable throughout the surface domain for fixed-surface case, the total head gradient is proportional to the squared mean flow velocity, $\nabla h \propto \bar{U}^2$, and consequently, $q^* \propto \bar{U}^2$. In free-surface case, this correlation between q^* and \bar{U}^2 is no longer valid since the velocity profile at the dune peak does not follow the conventional log-law profile when Fr_{avg} is large. Figure 5.6 shows the velocity near the bed in free-surface case rapidly increases compared to that in fixed-surface case. One of the reasons for this nonlinear increase in near-bed velocity is that the air-water mixture model considers the interaction between air and water, such as frictional forces.

5.5 Discussion

We observed the flow field was very different when the water was free to move for $Fr_{avg} > 0.5$. Since the air-water mixture model takes into account the frictional force between air and water, the velocity at the air-water interface is reduced, resulting in a disproportionate

increase in flow velocity at the dune peak compared to the fixed surface. This mechanism induces a decrease in total head at the peak, bringing an increased hyporheic flux. The (static) head gradients introduced by the change in water levels was not considerable, but instead the change in velocities drove the hyporheic flux increase. In other words, using the air-water mixture model does not just change the SWE, but it changes the entire channel flow field by considering the frictional effects between air and water and their cascading effects at depth. For two-dimensional stream flow and morphology as in this research or in Sawyer et al. (2011), the relationship between hyporheic flux and channel Froude number is highly correlated. In contrast, for three-dimensional case, it is difficult to derive a meaningful relationship between hyporheic flux and channel Froude number (Trauth et al., 2013). Our future work is to study the mechanism of three-dimensional channel flow over complex geometry to analyze how the flow interacts with morphology.

By examining the relationship between the Froude number and hyporheic exchange, and by comparing the fixed-surface cases with the free-surface cases, we are able to provide a simple criterion for when a fixed surface model can be used. Especially, when it comes to large-scale hyporheic exchange simulation as in Zhou (2018), the computational effort can be reduced depending on the Froude number of channel flow. When the average Froude number is smaller than 0.5, the hyporheic flux was not much different, and the extra effort to run a VoF simulation is not needed. However, when the average Froude number is larger than 0.5, the hyporheic flux increases considerably and nonlinearly. In that case, the air-water mixture model should be used in order to take the interaction between air and water into account and calculate hyporheic exchange. For example, at the highest Fr number we simulated, the normalized flux was more than three times higher when using the free surface model.

We coupled the surface and subsurface model by imposing the head values obtained from the surface water flow simulation to the sediment-water interface. We assumed the velocity is zero at the sediment-water interface when simulating the channel flow while water actually seeps in and out of the subsurface. The assumption is reasonable because the maximum subsurface flow velocity with highest mean velocity was 3.9×10^{-4} m/s, which is trivial compared to the average stream flow velocity, 1.5 m/s. Nevertheless, the development of fully-coupled surface-subsurface model is needed since up and downwelling fluxes play a key role for the transport of pollutants at the surface/groundwater interfaces (Layton et al., 2002; Cesmelioglu et al., 2020). Analytical methods to couple Stokes flow (homogeneous fluid flow, e.g. channel flow) with Darcy flow (porous media flow) have been developed (Ochoa-Tapia and Whitaker,

1995; Vafai and Kim, 1990; Alazmi and Vafai, 2001; Discacciati et al., 2002; Gatica and Sequeira, 2017) for almost a half century since Beavers and Joseph (1967), but the channel flow condition is limited to laminar. It remains challenging to couple turbulent flows across the porous boundary because the no-slip boundary condition is no longer applicable at the streambed but around individual grains, rendering simulations prohibitively expensive for most practical situations.

5.6 Summary and conclusions

We conducted a series of numerical simulations to explore how the Froude number affects the free-surface profile, total head over sediment bed and hyporheic flux. For larger Froude numbers (e.g. $Fr_{avg} > 0.5$), a boil on the water after the peak is observed. The water profile undulates more as Fr_{avg} increases. The difference between the fixed-surface and free-surface case becomes significant as Froude number increases. For larger Fr_{avg} , the head at the peak of the dune for free-surface case is smaller than that of fixed-surface case inducing larger head gradient. This is mainly because they have different velocity profile at the dune peak: in the fixed-surface case, the vertical velocity profile from the bottom to the air-water interface follows the law of the wall so that the velocity at the air-water interface has the maximum value. On the contrary, in the free-surface case, the velocity at the interface no longer has the maximum value: the location having the maximum velocity moves closer to the sediment bed. This results in increasing velocity near the bed and larger head gradients, accordingly.

Finally, we found that the normalized hyporheic flux increases linearly as Fr_{avg} increases in the fixed-surface case which is also suggested by Sawyer et al. (2011). This can be explained by applying Bernoulli equation for a streamline near the riverbed for any two points on the streamline. The total head difference between two points is then $\nabla h \propto \bar{U}^2$, and consequently, $q^* \propto \bar{U}^2$. In the free surface case, ∇h and $q^* \propto \bar{U}^3$ and in near critical flows, the normalized flux is several times higher than predicted by the classic fixed surface simulations. These differences in hyporheic fluxes could have important consequences in evaluating the fluxes of major elements at the surface/groundwater interfaces.

5.7 References

- Alazmi, B., and Vafai, K. (2001). Analysis of fluid flow and heat transfer interfacial conditions between a porous medium and a fluid layer. *International Journal of Heat and Mass Transfer*, 44 (9), 1735–1749. doi:10.1016/S0017-9310(00)00217-9
- Beavers, G. S., and Joseph, D. D. (1967). Boundary conditions at a naturally permeable wall. *Journal of Fluid Mechanics* (March 2006). doi:10.1017/S0022112067001375
- Best, J. (2005). Kinematics, Topology and Significance of Dune-Related Macroturbulence: Some Observations from the Laboratory and Field. *Fluvial Sedimentology VII* , 41–60. doi: 10.1002/9781444304350.ch3
- Cesmelioglu, A., Rhebergen, S., and Wells, G. N. (2020). An embedded hybridized discontinuous Galerkin method for the coupled Stokes Darcy system. *Journal of Computational and Applied Mathematics*, 367, 112476. doi: 10.1016/j.cam.2019.112476
- Discacciati, M., Miglio, E., and Quarteroni, A. (2002). Mathematical and numerical models for coupling surface and groundwater flows. *Applied Numerical Mathematics*, 43 (1-2), 57–74. doi: 10.1016/S01689274(02)00125-3
- Gatica, G. N., and Sequeira, F. A. (2017). Analysis of the HDG Method for the Stokes-Darcy Coupling. *Numerical Methods for Partial Differential Equations*, 33, 885–917. doi: 10.1002/num.22128
- Hirt, C. W., and Nichols, B. D. (1981). Volume of Fluid (VOF) Method for the Dynamics of Free Boundaries. *Journal of computational physics*, 39 , 201–225.
- Jerolmack, D. J., and Mohrig, D. (2005). A unified model for subaqueous bed form dynamics. *Water Resources Research*, 41 (12), 1–10. doi:10.1029/2005WR004329
- Layton, W. J., Schieweck, F., and Yotov, I. (2002). Coupling fluid flow with porous media flow. *SIAM Journal on Numerical Analysis*, 40 (6), 2195–2218. doi: 10.1137/S0036142901392766
- Ochoa-Tapia, J. A., and Whitaker, S. (1995). Momentum transfer at the boundary between a porous medium and a homogeneous fluid I. Theoretical development. *International Journal of Heat and Mass Transfer*. 38 (14), 2635–2646. doi: 10.1016/0017-9310(94)00346-W
- Sawyer, A. H., Cardenas, M. B. and Buttle, J. (2011). Hyporheic exchange due to channel-spanning logs. *Water Resources Research*, 47 (8), 1–12. doi:10.1029/2011WR010484
- Southard, J. B., and Boguchwal, L. A. (1990). Bed configurations in steady unidirectional water flows. Part2. Synthesis of flume data. *Journal of sedimentary petrology*, 60 (5), 658–679.

- Trauth, N., Schmidt, C., Maier, U., Vieweg, M., and Fleckenstein, J. H. (2013). Coupled 3-D stream flow and hyporheic flow model under varying stream and ambient groundwater flow conditions in a pool-riffle system. *Water Resources Research*, 49, 5834-5850, Retrieved from http://www.shom.fr/fr_page/fr_act_geo/abstract2008/a0_Alexander.pdf, doi: 10.1002/wrcr.20442
- Vafai, K., and Kim, S. J. (1990). Fluid mechanics of the interface region between a porous medium and a fluid layer-an exact solution. *International Journal of Heat and Fluid Flow* , 11 (3), 254–256. doi:10.1016/0142-727X(90)90045-D
- Van Mierlo, M. C. L. M. and de Ruiter, J. C. C. (1988) Turbulence measurements above artificial dunes. Rep. TOW A55 Q789. pp. 42. Delft Hydraul., Delft, Netherlands.
- Zhou, T., Bao, J., Huang, M., Hou, Z., Arntzen, E., Song, X., et al. (2018). Riverbed Hydrologic Exchange Dynamics in a Large Regulated River Reach. *Water Resources Research*, 54 (4), 2715–2730. doi: 10.1002/2017WR020508

6. BOULDER-DRIVEN HYPORHEIC EXCHANGE

The hyporheos is a subsurface space near riverbeds inundated by stream and groundwater. These ecotones are important drivers of ecosystem functions and services, influencing water quality and biogeochemical cycles. Stream restoration projects often use large boulders to reshape waterways or provide fish habitat. We investigate how boulder configuration (spacing and embeddedness) affects the near-bed flow. When boulders are mostly embedded, they do not affect the surface flow hydrodynamics enough to have a strong impact on hyporheic processes, regardless of their spacing. As the stones protrude more, recirculation eddies appear downstream but are smaller and less coherent where boulders are closer together. The interfacial flux (hyporheic exchange) increases as embeddedness decreases and spacing increases. As boulders are more embedded, the subsurface water moves more laterally and hyporheic flowpaths (and the associated travel times) are shortened. We also observe nonlinear dynamics between spacing and embeddedness; when boulders are close enough, there is a quiescent zone around them and little hyporheic exchange regardless of embeddedness. Our results suggest that increasing spacing and decreasing embeddedness could result in improved hyporheic flux and longer residence times, suggesting that stream restoration projects could improve fish habitat and water quality synergistically.

6.1 Boulder array configuration and Hydraulic conditions

We generated an artificial fluvial channel with an array of four boulders placed upon the sediment bed in a staggered manner. Figure 6.1. shows the boulder array setting along with the surface and subsurface flow domains. The shape of fluvial boulder is modelled as an ellipsoid (Krumbein, 1941) with a typical ratio of axial diameters of fluvial boulders, $D_x : D_y : D_z = 10 \text{ cm} : 8 \text{ cm} : 6 \text{ cm}$, followed by (Graham and Midgley, 2000). The distance between the center of two adjacent boulders is d_x (x-axis) and d_y (y-axis), respectively. We define the parameter boulder spacing as $S = d_x/D_x = d_y/D_y$. The boulder spacing is related to the boulder concentration and it varies depending on the fluvial channel type. Another key parameter we are interested in is the boulder embeddedness. Davis et al. (2001) defined embeddedness as “qualitative estimate of the percent of substratum particles covered by fine materials.”. We adopted BSK-orig computational method to quantify embeddedness which is $100 \cdot D_e/D_z$ where D_z is the total height of boulder and D_e is the embedded height, respectively. We varied the spacing (S) and

embeddedness (E) of boulders: for the spacing, $S = 2, 3$, and 7 and for the embeddedness, $E = 5, 20, 35, 50, 65, 80$ and 95% . The average velocity is assumed to be steady, $\bar{U} = 0.1$ m/s. We set the water surface elevation to be constant throughout the surface domain, $h = 0.3$ m, and the groundwater depth is limited to $h_g = 1$ m.

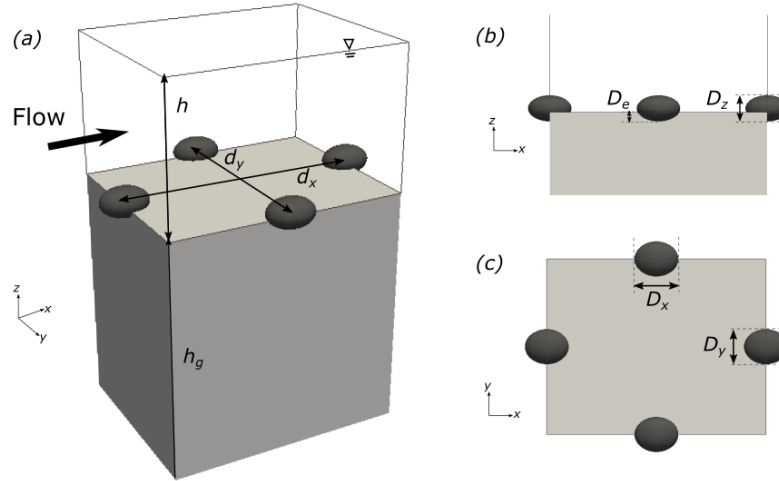


Figure 6.1 A conceptual diagram of a coupled surface-subsurface system with a boulder array with $S = 5$, $E = 35\%$. h (surface flow water depth) = 0.3 m, h_g (Groundwater depth) = 1 m.

(a) A geometry of a roughness element modelled by an ellipsoid having a ratio of axial diameters, $D_x : D_y : D_z = 10 \text{ cm} : 8 \text{ cm} : 6 \text{ cm}$. (b) An example of computational domain for As S increases, the distance between two adjacent boulders increases. As E increases, the boulder is more embedded into the sediment bed.

6.2 Experimental setup and boundary conditions

We used OpenFOAM 5.0 to solve a coupled surface-subsurface flow field and solute transport across the subsurface domain. Since we used four different settings for spacing and seven for embeddedness, $4 \times 7 = 28$ simulations were conducted in total. The smallest periodic domain found covers from the center of one boulder to the center of the next boulder in both streamwise (x -dir) and spanwise (y -dir) direction. The size of the domain is $S \cdot d_x$ (x -dir) and $S \cdot d_y$ (y -dir) where S is the boulder spacing. The average channel water depth and the depth of groundwater (z -dir) set to 0.3 m and 1 m while the flow velocity is set to 0.1 m/s. The highest Reynolds number and Froude number we can have under such condition is when the embedded is the smallest, which results in $Re = 17,142$ and $Fr = 0.046$, respectively. With such low Froude number, the effect of water depth on the bed pressure variation or hyporheic exchange

processes can be assumed to be negligible. In addition, we assumed no sediment transport under such hydraulic conditions.

No-slip boundary is used at the bottom of the surface/subsurface domain and at the boulder boundaries (e.g. boulder-water interface, boulder-sediment interface). The rough wall function is applied at the channel bed. We imposed a periodic boundary condition for inlet/outlet (streamwise direction) and east/west walls (spanwise direction) in both surface and subsurface domain. The pressure fields at the bottom of surface water flow are prescribed to the upper boundary of subsurface flow. The mesh is generated in such a way that $y^+ = 4$ near the bed and boulder.

Natural river flows are driven by the x -dir component of gravitational force, $\rho \mathbf{g}_x$. However, since the simulation domain in this work is periodic in the x -dir, special treatment is used to make the pressure field compatible with the periodicity requirement. Indeed, in all simulations, a desired mean flow velocity, $\bar{\mathbf{U}}$, (equivalently desired discharge) is enforced through an adjustable body force in the momentum equation. At every time step, the gravity term in the streamwise direction (adjustable body force) in the momentum equations of surface and subsurface flow, Eq. (3.15) and (3.26), is calculated as follows:

$$\rho \mathbf{g}_x = \omega \frac{(|\bar{\mathbf{U}}| - |U_{avg}|)}{a_p} \quad (6.1)$$

where ω is relaxation factor which is 0.2 in this research, $|U_{avg}|$ is the magnitude of volume averaged streamwise velocity, and a_p is the diagonal elements of the linear system equation for velocity. In this study, the mean flow velocity, $\bar{\mathbf{U}}$, is set to 0.1 m/s.

The boulder configuration such as spacing and embeddedness determines the turbulent flow regime (e.g. smooth, semi-smooth, or quasi-smooth). In particular, the embeddedness of boulder controls the surface roughness height, which often characterizes the channel flow field. Thus, we introduce the Reynolds number associated with the height of the boulder, Re_h , as

$$Re_h = \frac{U_{avg} H}{\nu} \quad (6.2)$$

where U_{avg} is the averaged velocity which is 0.1 m/s, H is the height of a boulder and ν is kinematic viscosity of water. Table 1. shows the corresponding Reynolds number to the embeddedness.

Table 6.1. Embeddedness and corresponding Reynolds number (Re_h). Re_h decreases as the boulder more embedded.

Embeddedness	5 %	20 %	35 %	50 %	65 %	80 %	95 %
Re_h	3,631	3,057	2,484	1,911	1,338	764	191

6.3 Result

6.3.1 Effect of boulder array configuration on the flow field

Figure 6.2. depicts three-dimensional streamlines colored based on the magnitude of the velocity with various spacing and embeddedness conditions. A typical cycle of flow passing by an emergent obstacle is characterized by a sequence of zones of (1) flow acceleration and detachment near the boulder's crest, (2) flow deceleration and recirculation behind the boulder, and (3) flow reattachment and recovering further downstream from the boulder (Buffin-Belanger and Roy, 1998). Depending on the spacing and embeddedness condition, however, some of phenomena within the sequence would become insignificant or vanish. For the cases with large embeddedness (small surface roughness), the recirculation zone would disappear as the flow is hardly detached at the boulder's crest regardless of the distance between boulders. Since the flow has not been separated, we do not expect the flow reattachment but the flow recovers its velocity profile shortly after passing by a boulder. For the cases with small embeddedness (large surface roughness), the recirculation vortex is observed in both closely-packed and loosely-packed cases, but the size of vortex was smaller and less coherent in the closely-packed case. This is because the flow passing by an array of small-spaced boulders is a quasi-smooth or skimming flow whose roughness element wake is strongly interfered by the next boulder, decelerating the streamwise flow velocity greatly. Due to this mechanism, the velocity profile is not fully recovered within the inter-boulder space, forming the enclosed pockets of dead fluid (Morris, 1959). The roughness element wake is rarely affected by the next element in the large-spacing case, which insinuates the flow is a semi-smooth turbulent or isolated-roughness flow.

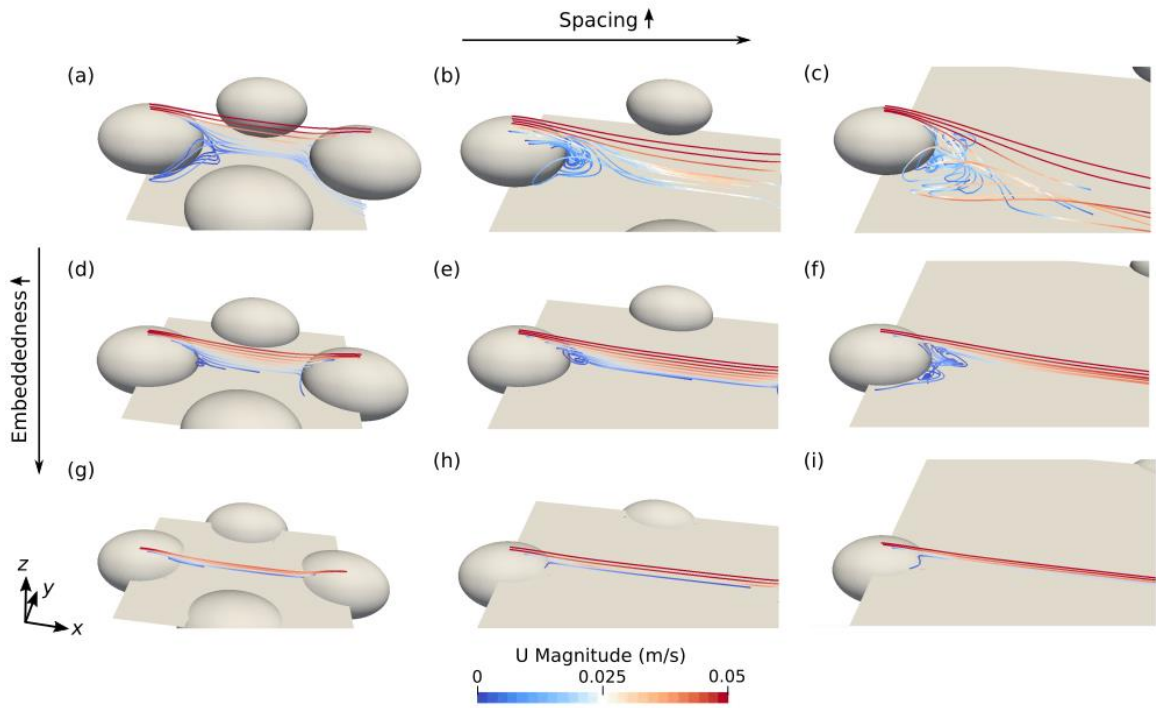


Figure 6.2 Channel flow fields depicted with three-dimensional streamlines colored with the magnitude of the velocity with various spacing (S) and embeddedness (E) conditions: (a) $S = 2$, $E = 5\%$ (b) $S = 3$, $E = 5\%$ (c) $S = 7$, $E = 5\%$ (d) $S = 2$, $E = 50\%$ (e) $S = 3$, $E = 50\%$ (f) $S = 7$, $E = 50\%$ (g) $S = 2$, $E = 80\%$ (h) $S = 3$, $E = 80\%$ (i) $S = 7$, $E = 80\%$. For the cases with large embeddedness, the recirculation zone would disappear as the flow is hardly detached at the boulder's crest regardless of the distance between boulders. For the cases with small embeddedness, the recirculation vortex is observed in both closely- and loosely-packed cases, but the size of vortex was smaller and less coherent in the closely-packed case.

Within the vicinity of boulders, the streamwise velocity either accelerates or decelerates depending on the relative location to the boulder element: the streamwise velocity is accelerated above the boulder's crest ($z/D_c > 1.0$) whereas it decreases below the boulder's crest ($z/D_c < 1.0$). Dey et al. (2011) suggested the difference in streamwise velocity between simulations with boulders and without boulders, Δu , is significant in the area below $z/D_c = 0.9$ where the effect of boulders is noticeable. In addition, below the boulder's crest, the streamwise velocity is strongly decelerated in both upstream and downstream of the boulder. The mechanism causing deceleration behind the boulder is different from that of upstream of the boulder: in the downstream of the obstacle, the streamwise velocity is reduced by the flow separation and recirculation while the obstacle physically blocks the water flow to pass through. it, transferring kinematic energy to static energy in front of the obstacle. The presence of

boulder even changes the flow path to move along the lateral side of the boulder rather than the vertical side when the boulder is less embedded as it provides shorter and smoother passage.

6.3.2 Pressure variation across the sediment bed and interfacial flux

The near-bed flow structures create the pressure variation at the channel bottom, thus controlling the interfacial flux. Figure 6.3. shows the pressure field across the bed with different boulder settings. For all cases, we observe the high-pressure area in front of the boulder and the low-pressure zone alongside the boulder. The presence of boulder accounts for such high pressure region, transferring the form of energy from kinetic to static. The flow deceleration results in raising up the pressure and this can be explained by the Bernoulli's principle: along the streamline, the pressure rises as the velocity decelerates. By the same principle, an acceleration in velocity results in lowering the pressure which can be seen alongside the boulder.

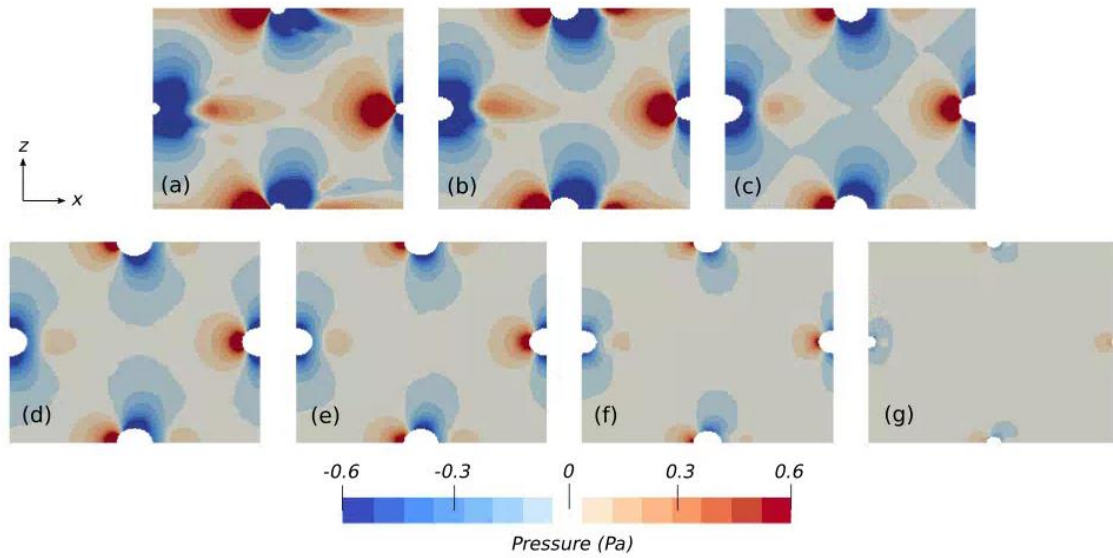


Figure 6.3 The pressure distribution over the sediment bed for various boulder embeddedness (E) with constant spacing (S), $S = 7$, (a) $E = 5\%$ (b) $E = 20\%$ (c) $E = 35\%$ (d) $E = 50\%$ (e) $E = 65\%$ (f) $E = 80\%$ (g) $E = 95\%$. The size of both high- and low-pressure zone is larger and spread out across the sediment bed when the boulder embeddedness is small. The small embeddedness also produces more complicated low-pressure variation since an additional factor, a funnel vortex, contributes to the flow acceleration near the bed.

Some distinctive features of pressure distribution are observed in the case with small boulder embeddedness, $E < 0.5D_z$. When $E > 0.5D_z$, it exhibits a typical pressure distribution around a cylinder, or a hemisphere: high-pressure region facing upstream and low-pressure

area around the perimeter of boulder boundary. In both small and large embeddedness cases, we observe that the maximum pressure occurs at the most front-side of the boulder, e.g. $x = -0.5D_x$. For the cases with small embeddedness, the low-velocity zone beneath the center of boulder ($x > -0.5D_x$, $z < 0.5D_y$) is generated so that the high-pressure area can be further extended to the boulder-sediment interface. In other words, high-pressure zones are larger and more spread out across the sediment bed when the boulder embeddedness is small. The small embeddedness also produces more complicated low-pressure variation since an additional factor, a funnel vortex, contributes to the flow acceleration near the bed. The size of low-pressure zone is also enlarged compared to the case with large embeddedness and this is due to the change in flow path, from vertical to lateral direction. If the embeddedness is large, the flow tends to pass over the boulder's crest (vertical movement) whereas the flow goes around the boulder (lateral movement) if the embeddedness is small, especially when $E < 0.5D_z$.

Figure 6.4. shows the effect of boulder array setting on the hyporheic exchange rate. The interfacial flux increases as the embeddedness decreases (Figure 6.4a) and as the spacing increases (Figure 6.4b) except for the case with the smallest spacing. Generally, as boulders are less embedded, pressure variations increase, generating larger gradients across the riverbed, thus driving more hyporheic flux. For the smallest spacing setting, the inverse relationship between the embeddedness and flux no longer holds. This implies there is nonlinear dynamics between the spacing and embeddedness contributing to the exchange rate between surface and subsurface domain. When boulders are densely packed, the flow trapped in the dead zone between boulders does not accelerate or decelerate as much as it does in the loosely-packed case. In other words, in the smallest spacing case, the effect of the dead zone becomes significant preventing the flow recovery as the boulder less embedded.

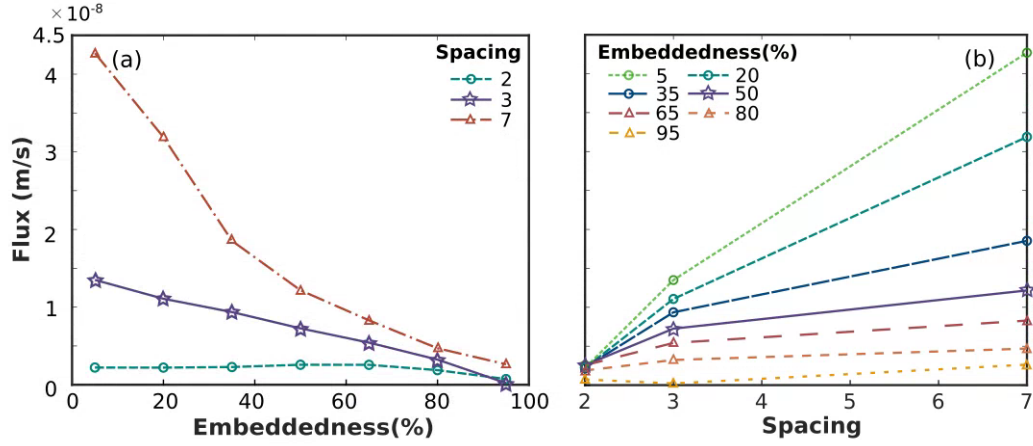


Figure 6.4 The dependence of hyporheic flux on (a) Embeddedness (E) and (b) Spacing (S). The interfacial flux increases as the embeddedness decreases and as the spacing increases except for the case with the smallest spacing. This implies there is nonlinear dynamics between the spacing and embeddedness contributing to the exchange rate between surface and subsurface domain.

6.3.3 Solute transport and residence time distribution

We simulated the mass transport through the subsurface domain to investigate how the boulder array configuration affect the residence time of solute inside the hyporheic zone. Figure 6.5. presents the normalized solute mass inside the bed (a) with different spacing (S) while the embeddedness is the smallest, $E = 5\%$ and (b) with different embeddedness (E) while the spacing is the smallest, $S = 2$. The figure shows the average residence time (RT) decreases from $S = 2$ to $S = 3$, but increases from $S = 3$ to $S = 7$. The residence time is directly proportional to the flow velocity and inversely proportional the length of flow path. A decrease in the average RT from $S = 2$ to $S = 3$ can be explained by an increase in the flux resulting in increase in velocity. The length of flow paths also increased, but it is compensated by a significant increase in flux. We observed a fast decrease of the mass in the bed for $S = 7$ before 1 day, but the rate of change becomes milder after then. The fast decrease is associated with the solute particles traveling through the region with small flow paths with fast flow velocities, so called “Region of local system of groundwater flow” in Toth’s flow. After then, the solute particles within the “region of intermediate or regional system” started leaving from the bed, resulting in a slow decrease in the total mass inside the bed. We see clearer pattern for the case with different embeddedness. The average residence time decreases as the embeddedness increases. Since the interfacial flux, which represents groundwater velocity, does not vary significantly

with respect to embeddedness (Figure 6.4b), the variation in residence time distribution is due to the difference in length of flow path.

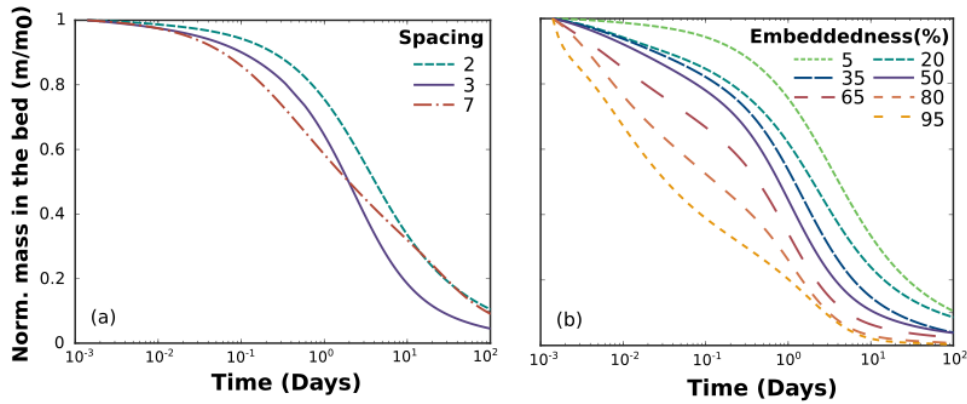


Figure 6.5 The normalized solute mass inside the bed (a) with different spacings (S) while the embeddedness is the smallest, $E = 1$ and (b) with different embeddednesses (E) while the spacing is the smallest, $S = 2$. The average residence time decreases as the embeddedness increases. As the boulder is embedded, the lateral movement of tracer becomes dominant making the path shorter, reducing the residence time of solute in the bed.

Figure 6.6. shows tracer paths of solute released at the centerline of the sediment bottom. In the case with the smallest embeddedness, most of paths move along the streamwise direction. As the boulder embeddedness increases, the path starts to move in lateral direction (Figure 6.6b, 6.6c) as the streamwise route is hindered by the submerged boulder. As the boulder is more embedded, the lateral movement of tracer becomes dominant making the path even shorter, reducing the residence time of solute in the bed. Thus, increases in embeddedness can negatively affect the hydro-ecosystem in reducing not only the space for aquatic organism but also the residence time of solute inside the bed.

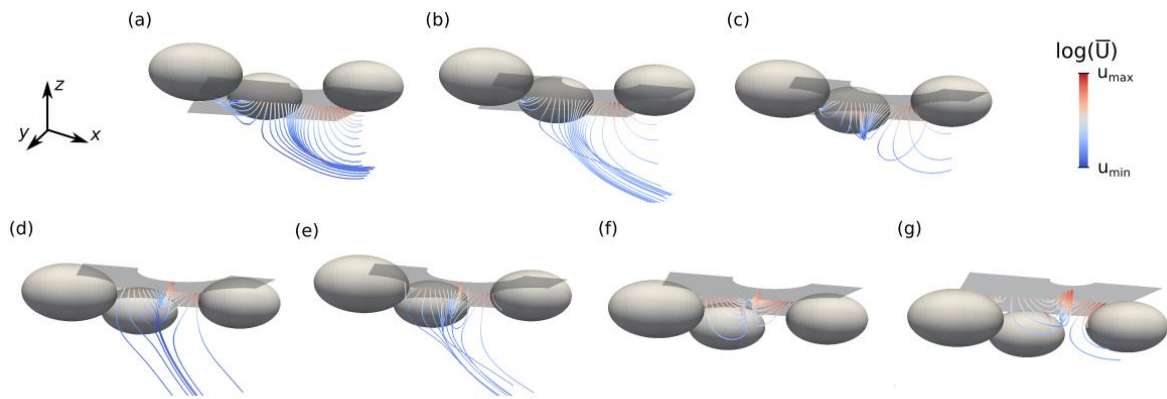


Figure 6.6 Tracer paths of solute released at the centerline of the sediment bottom: for various boulder embeddedness (E) settings with constant spacing ($S = 1$): (a) $E = 5\%$ (b) $E = 20\%$ (c) $E = 35\%$ (d) $E = 50\%$ (e) $E = 65\%$ (f) $E = 80\%$ (g) $E = 95\%$. As the boulder embeddedness increases (b, c), the path starts to move in lateral direction as the streamwise route is hindered by the submerged boulder. As the boulder is more embedded (e, f, g), the lateral movement of tracer becomes dominant making the path even shorter, reducing the residence time of solute in the bed.

6.4 Discussion

Roughness elements such as bedforms, vegetation, large woody debris and fluvial rocks provide flow resistance and diversify water depths and velocities across the channel. In stream restoration, boulders are often used to promote low-velocity pockets and eddies to provide fish passage and habitat (Gorman and Karr, 1978; Gregory et al., 1991; Gordon et al., 1992; Rabeni and Jacobson, 1993; Maddock, 1999; Allan and Castillo, 2007). Our study on the effect of boulder spacing and embeddedness on hyporheic exchange can further inform guidelines on designing engineered systems in terms of water/solute exchange and transport processes between the surface and subsurface region. For example, we showed that frequent boulder elements caused short hyporheic flow paths under each boulder whereas broader spacing resulted in longer hyporheic circulation. We also demonstrated that embeddedness has a significant impact on hyporheic exchange processes in terms of both interfacial flux and residence time.

Large woody debris (LWDs) are ubiquitous large roughness elements, often used in restoration projects to add channel complexity and provide ecological benefits (Valett et al., 2002; Curran and Wohl 2003; Gippel, 1995; Gurnell et al. 1995; Miller et al. 2010). Boulders and LWDs are similar in that they disturb the flow field, generate pressure gradients across the bed, and drive hyporheic exchange (Kasahara et al, 2009; Krause et al., 2014). Natural wood

however rarely lies directly on the channel bottom as limbs can hold it up. If water can flow through the woody debris, the velocity upstream can accelerate and scour through the gaps (Sawyer et al., 2011), whereas it decelerates upstream of the boulder and reaches a maximum on the sides. The wake generated by the LWD does not expand to the sediment bed surface since it reattaches with the flow going under the log, while the boulder wake can interact with the sediment bed.

We did not explore changing hydraulic conditions (e.g. water depth, flow velocity) or the shape and size of the boulders in order to isolate the effects of spacing and embeddedness. However, hydraulic conditions can greatly alter the surface flow field and associated hyporheic exchange processes since (1) water surface elevation will change due to the presence of boulder as Fr increases (Shamloo et al, 2001; Dermisis and Papanicolaou, 2014), (2) vortex/turbulent structures will be more complicated as Re increases (Dargahi, 1989; Sumer and Fredsoe, 2006) and (3) scour will developed around the solid object (Liu, 2008; Euler and Herget, 2012; Schlomer et al., 2020). In addition, the particle size distribution of the substrate is an important factor controlling the hydro-ecosystem (Schneck et al., 2011). Cooper (1965) showed that extremely uniform gravels, except in coarse gravels, reduce the survival rate of salmon eggs. In order to provide sufficient dissolved oxygen to the eggs and other organisms, it is essential to understand the linkage between the substrate size distribution and the hyporheic exchange processes. Our results suggest that adding boulders in a reach could enhance hyporheic fluxes and thus benefit sensitive species.

In this study, we assessed the effect of boulder spacing and embeddedness on hyporheic exchange from a physical standpoint: surface and subsurface flow fields, pressure distribution across the sediment/water interface and the residence time in the bed. As river restoration projects become more holistic, geomorphological, biogeochemical and hydro-ecological aspects should also be considered. For example, we show that embeddedness reduced hyporheic exchange, which could negatively affect oxygen sensitive fish or macroinvertebrate species. Embeddedness also reduces hyporheic flow paths and residence times, which in turn could also limit the amount of biogeochemical reactions that proceed. In this case, a potential benefit on water quality is lost.

6.5 Summary and conclusions

We investigated how boulder spacing and embeddedness affect the near-bed hydrodynamics and the surface-subsurface water exchange. Depending on the spacing and

embeddedness, the flow pattern passing over a boulder array changed significantly. For the cases with large embeddedness, the recirculation zone would disappear as the flow is hardly detached at the boulder's crest regardless of the distance between boulders. For the cases with small embeddedness, the recirculation vortex is observed in both closely-packed and loosely-packed cases, but the size of vortex was smaller and less coherent in the closely-packed case. For these dense clusters, the inverse relationship between embeddedness and flux no longer holds. There is thus nonlinear dynamics between the spacing and embeddedness contributing to the exchange rate between the surface and subsurface domain. As embeddedness increases, the subsurface flowpaths move in the lateral direction, as the streamwise route is hindered by the submerged boulder and the average residence time therefore decreases. As restoring streams and rivers has moved from aesthetics and forms to a more holistic approach that includes processes, we hope our study can inform designs that benefit both structural and functional outcomes. Hyporheic exchange is key to buffer water quality and temperatures in streams and rivers, while also providing localized downwelling and upwelling microhabitats. This study provides evidence that improving exchange while reaching other restoration goals is possible.

6.6 References

- Allan, J. D. and Castillo, M. M. (2007) *Stream Ecology: Structure and function of running waters*. Dordrecht, The Netherlands. Springer.
- Buffin-Belanger T. and Roy, A. G. (1998) Effects of a pebble cluster on the turbulent structure of a depth-limited flow in a gravel-bed river. *Geomorphology*, 25, 249–267
- Cooper, A.C. (1965) The effect of transported stream sediments on survival of sockeye and pink salmon eggs and alevin. *Int. Pac. Salmon Fish. Comm. Bull.* 18, 1–71.
- Curran, J. H. and Wohl, E. E. (2003) Large woody debris and flow resistance in step-pool channels, Cascade Range, Washington. *Geomorphology* 51(1):141–157
- Davis, J. C., Minshall, G. W., Robinson, C. T., and Landres, P. (2001) *Monitoring wilderness stream ecosystems*. General Technical Report RMRS-GTR-70. USDA Forest Service, Rocky Mountain Research Station, Ogden, UT
- Dargahi, B. (1989) The turbulent flow field around a circular cylinder. *Experiments in Fluids*. 8(1–2), 1–12.
- Dermisis, D. and Papanicolaou, A. N. (2014) The effects of protruding rock boulders in regulating sediment intrusion within the hyporheic zone of mountain streams. *Journal of Mountain Science* 11(6). doi: 10.1007/s11629-014-3054-9

- Dey, S., Sarkar, S., Bose, S. K., Tait, S., and Castro-Orgaz, O. (2011) Wall-wake flows downstream of a sphere placed on a plane rough-wall, *J. Hydraul. Eng. ASCE* 137, 10, 1173-1189, doi: 10.1061/(ASCE)HY.1943-7900.0000441.
- Euler, T. and Herget, J. (2012) Controls on local scour and deposition induced by obstacles in fluvial environments. *CATENA* 91, 35–46.
- Graham, D. J. and Midgley N. G. (2000) Graphical representation of particle shape using triangular diagrams: an Excel spreadsheet method. *Earth Surf. Proc. Landf.* 25: 1473–1477
- Gippel, C. J. (1995) Environmental hydraulics of large woody debris in streams and rivers. *J. Environ. Eng.* 121(5):388-395
- Gordon N. D., McMahon, T. A., Gippel, C. J. and Nathan, R. J. (2nd ed.) (1992) *Stream Hydrology: An introduction for Ecologists*, Chichester, West Sussex, England, John Wiley and Sons Ltd.
- Gorman and Karr (1978) Habitat Structure and Stream Fish Communities. *Ecology*, 59(3), 507-515
- Gregory, S. V., Swanson, F. J., McKee, W. A. and Cummins K. W. (1991) An Ecosystem Perspective of Riparian Zones. *BioScience*, 41(8), 540-551
- Gurnell, A. M., Gregory, K. J. and Petts, G. E. (1995) The role of coarse woody debris in forest aquatic habitats: implications for management. *Aquat Conserv Mar Freshw Ecosyst* 5(2): 143–166
- Kasahara, T., Datry, T., Mutz and M., Boulton, A. J. (2009) Treating causes not symptoms: restoration of surfacegroundwater interactions in rivers. *Mar. Freshw. Res.* 60(9):976-981
- Krause, S., Klaar, M., Hannah, D., Mant, J., Bridgeman, J., Trimmer, M. and Manning-Jones, S. (2014) The potential of largewood debris to alter biogeochemical processes and ecosystem services in lowland rivers. *Wiley Interdiscip. Rev. Water* 1(3):263-275
- Krumbein, W. C (1941) Measurement and geological significance of shape and roughness of sedimentary particles. *Journal of Sedimentary Petrology*, 11(2), 64-72
- Liu, X. (2008), *Numerical Models for Scour and Liquefaction Around Object Under Currents and Waves*, PhD Thesis, University of Illinois at Urbana-Champaign.
- Maddock, I. (1999) The importance of physical habitat assessment for evaluating river health. *Freshwater Biology*, 41, 383-391
- Miller, S. W., Budy, P. and Schmidt, J. C. (2010) Quantifying macroinvertebrate responses to in-stream habitat restoration: applications of meta-analysis to river restoration. *Restor Ecol* 18(1):8–19
- Morris, H. (1959) Design methods for flow in rough conduits. *Journal of the American Society of Civil Engineers*, 85(7), 43-62.

- Rabeni C. F. and Jacobson, R. B (1993) The importance of fluvial hydraulics to fish-habitat restoration in low-gradient alluvial streams. *Freshwater Biology*, 29, 211-220
- Sawyer, A. H., Cardenas, M. Bayani, and Buttles, J. (2011) Hyporheic exchange due to channel-spanning logs. *Water Resour. Res.*, 47, W08502, doi:10.1029/2011WR010484.
- Schlomer, O., Herget J. and Euler, T. (2020) Boundary condition control of fluvial obstacle mark formation – framework from a geoscientific perspective. *Earth Surf. Process. Landforms* 45, 189–206
- Schneck, F., Schwarzbald, A., and Melo, A. S (2011) Substrate roughness affects stream benthic algal diversity, assemblage composition, and nestedness. *Journal of the North American Benthological Society*, 30, 4, pp. 1049-1056
- Shamloo, H., N. Rajaratnam, and Katopodis, C. (2001) Hydraulics of simple habitat structures. *J. Hydraul. Res.* 39, 4, 351-366, doi: 10.1080/00221680 109499840.
- Sumer B. M. and Fredsoe, J. (2006) *Hydrodynamics around cylindrical structures (Revised Edition)*, World Scientific Publishing Co., Danvers, MA 01923, USA
- Valette, H. M., Crenshaw, C. L. and Wagner, P. F. (2002) Stream nutrient uptake, forest succession, and biogeochemical theory. *Ecology*, 83(10), 2002, pp. 2888–2901

7. PREDICTING CHANNEL BED PRESSURE USING POINT VELOCITY DATA WITH DATA-DRIVEN MODELS

Numerical modeling of fluid flows primarily depends on solving the partial differential equation systems in a discretized form, which is known as computational fluid dynamics (CFD). This approach typically involves solving partial differential equations, such as the Navier-Stokes equations of fluid flow. While conventional CFD methods give high-accuracy results, they are often computationally expensive. In many applications, CFD simulations are considered one of the most intensive and time-consuming processes. Thus, it is difficult to apply CFD models into real-time predictions and many-query analysis (e.g., optimization design of aircrafts with large parameter variations) and forward/inverse uncertainty quantification (UQ). In this study, we propose a general artificial neural network (ANN) based data-driven model for predicting the pressure field at the channel bottom using point velocities at different level. We show that ANN based surrogate models can estimate the pressure field compared to other linear regression model. Overall, ANN produces consistent and accurate prediction performance under various conditions whereas other linear surrogate models significantly depend on input variable

7.1 Methods

We generated an artificial fluvial channel with an array of four boulders placed upon the sediment bed in a staggered manner then simulated channel flow field using computational fluid dynamics. The numerical simulation has been completed in Chapter 6, so we collected velocity and pressure values for every 0.01 m interval in both x and y directions except the region where the boulder is placed, resulting in 3869 in total. We chose the one with largest spacing and smallest embeddedness as it shows various flow characteristics such as flow separation at the stagnation point, wakes behind the boulder, flow deceleration and acceleration.

We constructed three different data-driven models with multivariate linear regression (MLR), local multivariate linear regression (LMLR) and artificial neural network (ANN). The input variable is velocity in x, y, and z directions, U , and the target variable is pressure at the sediment bed. Multivariate Linear Regression (MLR)

7.1.1 Multivariate Linear Regression (MLR)

MLR, one of the fundamental supervised learning algorithm, is an important algorithm in the field of machine learning. If it is assumed that the variable y is affected by m independent variables, $\mathbf{x} = (x_1, \dots, x_d)^T$, then the linear model for regression is:

$$y(\mathbf{x}, \mathbf{w}) = w_0 + w_1 x_1 + \dots + w_d x_d + \epsilon \quad (7.1)$$

where ϵ is an error and w_0, \dots, w_d are coefficients of the linear model. Given an N independent and identically distributed (i.i.d.) data set $\{y^{(i)}, x_1^{(i)}, \dots, x_d^{(i)}\}$ for $i = 1, \dots, N$, regression coefficients are estimated by minimizing the objective function, the sum of the distances of observation points from the plane:

$$\begin{aligned} J_{MLR} &= \arg \min_{\mathbf{w}} \sum_{i=1}^N \left(y^{(i)} - w_0 - w_1 x_1^{(i)} - \dots - w_d x_d^{(i)} \right)^2 \\ &= \arg \min_{\mathbf{w}} \sum_{i=1}^N (\epsilon^{(i)})^2 = \arg \min_{\mathbf{w}} \|Y - XW\|^2 \end{aligned} \quad (7.2)$$

where $\|\cdot\|$ the indicates Euclidean norm,

$$Y = \begin{bmatrix} y^1 \\ \vdots \\ y^N \end{bmatrix}, X = \begin{bmatrix} 1 & x_1^1 & x_2^1 & \dots & x_d^1 \\ \vdots & \vdots & \vdots & \dots & \vdots \\ 1 & x_1^N & x_2^N & \dots & x_d^N \end{bmatrix}, \text{ and } W = \begin{bmatrix} w_0 \\ \vdots \\ w_d \end{bmatrix} \quad (7.3)$$

By setting the gradient of the objective function to zero, the estimate \hat{W} is calculated as follows:

$$\hat{W} = (X^T X)^{-1} X^T Y \quad (7.4)$$

It is well known that the solution of MLR is optimal estimate when the errors $\epsilon^1, \dots, \epsilon^N$ are Gaussians.

7.1.2 Local Multivariate Linear Regression (LMLR)

All of the data is used to fit a single model in MLR. Instead, local data sets can be used to combine multiple regression models to find the relationship between input and output variables. Given an N i.i.d. data set, regression coefficients of LMLR are estimated by minimizing the objective function given by

$$J_{LMLR} = \arg \min_{\mathbf{w}} \sum_{i=1}^M \|Y_i - X_i W_i\|^2 \quad (7.5)$$

where M is a number of local data sets,

$$Y_1 = \begin{bmatrix} y^1 \\ \vdots \\ y^{WS} \end{bmatrix}, Y_2 = \begin{bmatrix} y^{WS+1} \\ \vdots \\ y^{2 \times WS} \end{bmatrix}, \dots, Y_M = \begin{bmatrix} y^{M \times WS+1} \\ \vdots \\ y^N \end{bmatrix} \quad (7.6)$$

$$X_1 = \begin{bmatrix} 1 & x_1^1 & \dots & x_d^1 \\ \vdots & \vdots & \dots & \vdots \\ 1 & x_1^{WS} & \dots & x_d^{WS} \end{bmatrix}, X_2 = \begin{bmatrix} 1 & x_1^{WS+1} & \dots & x_d^{WS+1} \\ \vdots & \vdots & \dots & \vdots \\ 1 & x_1^{2 \times WS} & \dots & x_d^{2 \times WS} \end{bmatrix}, \dots, \quad (7.7)$$

$$X_m = \begin{bmatrix} 1 & x_1^{M \times WS+1} & \dots & x_d^{M \times WS+1} \\ \vdots & \vdots & \dots & \vdots \\ 1 & x_1^N & \dots & x_d^N \end{bmatrix}$$

$$W_1 = \begin{bmatrix} w_0^1 \\ \vdots \\ w_d^1 \end{bmatrix}, W_2 = \begin{bmatrix} w_0^2 \\ \vdots \\ w_d^2 \end{bmatrix}, \dots, W_M = \begin{bmatrix} w_0^M \\ \vdots \\ w_d^M \end{bmatrix} \quad (7.8)$$

and WS is the preassigned size of the local data. Reducing in WS gives more accurate prediction result, however, it may cause overfitting problems since it becomes linear interpolation scheme as WS gets closer to 1. Then, the estimates $\widehat{W}_1, \dots, \widehat{W}_M$ are computed as follows:

$$\begin{aligned} \widehat{W}_1 &= (X_1^T X_1)^{-1} X_1^T Y_1 \\ &\vdots \\ \widehat{W}_M &= (X_M^T X_M)^{-1} X_M^T Y_M \end{aligned} \quad (7.9)$$

LMLR is appropriate to model complex processes for nonlinear systems based on the simple MLR method.

7.1.3 Artificial Neural Networks (ANNs)

The multi-perceptron is one of artificial neural network models that imitates the nonlinear relationship between input and output variables. The model aims to obtain the optimized weights of the network using a training algorithm designed to minimize the error between the output and target variables by modifying the mutually connected weights. In this study, the multi-perceptron with one hidden layer composed of 10 neurons is used.

The initial weights in the hidden layer are set to have random values between -1 and 1, and the initial biases are all set to zero. The next step is to multiply the weight matrix by the input data, \mathbf{x} , and add the bias so that

$$n_k^h = \sum_{j=1}^J w_{kj}^h x_j + b_k^h, \quad k = 1 \text{ to } K \quad (7.10)$$

where J and K are the number of input variables and hidden neurons, respectively, and \mathbf{x} , \mathbf{b}^h and \mathbf{w}^h are the input variable, bias, and weight in the hidden layer, respectively. The subscripts of the weight w_{kj}^h are written in such a manner that the first subscript denotes the neuron in question and the second one indicates the input variable to which the weight refers.

The n_k^h calculated by Equation (5) is fed into an activation function, f^h , to calculate a_k^h . Hyperbolic tangent sigmoid function is used as the activation function so that

$$a_k^h = \frac{e^{n_k^h} - e^{-n_k^h}}{e^{n_k^h} + e^{-n_k^h}} \quad (7.11)$$

In the output layer, the same procedure as that in the hidden layer is used except that only one neuron is used so that

$$n_1^o = \sum_{j=1}^K w_{1j}^o a_j^h + b_1^o \quad (7.12)$$

and the linear activation function is used to calculate a_1^o so that

$$U = n_1^o \quad (7.13)$$

The weights and biases are modified by the training to minimize the difference between the model output and target (observed) values. To train the network, the error function is defined as

$$\epsilon = ||Y - U||^2 \quad (7.14)$$

where Y is the target value vector to be sought. To minimize the error function, the Levenberg-Marquardt algorithm is used, which is the standard algorithm of nonlinear least-squares problems. We stop the training when the epoch reaches 1000.

7.2 Result and discussion

We constructed three different data-driven models with multivariate linear regression, local linear regression and ANN. The input variable is velocity in x, y, and z directions and the target variable is pressure at the sediment bed. From the CFD simulation, we collected velocity and pressure values for every 0.01 m interval in both x and y directions except the region where the boulder is placed, resulting in 3869 in total. The velocity extracted at different level, $z = 0.05, 0.15, 0.3$ m, are used in order to compare how much the velocity at each level contribute to the pressure at the bed. We test our models with different training/test ratio, 0.7/0.3 and 0.5/0.5, to see whether the suggested data-driven model is reliable when the training data is insufficient. Training data are randomly sampled from the entire dataset and the rest of data are used as test data. All the data used in developing data-driven models is normalized within a range of $[-1, 1]$ to consider the relative variance of variables.

The correlation coefficient (r) and root mean squared error (RMSE) between model output values (T) and target values (Y) of the test data are used to evaluate the performance of the models. The correlation coefficient and RMSE are defined as

$$r = \frac{\sum_i^N \frac{(Y_i - \bar{Y})(U_i - \bar{U})}{N-1}}{\sqrt{\sum_i^N \frac{(Y_i - \bar{Y})^2}{N-1}} \sqrt{\sum_i^N \frac{(U_i - \bar{U})^2}{N-1}}} \quad (7.15)$$

$$RMSE = \sqrt{\sum_i^N \frac{(Y_i - U_i)^2}{N}} \quad (7.16)$$

As r value becomes closer to 1, the correlation between model prediction and true value is strong. As RMSE goes to 0, the discrepancy between the model output and target is small.

Table 1 shows the performance of suggested surrogate models, MLR, LMLR, and ANN for the test dataset. Overall, ANN outperforms MLR and LMLR resulting in the highest r and lowest RMSE values. In terms of degrees of freedom (DOF), the traditional linear regression model, MLR, has only four DOF, $(\beta_0, \beta_1, \beta_2, \beta_3)$, while LMLR and ANN have 28 and 51, respectively. Furthermore, ANN is capable of capturing the underlying structure of the nonlinear data whereas MLR and LMLR are linear models. The prediction of MLR in Case 1 is not successful compared to that of Case 2 because underfitting occurs when the nonlinear data are included in the training dataset in Case 1. From the sensitivity analysis, we also find out velocities near the bed directly influences the pressure at the bed more than velocities at higher elevation do. This result accords with physical aspects of fluid flow for the flow field is spatially correlated so that the closer the distance between two locations, the more they interact.

Table 7.1. Performance of multivariate linear regression (MLR), local multivariate linear regression (LMLR), and artificial neural network (ANN) for test data. The cases where the MLR and LMLR show the best performance are colored in light orange. ANN produces consistent and accurate prediction performance under various conditions (light blue).

	Input	Case 1: 0.7/0.3		Case 2: 0.5/0.5	
		r	RMSE	r	RMSE
MLR	U(z=0.05 m)	0.235	0.156	0.295	0.163
	U(z=0.15 m)	0.123	0.159	0.149	0.169
	U(z=0.3 m)	0.019	0.160	0.059	0.171
LMLR	U(z=0.05 m)	0.619	0.126	0.512	0.155
	U(z=0.15 m)	0.634	0.124	0.504	0.148
	U(z=0.3 m)	0.713	0.112	0.589	0.138
ANN	U(z=0.05 m)	0.779	0.100	0.777	0.108
	U(z=0.15 m)	0.757	0.105	0.781	0.107
	U(z=0.3 m)	0.777	0.102	0.802	0.102

Overall, ANN produces consistent and accurate prediction performance under various conditions whereas MLR and LMLR significantly depends on input variable. Interestingly, the performance of LMLR rises to the peak point when it uses the farthest velocities as an input

and the training/test data ratio is 0.7/0.3. One thing to notice is that MLR and ANN incorporate with the data across the whole domain whereas LMLR uses subsets of the entire data when developed. Compared with MLR, the near-bed velocity explains bed pressure when it comes to the global or universal relationship whereas the velocity apart from the bed accounts for the pressure across the bed within the subdomain. In other words, the nonlinear structure is dominant in global scale whereas a linear trend explains the relationship between input and output in regional scale.

Figure 7.1. shows the pressure obtained from CFD simulation and the difference between the model output and target data for Case 1 (training/test = 0.7/0.3). The pressure and error is normalized within the range, $[-1, 1]$ and the boulder is depicted as a black ellipse. In Figure 2(a), the pressure around the boulder shows the similar pattern observed in the flow around a cylinder: the flow is stagnated in front of the boulder resulting in high-pressure region and the flow accelerates as it passes the obstacle causing a decrease in pressure. In Figure 2(b1) ~ 2(d3), the highest error is observed near the boulder, especially right in front of the obstacle, where the pressure is rapidly changing due to the unexpected disturbance created by boulder. While LMLR and ANN are able to model the general shape of pressure distribution, MLR barely captures the variation of pressure as shown in Figure 2(b1) ~ 2(b3) where the error plot shows almost the same pattern as the actual pressure. Still, LMLR is not able to predict the extreme change in pressure near the boulder unlike ANN. This is because of underfitting meaning that LMLR cannot represent the data having nonlinear structures.

Comparing ANN with LMLR, ANN predicted the pressure field across the bed more accurately than LMLR based on the point velocity data. Both ANN and LMLR are able to model the general trend of pressure variation, but only ANN captures the nonlinear relationship between the velocity and pressure near the boulder. Furthermore, the performance of LMLR depends on the training/test data ratio and the elevation where the velocity is extracted from whereas ANN gives more stable prediction result under various conditions. Lastly, since LMLR is a piecewise regression function, the regression formula is only applicable for the region where it is developed whereas ANN provides general function for the entire domain.

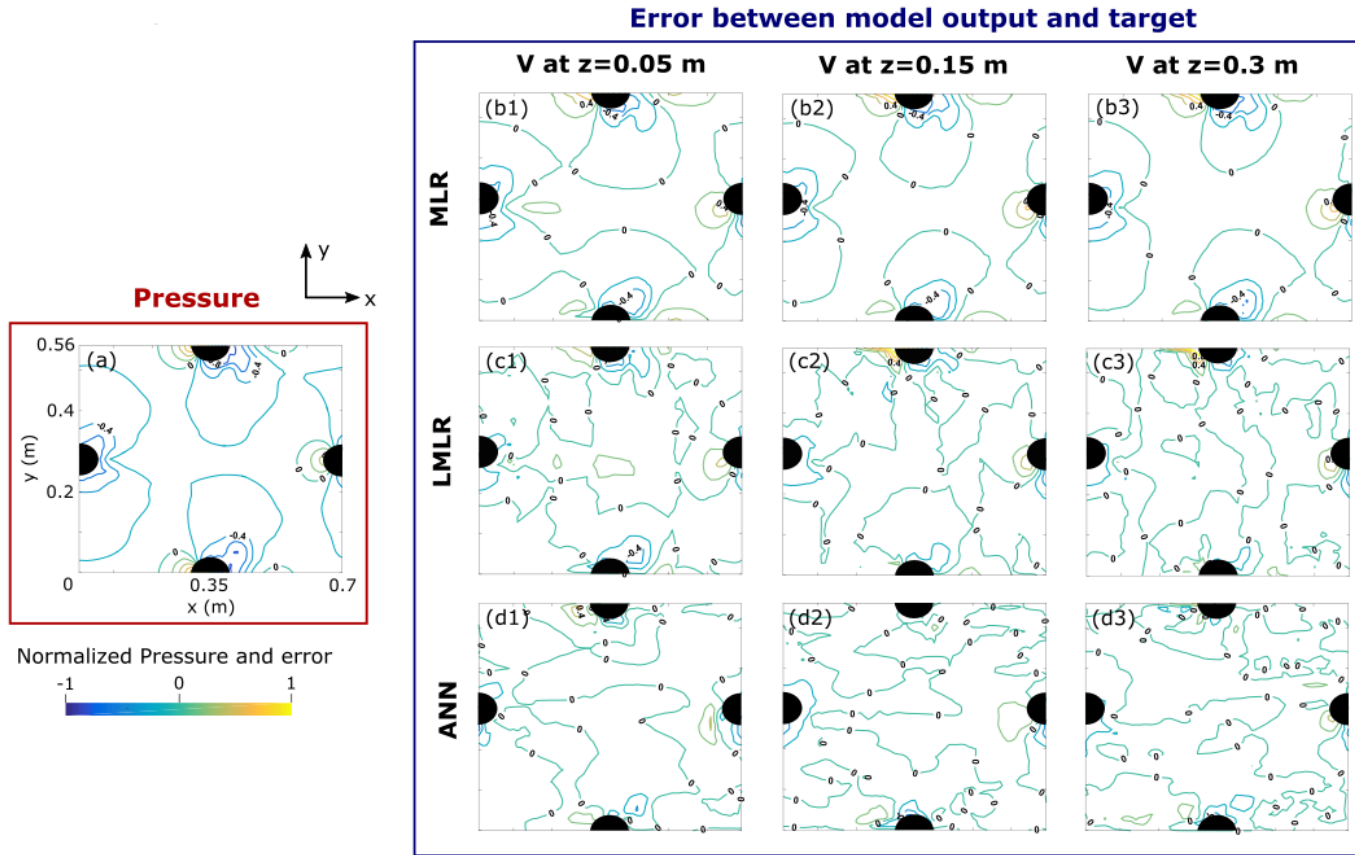


Figure 7.1. (a) The normalized pressure obtained from CFD simulation (b1) ~ (d3) The normalized difference between the model output and target data for Case 1 which uses 70% of data for training and 30% of data for test. The boulder is depicted as a black ellipse. The highest error is observed upstream and near the boulder. While LMLR and ANN are able to model the general shape of pressure distribution, MLR barely captures the variation of pressure where the error plot shows almost the same pattern as the actual pressure. Still, LMLR is not able to predict the extreme change in pressure near the boulder unlike ANN. This is because of underfitting meaning that LMLR cannot represent the data having nonlinear structures.

In this study, we developed and tested our surrogate models based on one single numerical simulation. This approach can be used when recovering missing data or when estimating pressure values using available velocity measurement data. Future research may incorporate with implementing the developed models to other numerical simulations under different conditions (e.g. mean flow velocity, boulder spacing, and boulder embeddedness) to test their performance. If the surrogate model can predict the relationship between pressure and velocity accurately under various conditions, then designers can utilize ANN to quickly iterate over multiple design alternatives to make decisions instead of conducting high-fidelity simulations during the early design stages.

7.3 Summary and conclusions

In this study, we propose a general artificial neural network (ANN) based data-driven model for predicting the pressure field at the channel bottom using point velocities at different level. We constructed three different data-driven models with multivariate linear regression, local linear regression and ANN. The input variable is velocity in x, y, and z directions and the target variable is pressure at the sediment bed.

We show that ANN based surrogate models can estimate the pressure field compared to other linear regression model. Comparing ANN with LMLR, ANN predicted the pressure field across the bed more accurately than LMLR based on the point velocity data. Both ANN and LMLR are able to model the general trend of pressure variation, but only ANN captures the nonlinear relationship between the velocity and pressure near the boulder. Overall, ANN produces consistent and accurate prediction performance under various conditions whereas other linear surrogate models significantly depend on input variable

8. SUMMARY AND CONCLUSIONS

This research investigated the dynamics of bio-fluvial-geomorphic influences on hyporheic exchange processes in various fluvial systems. We look at the “transitional” state in terms of geomorphology and hydrodynamic conditions. This thesis is composed of four different topics which are under the transitional states in terms of either geomorphology or hydrodynamics. In chapter 4, we investigate the effect of surface roughness (the scaling of bedform topography) on hyporheic exchange. In chapter 5, we study how the Froude number affects the exchange of water between surface and subsurface when the water surface is fixed and when it is allowed to adjust. In chapter 6, we discuss how boulder spacing and embeddedness affect the near-bed hydrodynamics and hyporheic exchange. Finally, in chapter 7, a surrogate model relating point velocities to pressure at the sediment bed is developed using neural networks. We assess the hyporheic exchange process in terms of interfacial flux and residence time distribution of solute in the hyporheic zone.

In chapter 4, we conducted a series of numerical simulations to systematically explore how the fractal properties of bedforms are related to hyporheic exchange. We compared the average interfacial flux (q_{int}) and residence time distribution in the hyporheic zone with respect to the magnitude of the power spectrum (C_q) and the fractal dimension (D) of riverbeds. First, we created two sets of fractal riverbed topologies: one with different maximum power spectrum density C_q and the other with different fractal dimension D . We then numerically simulated the turbulent flow field over the synthetic riverbeds and used the resultant head distribution as a boundary condition in simulations of hyporheic zone (groundwater) flow fields. Finally, random walk particle tracking simulations were used to quantify residence time distributions in the hyporheic zone. The results show that the average interfacial flux increases logarithmically with respect to C_q whereas it increases exponentially with respect to D . In addition, q_{int} generally increased with mean-square roughness (δ^2), yet the increases in flux remained more sensitive to increases in D than C_q . The additional roughness at larger D is more important than C_q at increasing q_{int} . These findings confirm that small features tend to dominate hyporheic exchange and imply that roughness is a significant driver of hyporheic exchange.

In chapter 5, we demonstrated how the Froude number affects the free-surface profile, total head over sediment bed and hyporheic flux. For larger Froude numbers (e.g. average Froude

number ($Fr_{avg} > 0.5$), a boil on the water after the peak is observed. The water profile undulates more as Fr_{avg} increases. The difference between the fixed-surface and free-surface case becomes significant as Froude number increases. For larger Fr_{avg} , the head at the peak of the dune for free-surface case is smaller than that of fixed-surface case inducing larger head gradient. This is mainly because they have different velocity profile at the dune peak: in the fixed-surface case, the vertical velocity profile from the bottom to the air-water interface follows the law of the wall so that the velocity at the air-water interface has the maximum value. On the contrary, in the free-surface case, the velocity at the interface no longer has the maximum value: the location having the maximum velocity moves closer to the sediment bed. This results in increasing velocity near the bed and larger head gradients, accordingly. Our future work is to study the mechanism of three-dimensional channel flow over complex geometry to analyze how the flow interacts with morphology.

In chapter 6, we investigated how boulder spacing and embeddedness affect the near-bed hydrodynamics and the surface-subsurface water exchange. Depending on the spacing and embeddedness, the flow pattern passing over a boulder array changed significantly. For the cases with large embeddedness, the recirculation zone would disappear as the flow is hardly detached at the boulder's crest regardless of the distance between boulders. For the cases with small embeddedness, the recirculation vortex is observed in both closely-packed and loosely-packed cases, but the size of vortex was smaller and less coherent in the closely-packed case. For these dense clusters, the inverse relationship between embeddedness and flux no longer holds. There is thus nonlinear dynamics between the spacing and embeddedness contributing to the exchange rate between the surface and subsurface domain. As embeddedness increases, the subsurface flowpaths move in the lateral direction, as the streamwise route is hindered by the submerged boulder. The average residence time therefore decreases as the embeddedness increases.

Lastly, in chapter 7, we propose a general artificial neural network (ANN) based data-driven model for predicting the pressure field at the channel bottom using point velocities at different level. We constructed three different data-driven models with multivariate linear regression, local linear regression and ANN. The input variable is velocity in x, y, and z directions and the target variable is pressure at the sediment bed. We show that ANN based surrogate models can estimate the pressure field compared to other linear regression model. Comparing ANN with LMLR, ANN predicted the pressure field across the bed more accurately than LMLR based on the point velocity data. Both ANN and LMLR are able to model the general trend of pressure variation, but only

ANN captures the nonlinear relationship between the velocity and pressure near the boulder. ANN produces consistent and accurate prediction performance under various conditions whereas other linear surrogate models significantly depend on input variable. Future research may incorporate with implementing the developed models to other numerical simulations under different conditions (e.g. mean flow velocity, boulder spacing, and boulder embeddedness) to test their performance. If the surrogate model can predict the relationship between pressure and velocity accurately under various conditions, then designers can utilize ANN to quickly iterate over multiple design alternatives to make decisions instead of conducting high-fidelity simulations during the early design stages.

Overall, we assessed the effect of geomorphological parameters on hyporheic exchange from a physical standpoint: surface and subsurface flow fields, pressure distribution across the sediment/water interface and the residence time in the bed. As restoring streams and rivers has moved from aesthetics and forms to a more holistic approach that includes processes, we hope our study can inform designs that benefit both structural and functional outcomes. Hyporheic exchange is key to buffer water quality and temperatures in streams and rivers, while also providing localized downwelling and upwelling microhabitats. This study provides evidence that improving exchange while reaching other restoration goals is possible. Our results could inform a number of critical processes, such as biological filtering for example. It is possible to use our approach to predict hyporheic exchange and thus constrain the associated biogeochemical processing under different topographies. As such, our results could be used to design more efficient biological filters. In a similar vein, as river restoration projects become more holistic, geomorphological, biogeochemical and hydro-ecological aspects should also be considered. For example, we show that embeddedness reduced hyporheic exchange, which could negatively affect oxygen sensitive fish or macroinvertebrate species. Embeddedness also reduces hyporheic flow paths and residence times, which in turn could also limit the amount of biogeochemical reactions that proceed. In this case, a potential benefit on water quality is lost.

PUBLICATION

Lee, A., Aubeneau, A. F., & Cardenas, M. B. (2020). The sensitivity of hyporheic exchange to fractal properties of riverbeds. *Water Resources Research*, 56, e2019WR026560.
<https://doi.org/10.1029/2019WR026560>